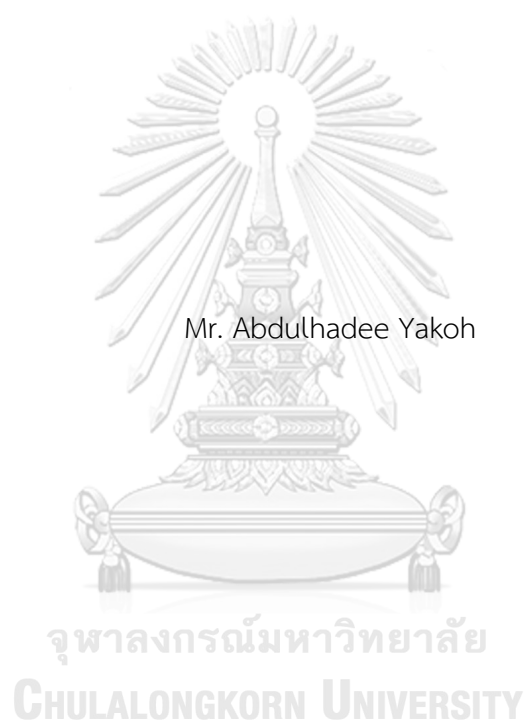DEVELOPMENT OF OPTICAL SENSOR FOR DETECTION OF CHLORIDE IONS AND
ELECTROCHEMICAL SENSOR FOR DETECTION OF CLINICAL INDICATORS

Mr. Abdulhadee Yakoh

จุฬาลงกรณ์มหาวิทยาลัย
CHULALONGKORN UNIVERSITY

A  Dissertation Submitted in Partial Fulfillment of the Requirements

for the Degree of Doctor of Philosophy in Chemistry

Department of Chemistry

FACULTY OF SCIENCE

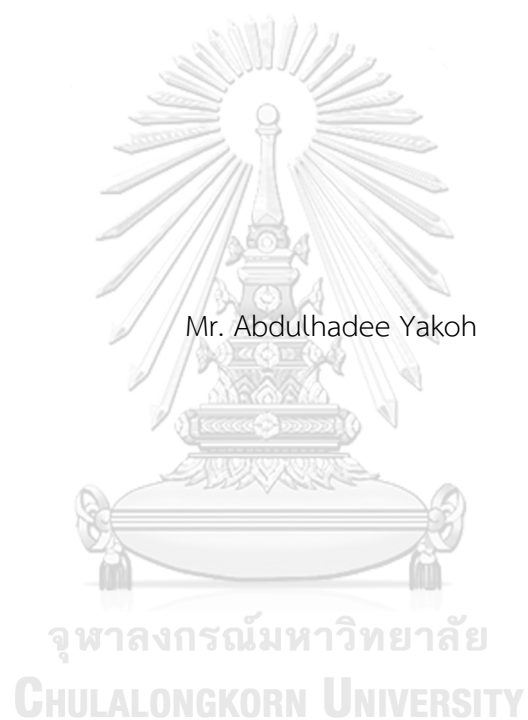Chulalongkorn University

Academic Year 2018

การพัฒนาเซ็นเซอร์เชิงแสงสำหรับการตรวจวัดไอออนคลอไรด์และเซ็นเซอร์เชิงเคมีไฟฟ้าสำหรับการตรวจวัดตัวบ่งชี้ทางการแพทย์

นายอับดุลฮาดี ยะโก๊ะ

วิทยานิพนธ์นี้เป็นส่วนหนึ่งของการศึกษาตามหลักสูตรปริญญาวิทยาศาสตรดุษฎีบัณฑิต
สาขาวิชาเคมี ภาควิชาเคมี
คณะวิทยาศาสตร์ จุฬาลงกรณ์มหาวิทยาลัย
ปีการศึกษา 2561

DEVELOPMENT OF OPTICAL SENSOR FOR DETECTION OF CHLORIDE IONS AND
ELECTROCHEMICAL SENSOR FOR DETECTION OF CLINICAL INDICATORS

Mr. Abdulhadee Yakoh

จุฬาลงกรณ์มหาวิทยาลัย
CHULALONGKORN UNIVERSITY

A Dissertation Submitted in Partial Fulfillment of the Requirements
for the Degree of Doctor of Philosophy in Chemistry
Department of Chemistry
FACULTY OF SCIENCE
Chulalongkorn University
Academic Year 2018

| | |
|---|---|
| Dissertation Title | DEVELOPMENT OF OPTICAL SENSOR FOR DETECTION OF CHLORIDE IONS AND ELECTROCHEMICAL SENSOR FOR DETECTION OF CLINICAL INDICATORS |
| By | Mr. Abdulhadee Yakoh |
| Field of Study | Chemistry |
| Thesis Advisor | Professor Dr. Orawon Chailapakul |
| Co Advisor | Associate Professor Dr. Weena Siangproh |

Accepted by the FACULTY OF SCIENCE, Chulalongkorn University in Partial Fulfillment of the Requirement for the Doctor of Philosophy

-------------------------------------------------- Dean of the FACULTY OF SCIENCE

(Professor Dr. Polkit Sangvanich)

DISSERTATION COMMITTEE

-------------------------------------------------- Chairman

(Associate Professor Dr. Vudhichai Parasuk)

-------------------------------------------------- Advisor

(Professor Dr. Orawon Chailapakul)

-------------------------------------------------- Co-Advisor

(Associate Professor Dr. Weena Siangproh)

-------------------------------------------------- Examiner

(Associate Professor Dr. Nattaya Ngamrojanavanich)

-------------------------------------------------- Examiner

(Associate Professor Dr. Suchada Chuanuwatanakul)

-------------------------------------------------- External Examiner

(Assistant Professor Dr. Amara Apilux)

อับดุลฮาดี ยะโก๊ะ : การพัฒนาเซ็นเซอร์เชิงแสงสำหรับการตรวจวัดไอออนคลอไรด์และเซ็นเซอร์เชิงเคมีไฟฟ้าสำหรับการตรวจวัดตัวบ่งชี้ทางการแพทย์. (DEVELOPMENT OF OPTICAL SENSOR FOR DETECTION OF CHLORIDE IONS AND ELECTROCHEMICAL SENSOR FOR DETECTION OF CLINICAL INDICATORS) อ.ที่ปรึกษาวิทยานิพนธ์หลัก : ศ. ดร.อรวรรณ ชัยลภากุล, อ.ที่ปรึกษาวิทยานิพนธ์ร่วม : รศ. ดร.วีณา เสียงเพราะ

วิทยานิพนธ์ฉบับนี้มุ่งเน้นการพัฒนาระบบการตรวจวิเคราะห์ขนาดย่อส่วนร่วมกับการใช้วัสดุระดับนาโนเมตรสำหรับการตรวจวัดสารบ่งชี้ที่สำคัญบางชนิดในสิ่งแวดล้อม เภสัชกรรม และการแพทย์ โดยสามารถแบ่งออกได้เป็น 2 ส่วนหลัก ประกอบด้วย (1) การพัฒนาระบบการตรวจวิเคราะห์ขนาดย่อส่วนร่วมกับการใช้วัสดุระดับนาโนเมตรสำหรับการตรวจวัดเชิงแสง และ (2) การพัฒนาระบบการตรวจวิเคราะห์ขนาดย่อส่วนร่วมกับการใช้วัสดุระดับนาโนเมตรสำหรับการตรวจวัดเชิงเคมีไฟฟ้า โดยวิทยานิพนธ์ส่วนแรกสามารถจำแนกออกเป็น 2 งานวิจัยย่อย โดยงานวิจัยย่อยที่ 1 มุ่งเน้นพัฒนาอุปกรณ์ตรวจวัดเชิงสีฐานกระดาษสำหรับการตรวจวัดไอออนคลอไรด์โดยใช้อนุภาคเงินปริซึมระดับนาโนเมตรร่วมกับการใช้สมาร์ทโฟนสำหรับการติดตามการเปลี่ยนแปลงสีของการเกิดปฏิกิริยาการกัดกร่อนแบบออกซิเดชันของอนุภาคเงินปริซึมระดับนาโนเมตรเป็นอนุภาคเงินทรงกลมระดับนาโนเมตรภายใต้การเหนี่ยวนำของไอออนคลอไรด์ ในงานวิจัยย่อยที่ 2 เป็นการพัฒนาเซนเซอร์จากจอภาพอิเล็กโทรลูมิเนสเซนซ์แบบพิมพ์สกรีนร่วมการกับใช้วัสดุกราฟีนออกไซด์ระดับนาโนเมตรขึ้นเป็นครั้งแรก โดยอุปกรณ์ที่พัฒนาขึ้นนี้สามารถนำไปใช้งานได้อย่างหลากหลาย เช่น จอภาพเรืองแสง เซนเซอร์สำหรับการตรวจวัดความเข้มข้นไอออน เซนเซอร์สำหรับการตรวจวัดความชื้น และเซนเซอร์สำหรับการติดตามลมหายใจของมนุษย์ งานวิจัยส่วนที่สอง อุปกรณ์ตรวจวัดเชิงเคมีไฟฟ้าได้ถูกพัฒนาขึ้น ซึ่งประกอบไปด้วย 2 งานวิจัยย่อย โดยงานวิจัยย่อยที่ 1 มุ่งเน้นพัฒนาขั้วไฟฟ้าจากวัสดุกราฟีนคอมโพสิตระดับนาโนเมตรที่สามารถลดการเกาะติดของวิตามินดีที่ผิวหน้าขั้ว จากผลการวิจัยพบว่าขั้วไฟฟ้าที่พัฒนาขึ้นมีประสิทธิภาพการตรวจวิเคราะห์ที่ดีและสามารถลดการเกาะติดของสารที่ผิวหน้าขั้วได้ งานวิจัยย่อยที่ 2 มุ่งเน้นพัฒนาอุปกรณ์วิเคราะห์ของไหลจุลภาคบนวัสดุฐานกระดาษสำหรับการนำส่งสารแบบซีเควนเชียล ร่วมกับการใช้วัสดุกราฟีนและอนุภาคทองระดับนาโนเมตร โดยระบบที่พัฒนาขึ้นนี้ถูกนำไปทดสอบกับการวัดแอสคอร์บิค เซโรโทนิน และอัลฟาฟีโตโปรตีน จากการวิจัยพบว่าระบบการตรวจวิเคราะห์ขนาดย่อส่วนทั้ง 4 แบบที่พัฒนาขึ้นให้ค่าความไวในการตรวจวิเคราะห์ที่ดี มีความจำเพาะเจาะจงสูง มีขนาดเล็กพกพาได้ และมีแนวโน้มที่จะนำไปใช้ในการตรวจวิเคราะห์นอกสถานที่ได้

| ภาควิชา | ภาควิชาเคมี | ลายมือชื่อนิสิต ................................................. |
|---|---|---|
| สาขาวิชา | เคมี | ลายมือชื่อ อ.ที่ปรึกษาวิทยานิพนธ์หลัก ................ |
| ปีการศึกษา | 2561 | ลายมือชื่อ อ.ที่ปรึกษาวิทยานิพนธ์ร่วม ................ |

# # 5672855023 : DOCTOR OF PHILOSOPHY

Optical sensor, Electrochemical sensor, Nanomaterial, Miniaturized device

Abdulhadee Yakoh : DEVELOPMENT OF OPTICAL SENSOR FOR DETECTION OF CHLORIDE IONS AND ELECTROCHEMICAL SENSOR FOR DETECTION OF CLINICAL INDICATORS. ADVISOR: Prof. Dr. Orawon Chailapakul,Assoc. Prof. Dr. Weena Siangproh

This dissertation concentrated on the development of nanomaterials-based miniaturized platforms for the detection of some important compounds/indicators from environmental, pharmaceutical, and clinical application. This dissertation can be classified into two main parts: (1) development of nanomaterials-based miniaturized platforms for optical sensing application, and (2) development of nanomaterials-based miniaturized platforms for electrochemical sensing applications. In the first part, two sub-sections were discussed. For the first sub-section, the paper-based colorimetric sensor for chloride ion determination using silver nanoprisms was developed. Using a smartphone as an optical readout, the color change from the oxidative etching of the silver nanoprisms to the silver nanospheres induced by chloride ion can be monitored. In the second sub-section, a screen-printed electroluminescent displaymodified with graphene oxidewas engineered for optical sensing applications for the first time. The potential of the proposed device was extended for a variety of applications, including a basic lamp, an ionic concentration sensor, a humidity sensor, and a human breath sensor. In the second part, electrochemical sensors were also developed. In this part, two sub-sections were discussed in detail. For the first sub-section, an anti-fouling electrochemical sensor for vitamin D determinationusing graphene/Nafion nanocompositewas developed. A greatly enhance in analytical performance and the anti-fouling capability was obtained. Lastly, in the second sub-section, a paper-based sequential microfluidic device modified with graphene and gold nanoparticles was developed for the fluid delivery system. Various target compounds including ascorbic acid, serotonin, and alpha-fetoprotein were chosen as model analytes and tested by the developed platform. Results obtained from these miniaturized devices demonstrated here provided a good promising for on-field testing with excellent sensitivity, selectivity, and portability.

| | | |
|---|---|---|
| Department: | Department of Chemistry | Student's Signature ...................... |
| Field of Study: | Chemistry | Advisor's Signature ...................... |
| Academic Year: | 2018 | Co-advisor's Signature ................. |

# ACKNOWLEDGEMENTS

Abdulhadee Yakoh

# TABLE OF CONTENTS

จุฬาลงกรณ์มหาวิทยาลัย
CHULALONGKORN UNIVERSITY

# List of tables

# List of figures

จุฬาลงกรณ์มหาวิทยาลัย

CHULALONGKORN UNIVERSITY

# LIST OF ABBREVIATIONS

| | |
|---|---|
| AgNPs | Silver nanoparticles |
| AuNPs | Gold nanoparticles |
| GO | Graphene oxide |
| LOD | Limit of detection |
| LOQ | Limit of quantification |
| EL | Electroluminescence |
| LED | Light emitting diode |
| AC | Alternating-current |
| DC | Direct-current |
| $J_i(x)$ | Flux of species i (mol s$^{-1}$ cm$^{-2}$ ) at distance x from the surface |
| $D_i$ | Diffusion coefficient (cm$^2$/s) |
| $\partial C_i(x)/\partial(x)$ | Concentration gradient at distance x |
| $\partial \phi(x)/\partial(x)$ | Potential gradient |
| $z_i$ | Charge (dimensionless) of species i |
| $C_i$ | Concentration (mol cm$^{-3}$) of species i |
| $\textbf{V}(x)$ | Velocity (cm/s) |
| WE | Working electrode |
| RE | Reference electrode |
| CE | Counter electrode |

| | |
|---|---|
| A/V | Area per volume |
| n | Number of electrons |
| A | Electrode surface area ($cm^2$) |
| F | Faraday constant ($96487$ c $mol^{-1}$) |
| $\mathbf{V}$ | Scan rate (mV $s^{-1}$) |
| $i_{pc}$ | Cathodic peak current |
| $i_{pa}$ | Anodic peak current |
| $\Delta E_p$ | Peak separation |
| $E_{pc}$ | Cathodic peak potential |
| $E_{pa}$ | Anodic peak potential |
| $\alpha$ | Transfer coefficient |
| LSV | Linear scan voltammetry |
| CV | Cyclic voltammetry |
| DPV | Differential pulse voltammetry |
| SWV | Square-wave voltammetry |
| AdSWV | Adsorptive stripping square-wave voltammetry |
| $i_f$ | Forward current sample |
| $i_r$ | Reverse current sample |
| $i_f$-$i_r$ | Current difference between forward and reverse scan |
| PVC | Polyvinyl chloride |

| | |
|---|---|
| SPE | Screen-printed electrode |
| AgNPss | Silver nanosphere |
| AgNPrs | Silver nanoprisms |
| PADs | Paper-based analytical devices |
| SPR | Surface plasmon resonance |
| OPQPR | Out-of-plane quadrupole plasmon resonance |
| IPDPR | In-plane dipole plasmon resonance |
| $E^{\circ}$ | Standard reduction potential |
| $\Delta I$ | Mean color intensity difference |
| ITO | Indium tin oxide |
| TES | Top emission structure |
| BES | Bottom emission structure |
| GO | Graphene oxide |
| POC | Point-of-care |
| PET | Polyethylene terephthalate |
| RH | Relative humidity |
| S/B | Signal-to-background current ratio |
| PEDOT | Poly(3,4-ethylenedioxythiophene) |
| LC | Liquid chromatography |
| MS | Mass spectrometry |

| EIS | Electrochemical impedance spectroscopy |
|---|---|
| $C_{dl}$ | Double-layer capacitance |
| BDD | Boron-doped diamond electrode |
| $R_{ct}$ | Charge transfer resistance |
| GCE | Glassy-carbon electrode |
| AuPd | Gold-palladium nanocomposite |
| sePAD | Sequential microfluidic paper-based analytical device |
| μPAD | Microfluidic paper-based analytical device |
| rPAD | Storage paper-based analytical device |
| oPAD | Origami paper-based analytical device |
| AFP | Alpha-fetoprotein |
| NC | Nitrocellulose |
| CA | Chronoamperometry |
| AA | Ascorbic acid |
| 5-HT | 5-hydroxy-DL-tryptophan |
| $R^2$ | Correlation coefficient |
| NFC | Near-field communication |

# CHAPTER I

# INTRODUCTION

## 1.1 Introduction

In the developing world, the profits of operating all forms of analytical lab process in the reduced scale devices are now being discerned. Great benefits from their reduced cost, small chemical consumption, and portable make it proper to use for on-site analysis. These devices can serve as a screening tool in various formats, which will open up new possibilities and improve the quality of human being, especially in poor resource and remote areas. Currently, the vital criteria towards miniaturized platform are now focused on the device simplification and broad applicability. Therefore, myriad types of the miniaturized systems have been progressively developed for a range of analytical applications, including healthcare applications, pharmaceutical screening, environmental and food analysis. Meanwhile, current research is also center on the integration of the inorganic nanomaterials into a detection system of the miniature platform because they provide superior prospects for designing a sensitive sensing device. The remarkable properties from their nanometer scale dimension exceedingly enhance the sensitivity for the development of the sensor. Besides, a facile synthesis, as well as the mass production of the nanomaterials, enable them to unify into a variety application. Until now, different kinds of inorganic nanomaterial, including metal nanoparticles, carbon-based nanomaterials, and related nanocomposites have been broadly explored and particularly employed in optical and electrochemical detection.

Lately, metal nanoparticles have received tremendous attention due to their unique optical and electrical properties. Silver nanoparticle (AgNP), for instance, is broadly applied in the development of a colorimetric/optical sensor owing to its high

extinction coefficient, biocompatibility, and stability. The morphologically dependent plasmonic properties permit its use in abundant naked eyes colorimetric sensors. The ability to functionalize the surface of the AgNP can also tune the selectivity for chemical analysis. Gold nanoparticle (AuNP) is another common example of the metal nanoparticles that has been exploited not only in the colorimetric assay but also the electrochemical sensor. AuNP exhibits a very high ratio of surface-to-volume with good biocompatibility. In electrochemical aspects, AuNP is a good candidate for electrode modification due to its excellent conductivity enhancement and electrocatalytic activity for diverse biological species.

In addition, carbon materials are another of interest. Graphene and graphene oxide (GO)-based nanomaterials, for example, have gained remarkable attention owing to its exceptional features of the substantial surface area, mechanical flexibility, and chemical stability. Graphene, a single-layer sheet of $sp^2$ bonded carbon atoms with densely packed honeycomb crystal lattice, possesses a superior electrical conductivity which is extensively used in the electrochemical sensor. On the other hands, GO, a heavily decorated oxygen-containing functional group in the plane of carbon atoms, is often described as an electrical insulator due to the disruption of its $sp^2$ bonding networks. Functionalization the GO surface can basically alter the properties of the GO, which make it become much more adaptable for many applications.

Not only one phase of the nanomaterials but also the composite that cause researchers to consider using them in many sensing applications. A nanocomposite is a composite material, in which one of the components has at least one dimension that is around nanometer scale. Nanocomposite was designed to improve its physical properties and overcome the limitations of monolithic and microcomposites. Graphene nanocomposites, for example, have found to be one of the most

functional material with unprecedented performance and exhibited excellent synergistic activity toward the target molecule. Therefore, a number of publications have been reported based on the use of graphene nanocomposite.

In this research, different nanomaterial-based miniaturized devices for an optical and electrochemical detection system were developed for the determination of analytes of interest. Considering the method of detection, this research can be categorized into 2 main segments; optical and electrochemical sensor. Four developed platforms are described as follows;

1. Simple and selective paper-based colorimetric sensor for determination of chloride ion in environmental samples using label-free silver nanoprisms.

2. Screen-printed electroluminescent lamp modified with graphene oxide as a sensing device.

3. Fabrication and characterization of graphene-Nafion nanocomposite and its application in highly sensitive electrochemical sensor for vitamin D determination.

4. A 3D capillary-driven paper-based sequential microfluidic device for sensing applications.

Herein, powerful miniaturized devices were elaborately developed for the potential use in environmental, clinical, and pharmaceutical analysis. To demonstrate the sensing capabilities of the developed devices, the analytical figures of merit, as well as selectivity and interferences study were investigated. Finally, this research also includes a real-sample analysis and expands its functionality to an advancement format as conceptual ideas.

## 1.2 Research objective

Two main objectives of this research are as below:

1. To develop novel miniaturized platforms as analytical sensing tools for sensitive determination of environmental, pharmaceutical, and clinical indicators.

2. To improve the performance of the developed miniaturized devices using different nanomaterials.

## 1.3 Scope of the research

To reach the research goals in this dissertation, the scope of the research was set to achieve the most sensible platform for each miniaturized device. First of all, the device configuration and working operation were designed and fabricated using a simple method including wax-printing and screen-printing method. Various experimental conditions affecting detection performance were also optimized. Under optimal conditions, the analytical performance of the developed platform including linear range, limits of detection (LOD) and quantification (LOQ), and reproducibility were investigated. In addition, most of the experiments were further studied the effect of interferent and applied the developed sensor to real sample analysis. To confirm the accuracy of the sensor, the analysis data from the developed assay were then compared with those analyzed with the conventional technique.

There are five chapters in this dissertation. Chapter I is the introduction to this research. Chapter II describes the theory for the detection method (including optical and electrochemical detection) and fabrication technique of the device. Next, chapter III reports on the development of the optical sensors while chapter IV

reports on the development of the electrochemical sensors. Lastly, chapter V is the conclusions and future perspectives for this dissertation.

CHAPTER II

THEORY

## 2.1 Detection Method

One crucial step for analytical sensing devices is the capability of the readout to quantify the amount/concentration of the target analyte. Numerous detection methods compatible with miniaturized devices have been reported over years. However, two of the most common methods which are extensively applied in miniaturized platforms are optical and electrochemical detection. These two techniques offer excellent sensitivity and show a good compatibility with a portable device and miniaturized systems. Therefore, the optical and electrochemical methods were selected and discussed in this dissertation.

### 2.1.1 Optical detection

Many optical detection techniques have been implemented with miniaturized systems, such as colorimetry, luminescence, absorption spectroscopy, IR spectroscopy, Raman spectroscopy, and nuclear magnetic resonance (NMR) spectroscopy. To achieve the criteria of a simple and portable sensing device, colorimetry and luminescence were chosen as the readout among other techniques owing to their benefits of a simple operation and uncomplicated instrument.

#### 2.1.1.1 Colorimetry

Over a decade, colorimetry is found to be the simplest detection method in terms of the device operation and visual interpretation. Colorimetry is the method for determining the amount of the target compounds with the aid of a colorimetric

agent. Basically, the color intensity is proportional to the concentration of the analyte. Moreover, the change in the color intensity can be monitored through naked eyes or by the quantitative readouts (e.g. digital camera, scanners or smartphones) such as the work published by Lopez-Ruiz et al. as shown in figure 2.1 [1].
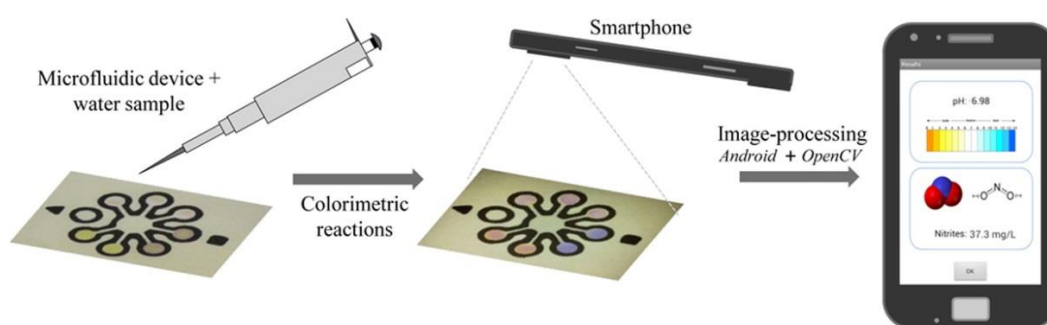


**Figure 2.1** A paper-based colorimetric device for simultaneous colorimetric detection of pH and nitrite using a smartphone as an image processor [1].

### 2.1.1.2 Luminescence

Luminescence is a process of giving off light without obtaining or generating heat. The luminescence differs from incandescence, which is light emitted by a substance as a result of heating. This phenomenon can result from many sources, such as chemical reaction, electrochemical reaction, or a mechanical action on a solid. [2] The example types of luminescence are as follows,

1. Chemiluminescence: the light emitted as a result of a chemical reaction.

    1.1 Bioluminescence: the light emitted as a result of biochemical reactions in a living organism.

    1.2 Electrochemiluminescence: the light emitted as a result of an electrochemical reaction.

2. Photoluminescence: the light emitted as a result of absorption of photons.

2.1 Fluorescence: photoluminescence emitted as a result of singlet-singlet electronic relaxation (typical lifetime: nanoseconds).

2.2 Phosphorescence: photoluminescence emitted as a result of triplet-singlet electronic relaxation (typical lifetime: milliseconds to hours).

2.3 Raman emission: photoluminescence emitted as a result of inelastic light scattering, (lifetime: nanoseconds).

3. Electroluminescence: the light emitted as a result of an electric current passed through a substance.

4. Crystalloluminescence: the light emission produced during crystallization.

5. Mechanoluminescence: the light emitted as a result of a mechanical action on a solid.

6. Radioluminescence: the light emitted as a result of bombardment by ionizing radiation.

In this dissertation, the electroluminescence technique is of interested. The operating principle underlying this device will be discussed in detail.

### 2.1.1.2.1 Background of electroluminescence

The term "electroluminescence" is an optical and electrical phenomenon in which a material emits light in response to the passage of electric current. Typically, the materials used in electroluminescence (EL) is an inorganic polycrystalline solid

instead of the single crystal materials used in the light emitting diode (LED). The polycrystalline nature of the EL powder plays a key role for the uniform light emission in EL. The emitted light is caused by substantial grains or crystals. Therefore, even a less ideal material than the single crystal materials of LED is capable to produce extremely reproducible light [3].

Generally, the inorganic electroluminescence can be classified based on the form of the driving voltage into two groups; direct-current electroluminescence (DCEL) and alternating-current electroluminescence (ACEL) [4]. However, it has been reported that under the DC driving voltage, the glowing would stop as soon as the current stop. This is because DC moves only in one direction (Figure 2.2). Therefore, the light emission would begin and terminate rapidly as the current passed. On the other hands, for continuous glow, it requires a constant supply of electrical current. With an AC driving voltage, the electrical current moves back and forth between the negative and positive poles of the circuit. This alternating polarity means that electricity constantly flows through the circuit, giving the EL a constant electrical supply. In addition, AC offers higher voltages than DC because AC can be stepped up or down using transformers. The higher the voltage, the more electron excitation, which in turn yields a brighter emission.
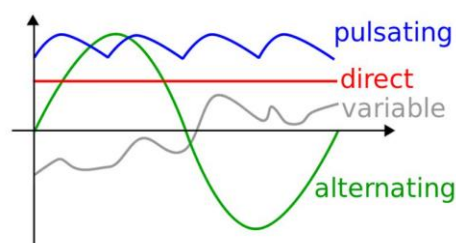


**Figure 2.2** Representation of visual difference between DC and AC voltage [5].

### 2.1.1.2.2 Structure and materials of ACEL device

Initially, ACEL was first demonstrated in the first era of EL device by Sylvania [4]. A standard structure of an ACEL is presented in Figure 2.3. This ACEL device is constructed by various layers of the screen-printed ink composition. The EL structure consists of 4 layers including a top metal electrode, dielectric, phosphor, and a transparent electrode layer supported on a substrate (glass or flexible plastic). Until now, the most widely used powder phosphors by an AC electric field is mainly limited to the group of ZnS type. The color of the emitted light depends on the activator of the ZnS phosphors. The most common ZnS phosphor is ZnS: Cu, Cl. The Cu activator is used as an acceptor in this material and is responsible for the color of the emitted light, whereas Cl acts as a donor. This phosphor layer is sandwiched between two metal plate electrodes, one of which is transparent. The embedding dielectric of $BaTiO_3$ in the device is used to increase the stability and protect the device against the device breakdown.
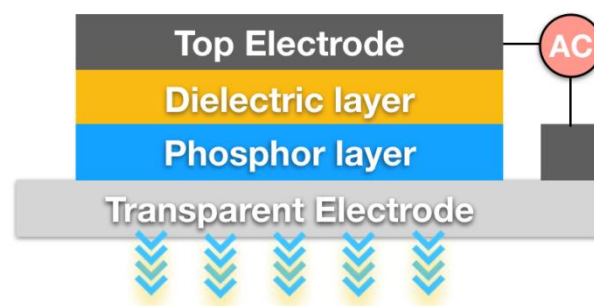


**Figure 2.3** A standard structure of ACEL device.

### 2.1.1.2.3 The mechanism of light emission for ZnS ACEL device

Until now, several theories have been proposed to explain the mechanism of the ZnS types in ACEL device. However, the most popular model is the bipolar field

emission that was proposed by Fisher [6]. It was observed under an optical microscope that there were many dark precipitates inside the phosphor particles (Figure 2.4). This is because ZnS powder is generally firing at high temperatures. When the powders are chilled, there is a phase transition to the cubic zinc-blende structure. Copper favorably precipitates on defects formed in the hexagonal-to-cubic transformation with the decrement of their solubility in ZnS. The Cu forms thin embedded $Cu_{2-x}S$ needles in the crystal matrix, which is known to be a p-type semiconductor with high conductivity (Figure 2.5). The heterojunction is formed between these precipitates and ZnS phosphor [3].
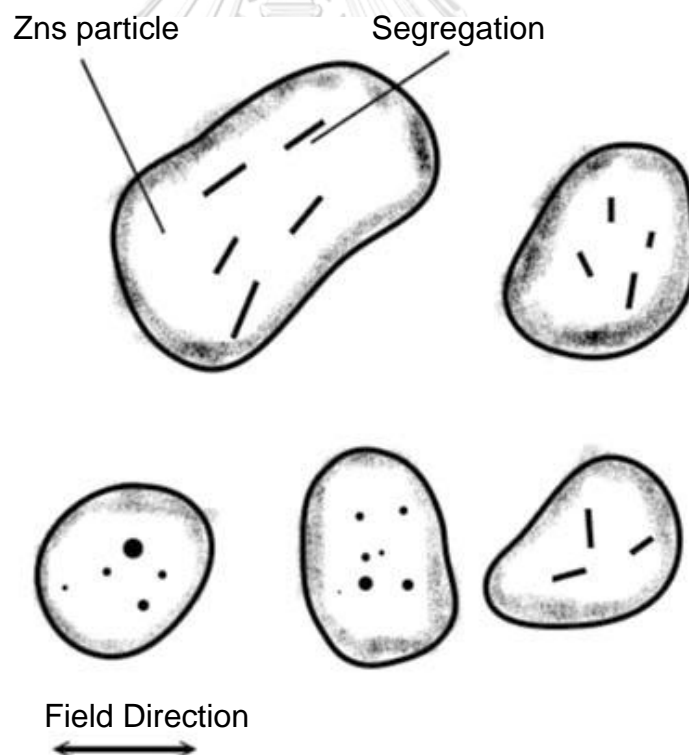


**Figure 2.4** A standard structure of ACEL device.
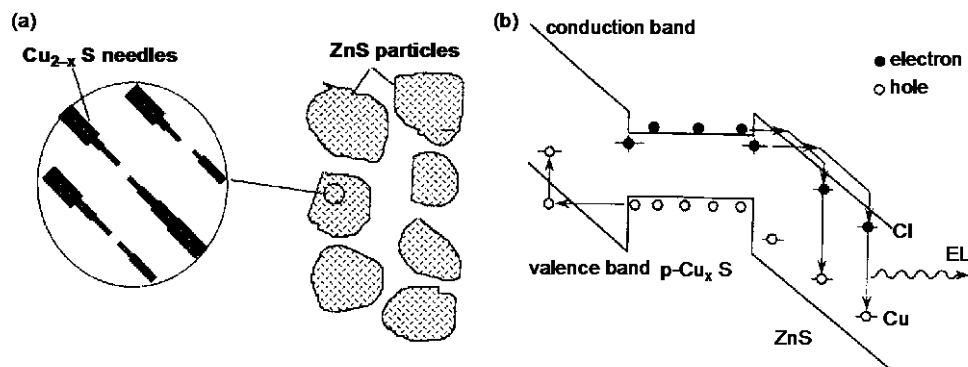
**Figure 2.5** EL emission mechanism and schematic energy-band diagram of ac powder EL devices: (a) $Cu_{2-x}S$ needles (b) energy-band diagram [3].

When an electric field is applied to the phosphor layer, relatively high electric fields will be intensified on the tips of $Cu_{2-x}S$ conducting needles (Figure 2.6). This strong electric field will cause the tunneling of the holes from one end of the needle and electrons from the other to the ZnS: Cu, Cl lattice. As shown in figure 2.7, the electrons are trapped in shallow traps in Cl donor sites, while the holes are captured by the Cu recombination centers (acceptor sites). When the field is reversed, the emitted electrons recombine with the trapped holes to produce the light [3].
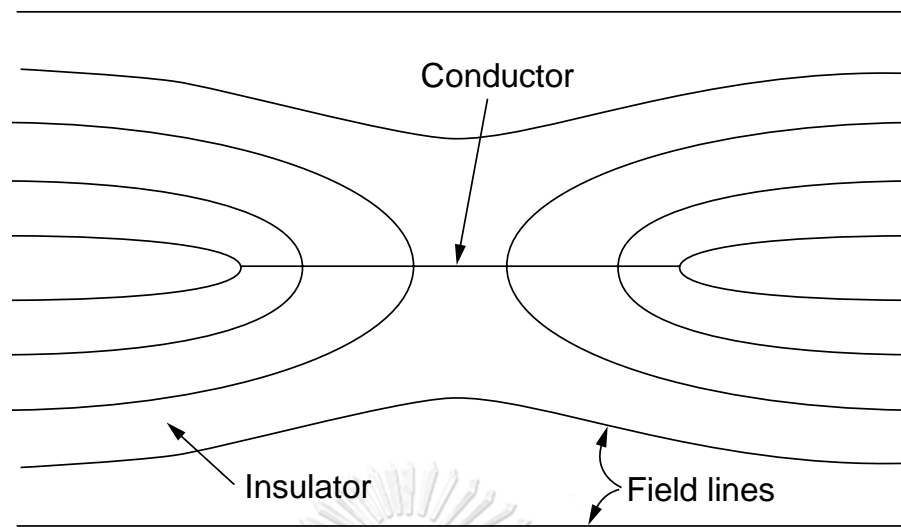
**Figure 2.6** Conducting needle embedded in the insulator. Geometrical field intensification occurs at the ends [3].
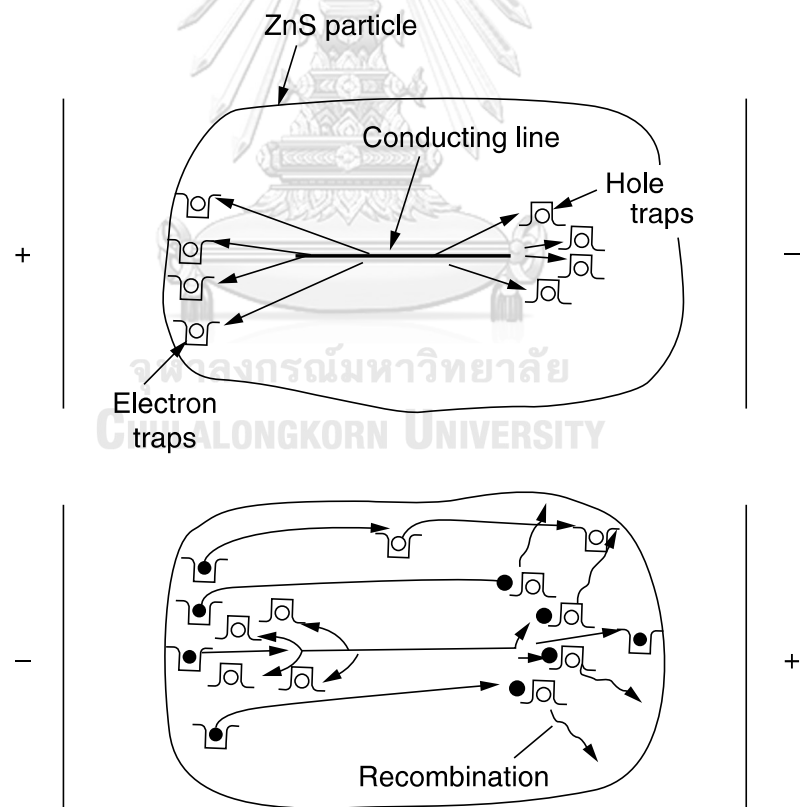


**Figure 2.7** Illustration of the basic principle of field-emission model at field application (above) and field reversal (below) [3].

### 2.1.2 Electrochemical detection

The miniaturized device coupled with electrochemical detection offers a sensitive and selective determination platform for measuring the analyte of interest. This detection method exhibits good advantages of the fast analysis, high sensitivity, compact size instrument, and low power requirement. In electrochemical systems, the event that occurs at the electrode/electrolyte interface when an electrical potential is applied and current passes is of concerned.

#### 2.1.2.1 Faradaic and nonfaradaic processes

There are 2 types of processes occur at electrode surface [7]. First is the reaction in which charges (electrons) are transferred across the electrode-solution interface. This electron transfer causes reduction or oxidation to occur. Because such reaction is governed by Faraday's law, they are called faradaic processes. Under some conditions, a given electrode-solution interface will show a range of potentials where no charge-transfer reactions occur because such reactions are thermodynamically or kinetically unfavorable. However, processes such as adsorption and desorption can occur, and the structure of the electrode-solution interface can change with changing potential or solution composition. These processes are called nonfaradaic processes. Although charge does not cross the interface, external currents can flow (at least transiently) when the potential, electrode area, or solution composition changes.

### 2.1.2.2 Electrochemical cell

In electrochemical system, electrochemical cell in which faradaic currents are flowing can be classified as either galvanic or electrolytic cell [7]. As shown in figure 2.8, a galvanic cell is one in which reactions occur spontaneously at the electrodes. These cells are often employed in converting chemical energy into electrical energy. An electrolytic cell, in contrast to a galvanic cell, requires an external source of electrical energy for operation. This cell is frequently employed to carry out desired chemical reactions by expending electrical energy. In discussing cell, one calls the electrode at which reduction occur the cathode, and the electrode at which oxidation occur the anode. A current in which electrons cross the interface from the electrode to a species in solution is a cathodic current, while electron flow from a solution species into the electrode is an anodic current. In an electrolytic cell, the cathode is negative with respect to the anode; but in a galvanic cell, the cathode is positive with respect to the anode.
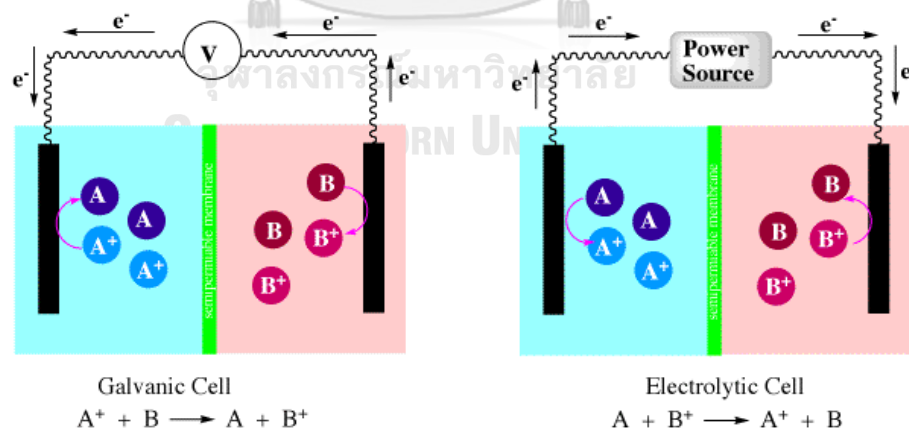


**Figure 2.8** Galvanic (left) and electrolytic (right) cells [8].

### 2.1.2.3 Modes of mass transfer

It is important to understand the mass transfer modes because it plays a key role in electrochemical dynamics. Theoretically, mass transfer, that is, the movement of material from one location in solution to another, arises either from differences in electrical or chemical potential at the two locations or from the movement of a volume element of the solution [7]. There are three modes of mass transfer as follows:

1. Migration is the movement of a charged body under the influence of an electric field (a gradient of the electrical potential).

2. Diffusion is the movement of a species under the influence of a gradient of chemical potential (i.e., a concentration gradient).

3. Convection is a stirring or hydrodynamic transport. Generally, fluid flow occurs because of natural convection (convection caused by density gradients) and forced convection and may be characterized by stagnant regions, laminar flow, and turbulent flow.

Mass transfer to an electrode is governed by the Nernst-Planck equation, written for one-dimensional mass transfer along the x-axis as

$$J_i(x) = -D_i \frac{\partial C_i(x)}{\partial x} - \frac{z_i F}{RT} D_i C_i \frac{\partial \phi(x)}{\partial x} + C_i V(x) \tag{2.1}$$

where $J_i(x)$ is the flux of species i (mol s$^{-1}$ cm$^{-2}$) at distance x from the surface, $D_i$ is the diffusion coefficient (cm$^2$/s), $\partial C_i(x)/\partial(x)$ is the concentration gradient at distance x, $\partial \phi(x)/\partial(x)$ is the potential gradient, $z_i$ and $C_i$ are the charge (dimensionless) and concentration (mol cm$^{-3}$) of species i, respectively, and $V(x)$ is

the velocity (cm/s) which a volume element in solution moves along the axis. The three terms on the right-hand side represent the contributions of diffusion, migration, and convection, respectively, to the flux.

### 2.1.2.4 Electrochemical techniques

Electrochemistry comprises techniques that use a measurement of potential, current, or charge to determine the concentration or the chemical reactivity of analytes. Electroanalytical methods can be classified into several categories depending on which aspects of the cell are controlled and which are measured. In brief, there are 4 main electrochemical techniques including potentiometry, coulometry, amperometry, and voltammetry (Figure 2.9).
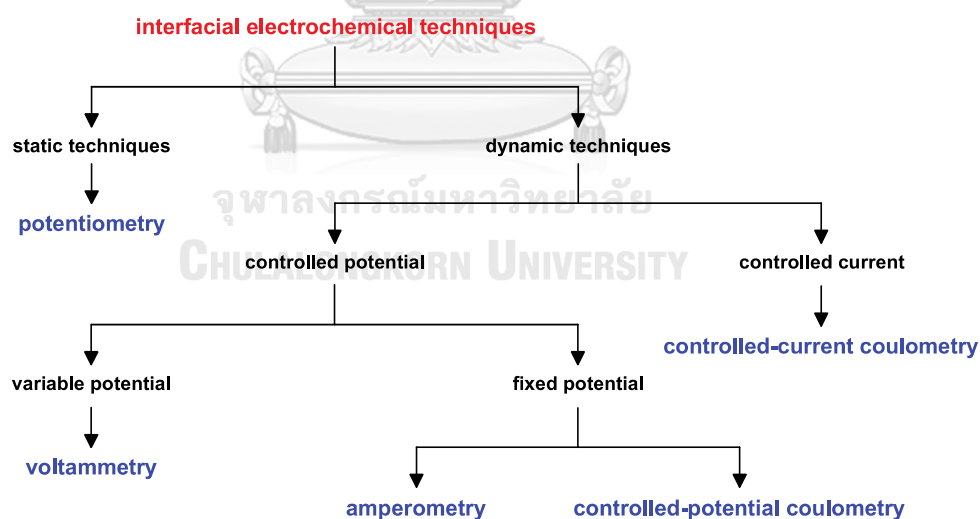


**Figure 2.9** The family tree of interfacial electrochemical techniques [9].

Herein, the voltammetry and amperometry techniques were used as an electrochemical method in this research. Therefore, an overview of these two techniques will be described in this chapter.

### 2.1.2.4.1 Voltammetry

Electrochemical techniques that depend on the measurement of current as a function of applied potential are called voltammetric methods. These techniques are based on the measurement of current in an electrochemical cell under conditions of complete concentration polarization in which the rate of oxidation or reduction of the analytes is limited by the mass transfer rate of the analyte to the surface of an electrode. Basically, to enhance polarization, the size of the working electrode (WE) is relatively small in a few square millimeters or micrometers scale. Such circumstances are known as small A/V conditions.

For the electroanalytical purpose, several types of voltammetry are in current use. For voltammetry systems, the voltage of the WE is varied while the current response is monitored. As presented in figure 2.10, various voltage-time functions (waveform) can be applied to the electrode. More information on each technique will be described in detail.
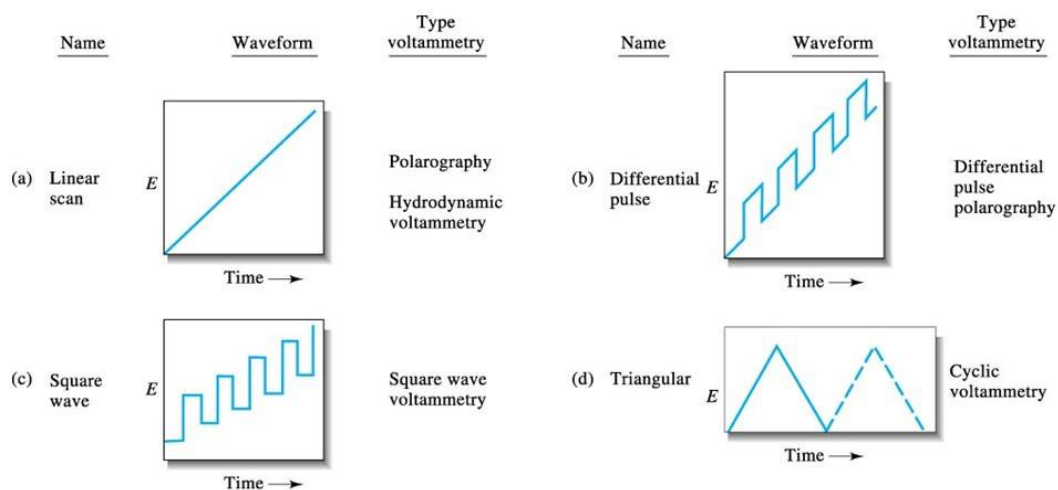
**Figure 2.10** Potential waveforms for (a) linear scan, (b) differential pulse, (c) square-wave, and (d) cyclic voltammetry [10].

### 2.1.2.4.1.1 Linear scan voltammetry (LSV) and cyclic voltammetry (CV)

The simplest voltammetry technique is an LSV or CV which frequently used as an initial study of new systems to obtain qualitative information about oxidation/reduction reactions of electroactive species. In the LSV measurement, the WE potential is ramped linearly versus time (the rate of the potential change over time is called a scan rate (V/s)). However, for the CV measurement, when the potential reached the switching potential, the WE potential is then ramped in the opposite direction to a starting potential (figure 2.11). This can be repeated as needed. The resulting voltammogram is illustrated in Figure 2.11b. When the potential moves past $E^{0'}$, the reduction of the electroactive species begins, and the cathodic current starts to flow. As the potential continually grows to more negative, the concentration of the electroactive species at the surface decreases. At this point, mass transfer of an electroactive species at the electrode surface reaches a maximum rate, and then it declines as the depletion effect sets in. When the

potential is sweeping back in a positive direction and passing $E^{0'}$, the reduced species will be re-oxidized and caused the anodic current flow.
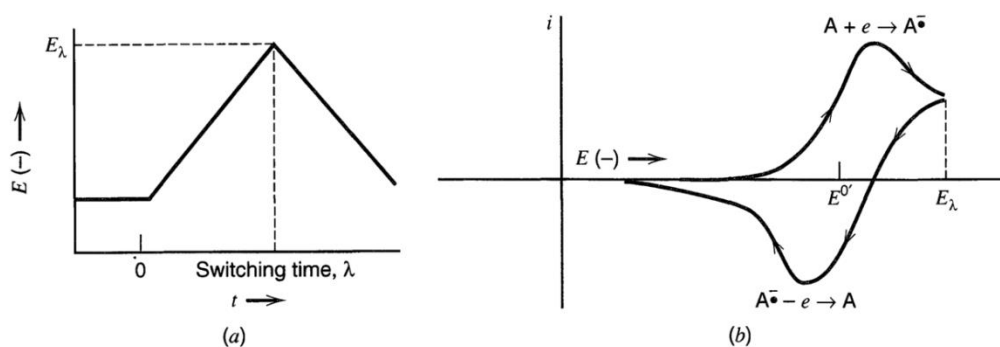


**Figure 2.11** (a) Cyclic potential sweep and (b) Resulting cyclic voltammogram.

For a Nernstian (reversible) systems, the peak currents (cathodic peak current ($i_{pc}$) and anodic peak current ($i_{pa}$) are proportional to the concentration of an analyte and the square root of the scan rate, which can be described by Randles-Sevick equation [7].

$$i_{p(a,c)} = (2.69 \times 10^5) \, n^{3/2} \, A \, F \, C \, D^{1/2} \, V^{1/2} \qquad (2.2)$$

Where      n:      number of electrons

A:      electrode surface area ($cm^2$)

F:      Faraday constant ($96487 \, c \, mol^{-1}$)

C:      concentration ($mol \, cm^{-3}$)

D:      diffusion coefficient ($cm^2 \, s^{-1}$)

V:      scan rate ($mV \, s^{-1}$)

The peak separation ($\Delta$Ep, mV) between anodic peak potential ($E_{pa}$) and cathodic peak potential is approximately equal to

$$\Delta Ep = Ep_a - Ep_c = 59/n \qquad (2.3)$$

For totally irreversible systems, the peak current is found to be:

$$i_p = (2.99 \times 10^5)\, \alpha^{1/2}\, A\, C\, D^{1/2}\, V^{1/2} \qquad (2.4)$$

Where $\alpha$:    transfer coefficient

### 2.1.2.4.1.2 Differential pulse voltammetry (DPV)

DPV is one of the voltammetry measurements that used to make a derivative of linear scan voltammetry or staircase voltammetry, with a set of voltage pulses superimposed on the potential linear scan, as previously shown in figure 2.10. In this technique, the current is monitored before each potential change. By taking the current samples before the potential change, the effect of the charging current can be effectively decreased [7]. The resulting voltammogram is plotted between the current difference as a function of potential as depicted in figure 2.12.
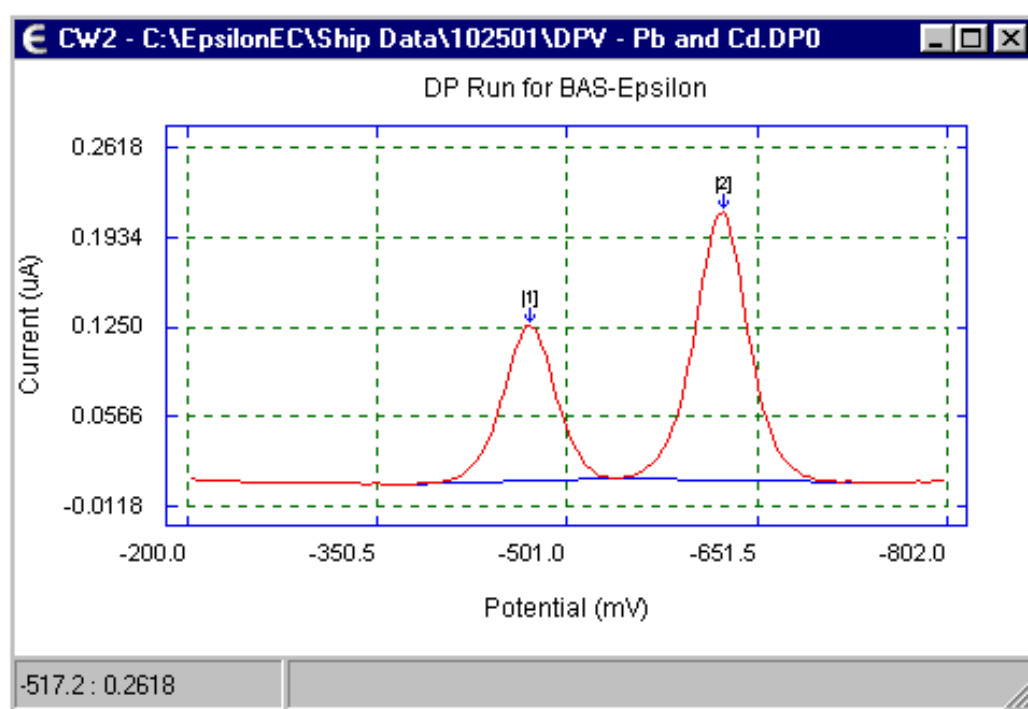
**Figure 2.12** A typical differential pulse voltammogram [11].

DPV is frequently used to study the electrochemical properties of the analytes due to the advantages of 1) the effect of the charging current is minimized, thus good sensitivity is gained 2) only the faradaic current is extracted, thus electrode reactions are interpreted more accurately. In addition, the current responses from the DPV voltammogram can be treated quantitatively in a straightforward manner since the peak current is proportional to the concentration.

### 2.1.2.4.1.3 Square-wave voltammetry (SWV)

SWV technique provides an exceptional versatility for electrochemical measurement. This method combines the best features of several pulse methods, including the background suppression and sensitivity improvement from DPV and the capability to examine products in much the manner of reverse pulse voltammetry.

As presented earlier in figure 2.10, the potential waveform is a bipolar square wave superimposed on the staircase. In this sense, it gives rise to the name of the method. The current is sampled twice per cycle, at the end of each pulse. The forward current sample ($i_f$) results from the first pulse per cycle, which is in the direction of the staircase scan. The reverse current sample ($i_r$) is taken at the end of the second pulse, which is in the opposite direction. Consequently, a current difference between the forward and reverse scan ($i_f$-$i_r$) is calculated and plotted versus the potential [7]. The resulting SWV voltammogram is shown in figure 2.13.
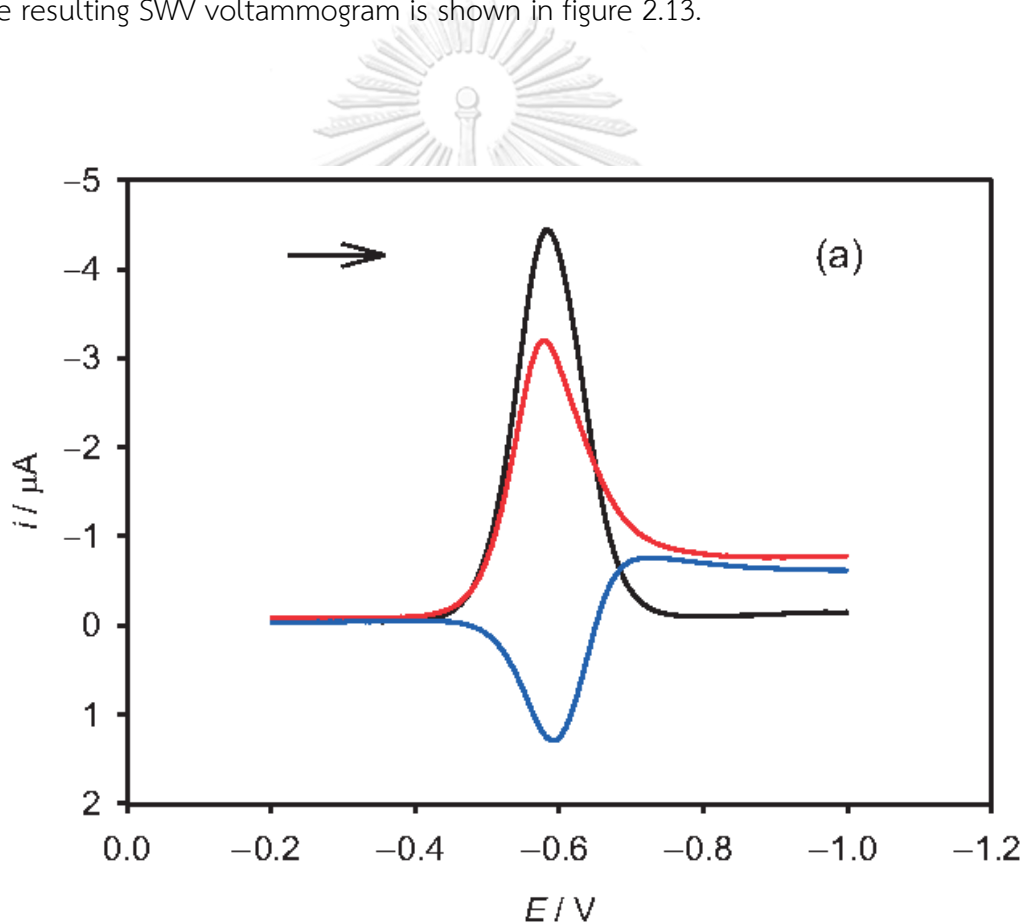


**Figure 2.13** Square wave voltammogram of $Eu^{3+}$ (0.5 mmol $dm^{-3}$) in 0.01 mol $dm^{-3}$ $HClO_4$ and its forward (red), backward (blue) and different current (black) [12].

### 2.1.2.4.2 Amperometry

Amperometry, an electrochemical technique in which the current is measured as a function of time while the electrode potential (potential difference) is kept constant. The excitation waveform and resulting current response are displayed in figure 2.14. For quantitative measurement, the resulting current is proportional with the analyte concentration. Typically, this electrochemical detection method has been broadly coupled with the flow-based and chromatographic system. The main advantage of this technique is the time resolution which is only limited to the data collection frequency of the equipment. However, a disadvantage is mainly because of a poor selectivity since all species with an oxidation/reduction potential lower (oxidation) or higher (reduction) than the applied potential will be oxidized/reduced and contributed the current. Thus, an optimal applied potential that provides the highest ratio of S/B (signal-to-background) will be selected.
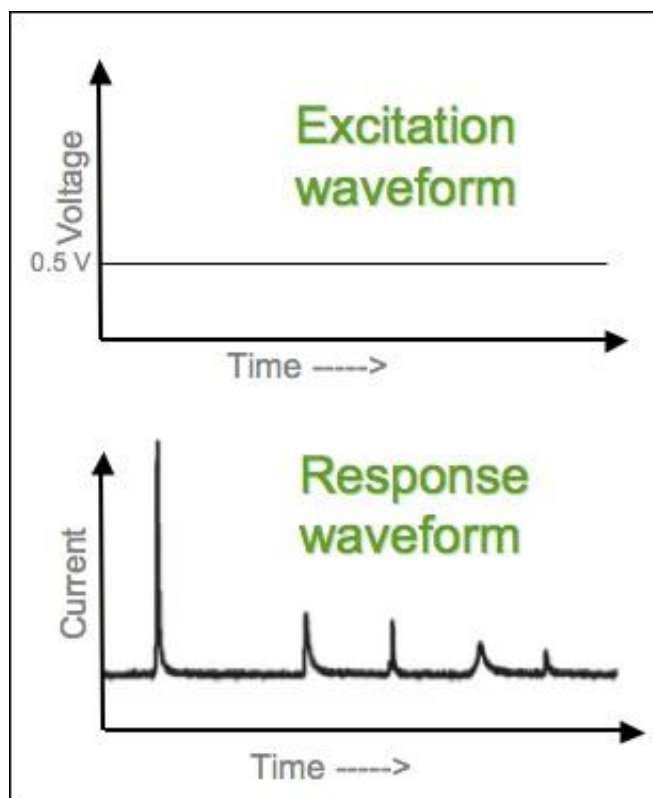
**Figure 2.14** The excitation waveform and current response from amperometric detection [13].

### 2.1.2.4.3 Electrochemical Impedance Spectroscopy (EIS)

Apart from the voltammetry and amperometry, The utilization of EIS technique has increased considerably in the past few years owing to its capability to interpret physical and electronic properties of electrochemical systems such as electron transfer rate constants, charge transfer resistances, and capacitance. In theory, impedance is generally the opposition force to electrical current in a circuit and is measured in the same units as resistance. However, resistance is dissimilar to impedance because resistance follows Ohm's law and is observed in DC circuits where the resistance is technically the impedance with zero phase angle, since the current is not alternating [14]. For EIS experiment, a fixed sinusoidal voltage is applied by a potentiostat across 3 electrodes containing a solution under

investigation. For the data presentation, real and imaginary impedance components are plotted against one another in Nyquist plots (Figure 2.15) which have to be interpreted properly to deduce solution resistances, charge transfer resistances and Warburg impedance as well as time constants. EIS circuits are normally simplified into circuit diagrams to help users understanding the different components contributing to the overall impedance of the circuit. For instance, in an electrochemical experiment, impedance will arise from the solution resistance ($R_s$), double layer charging at the electrode surface ($C_{dl}$), charge transfer resistance ($R_{ct}$), and the Warburg Element ($Z_w$).
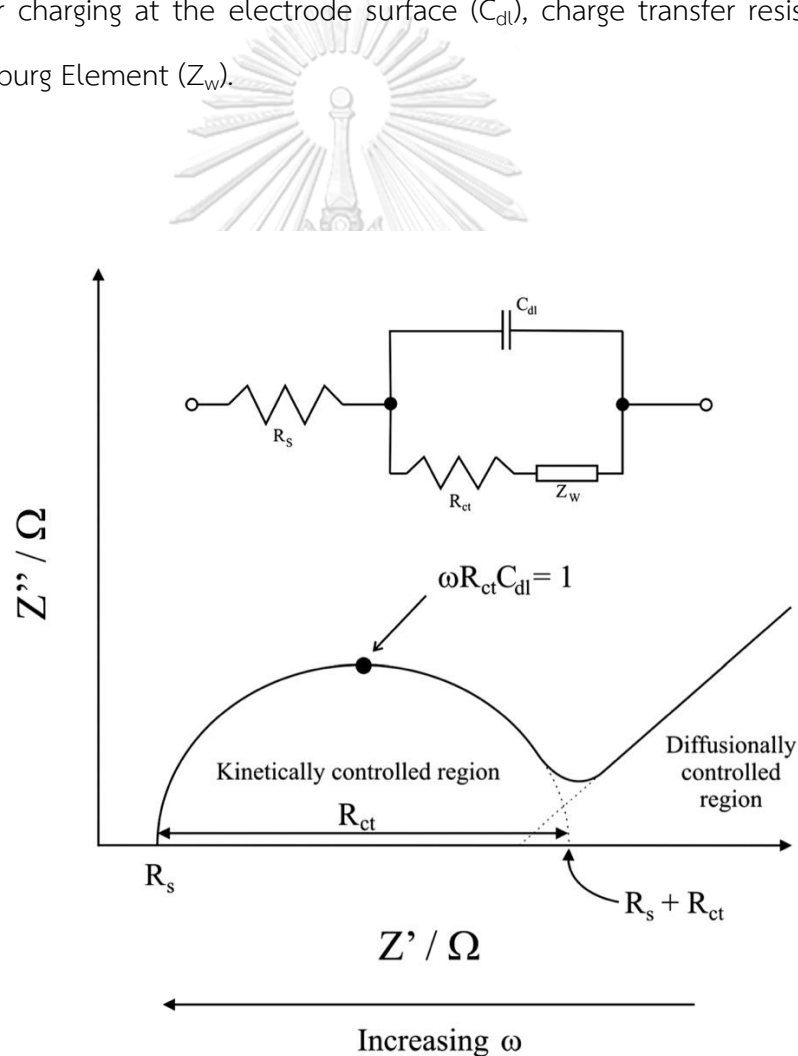
**Figure 2.15** Simple Randles equivalent circuit for an electrochemical cell [14].

**2.2 Methods for the device fabrication**

Up to now, several fabrication methods for different miniaturized platforms have been established. Although a simple fabrication is the main criteria for the selection of a method. The realization of an advanced device with enhanced functionality has been pursued. In this research, common methods to fabricate optical and electrochemical sensors will be discussed.

**2.2.1 Wax-printing method**

Previously, the photoresist has been used to define the flow boundaries of the device; however, the complicated procedures and the cost of a photoresist make this conventional method less convenient to use. Wax, in particular, provides a low-cost and easily fabricated method. With today's technology, papers or printable substrates (e.g. polyvinyl chloride (PVC) sheet or plastic films) can be directly printed with the commercial wax-based ink office printer to create a wax barrier on substrates (Figure 2.16). The printed-pattern is readily melted when heated, allowing the wax to penetrate into a paper pore, yielding a three-dimensional hydrophobic barrier. Successful fabrication with the wax-printing method has led to the development of devices with various designs, channel sizes, and allowed for mass production.
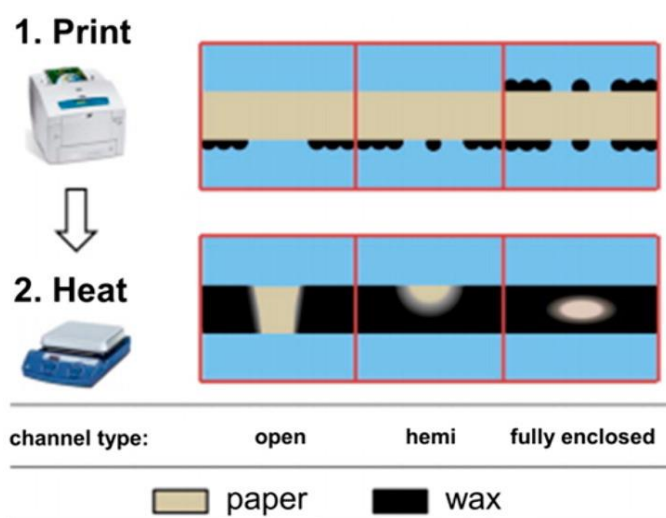
**Figure 2.16** Schematic illustration of a wax printing process to create open, hemi- and fully-enclosed channel [15].

### 2.2.2 Screen-printing method

Printing conductive material for preparing an electrode has been of attention regarding the electrochemical, optoelectrical, and related applications. Typically, the screen-printing method has found to be the most promising approach to fabricate an electrode onto devices or external screen-printed electrodes. The conductive paste or ink can be directly pressed onto the device through a screen or stencil to form patterned electrodes and then cured. The screen-printed electrode (SPE) is in growing demand for the development of a portable and disposable device. In addition, the miniaturized geometry of SPE and versatility for the electrode modification enable it to use for on-site analysis without common problems found from classical solid electrodes, especially their tedious cleaning steps.

Using screen-printing method, the whole electrodes, including a working electrode (WE), a counter electrode (CE), and a reference electrode (RE), can be printed on the same substrate as shown in figure 2.17. Briefly, the WE is the principal electrode at which the analyte is oxidized or reduced, while the other half

electrochemical reaction occurs at CE vice-versa. In this sense, carbon ink is basically used for WE and CE fabrication. For RE, it functions as a reference in measuring and controlling the WE's potential. The most suitable material that can be printed as an RE is Ag/AgCl ink, thanks to its stability.
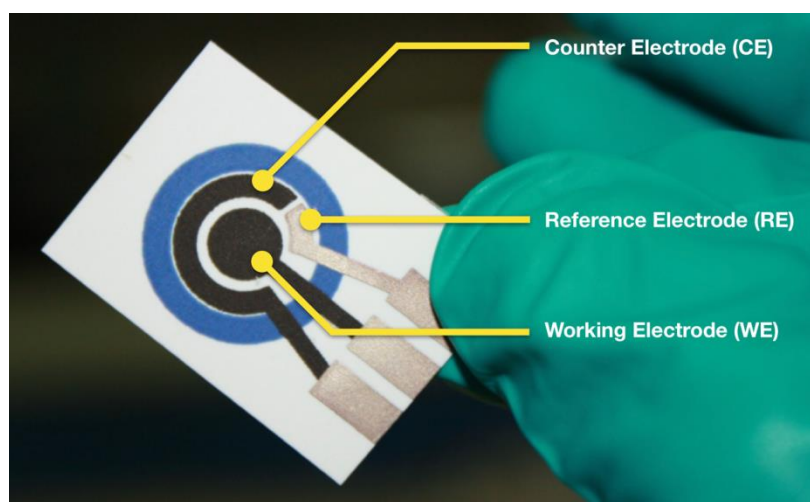


**Figure 2.17** Counter, reference, and working electrode for a screen-printed electrode (SPE).

# CHAPTER III

# DEVELOPMENT OF NANOMATERIALS-BASED MINIATURIZED PLATFORMS

# FOR OPTICAL SENSING APPLICATIONS

This chapter is divided into two main parts. Part I (section 3.1) reports on a simple and selective paper-based colorimetric sensor for determination of chloride ion in environmental samples using label-free silver nanoprisms. Part II (section 3.2) reports on a screen-printed electroluminescent lamp modified with graphene oxide as a sensing device.
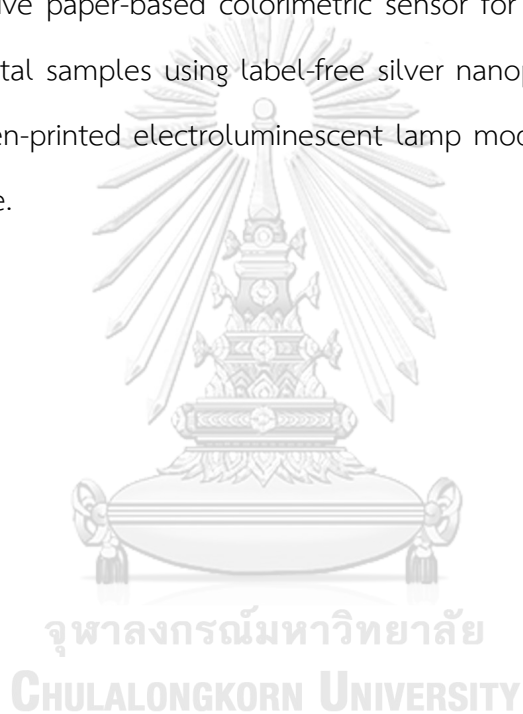
PART I

## 3.1 Simple and Selective Paper-Based Colorimetric Sensor for Determination of Chloride Ion in Environmental Samples Using Label-Free Silver Nanoprisms

Abdulhadee Yakoh[a], Poomrat Rattanarat[a], Weena Siangproh[b*], and Orawon Chailapakul[a,c*]

[a] Electrochemistry and Optical Spectroscopy Center of Excellence (EOSCE), Department of Chemistry, Faculty of Science, Chulalongkorn University, 254 Phayathai Road, Patumwan, Bangkok 10330, Thailand

[b] Department of Chemistry, Faculty of Science, Srinakharinwirot University, Sukhumvit 23, Wattana, Bangkok 10110, Thailand

[c] Center for Petroleum, Petrochemicals and Advanced Materials, Chulalongkorn University, 254 Phayathai Road, Pathumwan, Bangkok 10330, Thailand

* Corresponding author

**Abstract**

   Simple and selective paper-based colorimetric sensors using silver nanoprism (AgNPrs) were conveniently fabricated and developed for the determination of chloride ions (Cl$^-$) contaminated in the environment. Samples containing different concentrations of Cl$^-$ were analyzed. The analysis is based on the oxidative etching of the AgNPrs into smaller silver nanospheres (AgNPss) by Cl$^-$. In the presence of Cl$^-$, the distinctive color change of the AgNPrs from dark-violet to red was rapidly visualized by the naked eye in 5 minutes without the requirement of surface modification. For quantitative measurement using image processing, a good linear relationship ($R^2$ = 0.996) between logarithmic of Cl$^-$ concentration and the average mean color intensity was obtained in the range of 10-1000 mg L$^{-1}$ with a detection limit of 1.3 mg L$^{-1}$. The developed sensors were investigated for precision, accuracy, and sensitivity and validated by the classical method. Statistical analysis proved that the developed sensors were precise, sensitive and accurate and can be used effectively for the analysis of Cl$^-$ in natural waters.

**Keywords:** Chloride ion (Cl$^-$), Silver nanoprisms (AgNPrs), Paper-based analytical devices (PADs), Colorimetric detection

### 3.1.1 Introduction

Chlorides are widely distributed in nature as salts of sodium, potassium and calcium. Chloride ion ($Cl^-$) is one major anion that plays a critical parameter in various fields. Importantly, $Cl^-$ sensing in an environment is required for quality control and management purpose, in particular the content of $Cl^-$ in water that has been well monitored. Although a high level of $Cl^-$ in an environment may not cause harmful health effect on human, it can cause severe corrosion in metallic pipes. Besides, $Cl^-$ can also react with metal ions to form soluble salts, thus increasing levels of metals in drinking-water [16]. Therefore, the maximum allowable $Cl^-$ level of 250 mg $L^{-1}$ has been established by the World Health Organization (WHO) for drinking water and natural water [16]. Therefore, reliable, sensitive, simple, rapid and accurate analytical methods are necessary in the analysis of these types of water.

The growing demand in environmental analyses has stimulated the development of several methods. Various analytical approaches have been reported for $Cl^-$ determination including ion chromatography [17, 18], electrochemistry [19, 20], spectrophotometry [21-26], and colorimetry [27]. Among them, the spectroscopic procedure with mercury(II) salt is the most frequently used and recommended by the Association of Official Analytical Chemists (AOAC) as the standard method for $Cl^-$ determination in natural water [28]. However, the main drawbacks of this method are the use of a highly toxic and expensive reagent, time-consuming process and costly instruments which are inconvenient for routine work and for on-site monitoring. Therefore, to avoid the utilization of the hazardous reagent and to reduce toxic waste generation, the development of a greener, simpler, and less expensive alternative approach has become increasingly attractive and necessary. Recently, paper-based analytical devices (PADs) have been exploited as a miniaturized analytical platform for an economical and portable sensing application. Paper-based

sensors can be advantageous for applications in diagnostics, food safety, and environmental monitoring due to the advantages of natural abundance, simplicity, disposability, low sample-reagent usage and suitability for routine analysis [29-31]. Most of the PADs applications to date have emphasized colorimetric assays, which are well suited to be used as a detection method in paper-based devices. Color change obtained from the chemical reaction between a target analyte and colorimetric agent can readily be detected by the naked eye, a conventional digital camera or even with smartphones.

In the past few decades, noble metallic nanoparticles (NPs) such as gold nanoparticles (AuNPs) and silver nanoparticles (AgNPs) have received considerable attention owing to their distinctive properties including optical and electronic properties, biocompatibility and long-term stability. Their excellent optical properties enable brilliant color display for sensing applications which can be visualized by the naked eye with no need for an additional instrument. Compared with AuNPs, AgNPs are much cheaper and display stronger surface plasmon absorption (SPR) resonance with an ultrahigh extinction coefficient [32-34], which in principle promises a wider range of potential applications. Therefore, AgNPs have been broadly utilized for the colorimetric sensor of myriad substances [35-41]. Recently, among other shapes, silver nanoprisms (AgNPrs) have become progressively appealing because of their extreme degrees of anisotropy, morphologically dependent plasmonic properties, and tailored optical properties from visible to near infrared regions [42-45]. In particular, AgNPrs possess much stronger SPR which can increase sensitivity and also their highly reactive sharp edges which are facilely etched by other molecules. For this reason, AgNPrs can serve as a chromogenic agent for the colorimetric detection. However, to date, AgNPrs have been seldomly explored for colorimetric sensors compared with AgNPs and AuNPs. With such attractive properties of the AgNPrs, this

work sought to fabricate a versatile and straightforward sensing platform based on this material.

Herein, a novel, simple, field-portable and rapid colorimetric PADs for Cl⁻ monitoring by utilizing AgNPrs as a remarkable colorimetric agent was proposed for the first time. Upon the addition of the Cl⁻ solution into AgNPrs, a visible color change of AgNPrs from dark-violet to red was rapidly observed. To facilitate the application of this sensor for on-site testing, a smartphone was also used to monitor the colorimetric responses in the detection platform, as shown in Figure 3.1.1. Furthermore, the proposed colorimetric sensor could be exploited to determine the Cl⁻ level in different kinds of water samples, and comparisons were in good agreement with the conventional spectroscopic method. The simple, disposable character and simplicity of the devices provides an interesting alternative to the most frequently used conventional methods.

**Figure 3.1.1** Photograph showing the setup of an in-house light control box with the smart-phone for Cl⁻ detection.

### 3.1.2 Experimental

#### 3.1.2.1 Reagents and apparatus

Silver nanoprisms (AgNPrs) with diameters of 35, 45 and 50 nm and silver nanoparticles (AgNPs) with a diameter of 10 nm containing starch as a stabilizer without a capping agent were obtained from the Sensor Research Unit, Department of Chemistry, Faculty of Science, Chulalongkorn University, Thailand. A standard Cl⁻ solution for Cl⁻ detection was prepared from sodium chloride (Carlo Erba, France). Ammonium acetate was purchased from Riedel-de Haen, Germany. Magnesium

sulfate was purchased from Sigma Aldrich, USA. Iron (II) sulfateheptahydrate, zinc nitrate tetrahydrate, boric acid and sodium hydrogen carbonate were purchased from Merck, Germany. Di-ammonium hydrogen orthophosphate was obtained from Univar, Australia. Copper sulphate was purchased from Fluka, Switzerland. All chemicals were used as received without any purification procedure. All reagents were prepared with milli-Q water from Millipore ($R \geq 18.2$ MΩ cm) throughout these experiments.

### 3.1.2.2 Instrumentation

UV-visible absorption spectra were recorded by a HEWLETT PACKARD 8453 UV-visible spectrometer (Agilent technologies, UK) using a conventional 1.0 cm quartz cell. Transmission electron microscopy (TEM) images were recorded by a H-7650 transmission electron microscope (Hitachi model, Japan). Surface morphologies were studied using a JSM-7610F field emission scanning electron microscope (FESEM) (JEOL ltd., Japan).

### 3.1.2.3 Preparation of the silver nanoprisms

The AgNPrs were synthesized according to a reporting procedure [44]. It should be noted that the AgNPrs employed in this reaction were stabilized with a starch solution (steric stabilization). Briefly, a $NaBH_4$ reducing agent was dissolved in the starch solution. Then, the $AgNO_3$ dissolved in starch solution was immediately injected into the reducing agent solution under vigorous stirring. The colorless solution became a dark brown colloid, indicating the formation of the small silver nanospheres (AgNPSs). The colloidal solution was then boiled, cooled down and aged for 12 hrs to eliminate the residual of $NaBH_4$. Upon dilution with milli-Q water,

the colloid turned bright yellow. Then, a 30% $H_2O_2$ functioned as an etchant toward Ag species and as reducing species toward $Ag^+$ was injected via a syringe pump. After the addition of the $H_2O_2$ solution, the colloid was further stirred for another 10 min to ensure a complete reaction.

### 3.1.2.4 Wax-patterned paper fabrication

Circular areas with a diameter of 0.7 cm were designed by Adobe illustrator CS4 software (Adobe Systems, Inc.). The wax printing method was used for the fabrication of PADs. The blue wax color with an RGB value of (98/147/254) was used to be complementary to the colorimetric reaction. The process to fabricate PADs consisted of two steps: (1) printing the wax pattern on the surface of filter paper (Whatman no.1) by a commercial wax printer (Xerox Color Qube 8570, Japan) and (2) melting the wax printed paper at 175ºC for 40 seconds on a hot plate. The printed wax can penetrate the paper and generate complete hydrophobic barrier and hydrophilic channels within the paper.

### 3.1.2.5 Analytical procedure and image processing

For colorimetric monitoring of $Cl^-$, 10 µL of the AgNPrs was firstly added onto the hydrophilic test zone on PADs. Next, 10 µL of either sample solution or $Cl^-$ standard solution was applied onto the test zone. The color change of AgNPrs was rapidly visualized after 3 minutes through the naked eye. After that, the test zone of PADs was captured with a smartphone (Iphone 6s, Apple Inc.) under an in-house light control box using the Yamera application. The JPEG format image was then imported to ImageJ software (National Institute of Health, USA) for measurement of the mean color intensity. The image color threshold was set to remove the blue background

color by adjusting the hue and brightness window specific range at (100/200) and (60/200), respectively. The color signal of each zone was measured as the mean color intensity and then imported into Numbers software (v 2.0.3, Apple Inc.) for analysis.

### 3.1.2.6 Preparation of water samples

The local tap water, drinking water and groundwater from the salt evaporation pond were collected and used in this study. Tap water and drinking water samples were analyzed without any additional sample treatment. The groundwater samples were diluted 20-fold with milli-Q water before use. Then all of the samples were analyzed for $Cl^-$ level by the spectrophotometric method and the proposed colorimetric sensor in succession.

### 3.1.3 Results and discussion
#### 3.1.3.1 Morphological characteristics of AgNPrs
##### 3.1.3.1.1 UV-Visible spectrophotometry

To monitor the size change of AgNPrs, UV-Vis absorption spectroscopy was first used. Figure 3.1.2 displays the surface plasmon resonance (SPR) absorption spectrum of the AgNPrs. Technically, as reported by Parnklang et al. [44], the AgNPrs possess two characteristic peaks attributed to the out-of-plane quadrupole plasmon resonance (OPQPR) and in-plane dipole plasmon resonance (IPDPR). Clearly, two characteristic peaks of AgNPrs (purple line) were observed at 338 and 543 nm, as shown in Figure 3.1.2. The signature peaks at 338 and 543 nm could be ascribed to the OPQPR and IPDPR of the AgNPrs, respectively. Interestingly, after the addition of the $Cl^-$ into the AgNPrs solution, a slight shift toward longer wavelength (red shift) of OPQPR from 338 nm to 350 nm was perceived. This change indicates the decrement

of the aspect ratio (bisector length/thickness) of the nanoprisms [44]. Besides, the substantial blue shift of IPDPR of AgNPrs from 543 nm to 455 nm together with gradual decreases in absorbance was also observed. This change in the in-plane plasmon band demonstrates the lateral reduction in the dimension of the AgNPrs (as evidence in the TEM images (Figure 3.1.3)), leading to a decline in the extinction coefficient of the particle. Thus, the absorbance is decreased. Additionally, an obvious color change of the AgNPrs solution from dark-violet to red could also be seen by the naked eye as shown in the inset of Figure 3.1.2. The color change and shift in SPR absorption band suggested that the shape of the AgNPrs was transformed by the concentration of Cl$^-$ added into solution.
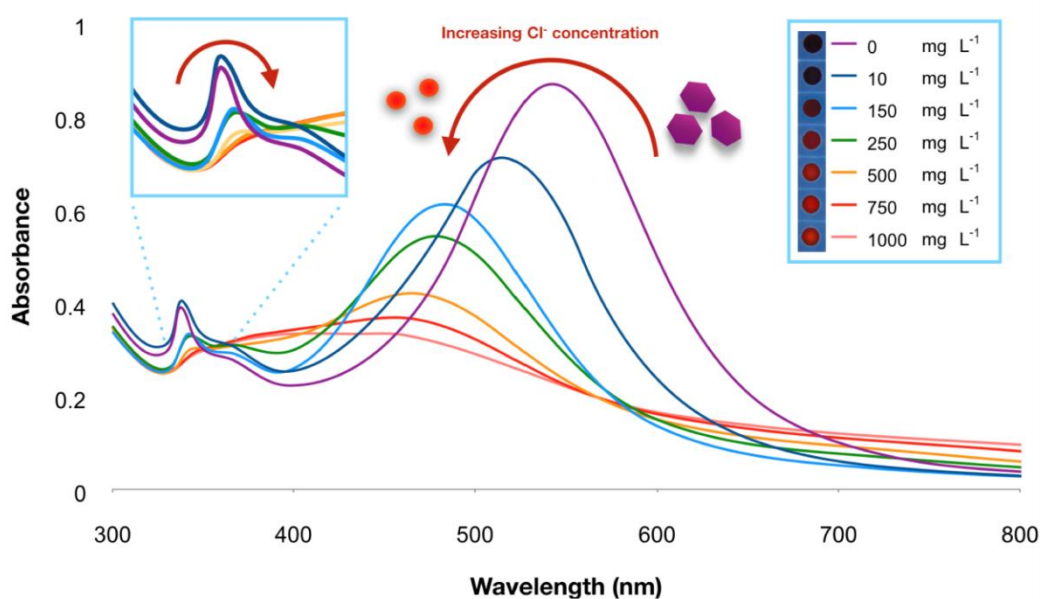


**Figure 3.1.2** The UV-vis absorption spectra and the photographs (inset) of the AgNPrs after the addition of Cl$^-$ at different concentrations ranging from 0 to 1000 mg L$^{-1}$ with the measurement time at 5 min.

### 3.1.3.1.2 Transmission electron microscopy (TEM) and scanning electron microscopy (SEM) with energy dispersive X-ray analysis (EDX)

In order to investigate the morphology of the AgNPrs, TEM and SEM/EDX analyses of AgNPrs were carried out in the presence and absence of $Cl^-$. The results from TEM images (Figure 3.1.3) indicate that the particle size of the AgNPrs decreased after the addition of $Cl^-$. Moreover, the morphological transformation from truncated triangle and hexagon to circular disk was clearly observed indicating the oxidative etching of AgNPrs upon the addition of $Cl^-$. This is because the AgNPrs possess high surface energy, particularly at the tip and edge portion where the silver atoms are easily etched by oxidation. Additionally, from SEM images, 50,000 x amplification was made to verify the structure of the AgNPrs on the paper substrate without (Figure 3.1.4A) and with (Figure 3.1.4B) the existence of $Cl^-$. This complementary result clearly justified that the AgNPrs were etched by $Cl^-$. In the absence of $Cl^-$, AgNPrs were extensively deposited on the cellulose paper. In the presence of $Cl^-$, however, the small amount with a reduction in average size of AgNPrs was evidently observed. Furthermore, a SEM/EDX analysis of AgNPrs was also performed on the surface of paper substrate as shown in Figure 3.1.4C and 3.1.4D. EDX spectrum shows the presence of silver (Ag) that correspond to the AgNPrs. Carbon (C) and oxygen (O) are also present, which can be attributed to the cellulose composition of the paper. Although a less intense peak of Ag in the EDX spectrum arose likely because of the penetration of the AgNPrs into the porous fiber of paper substrate, this data could confirm the elemental identification of the deposited AgNPrs on paper. The results from the TEM and SEM/EDX analyses are consistent with the SPR absorption spectra which can confirm the experimental observations discussed above.
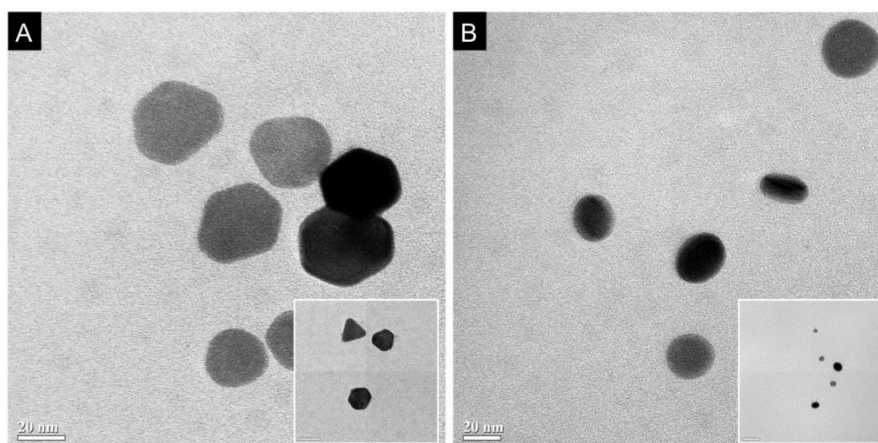
**Figure 3.1.3** TEM images of the AgNPrs at high and low magnification (inset) in the absence (A) and the presence (B) of 1000 mg L$^{-1}$ Cl$^-$.
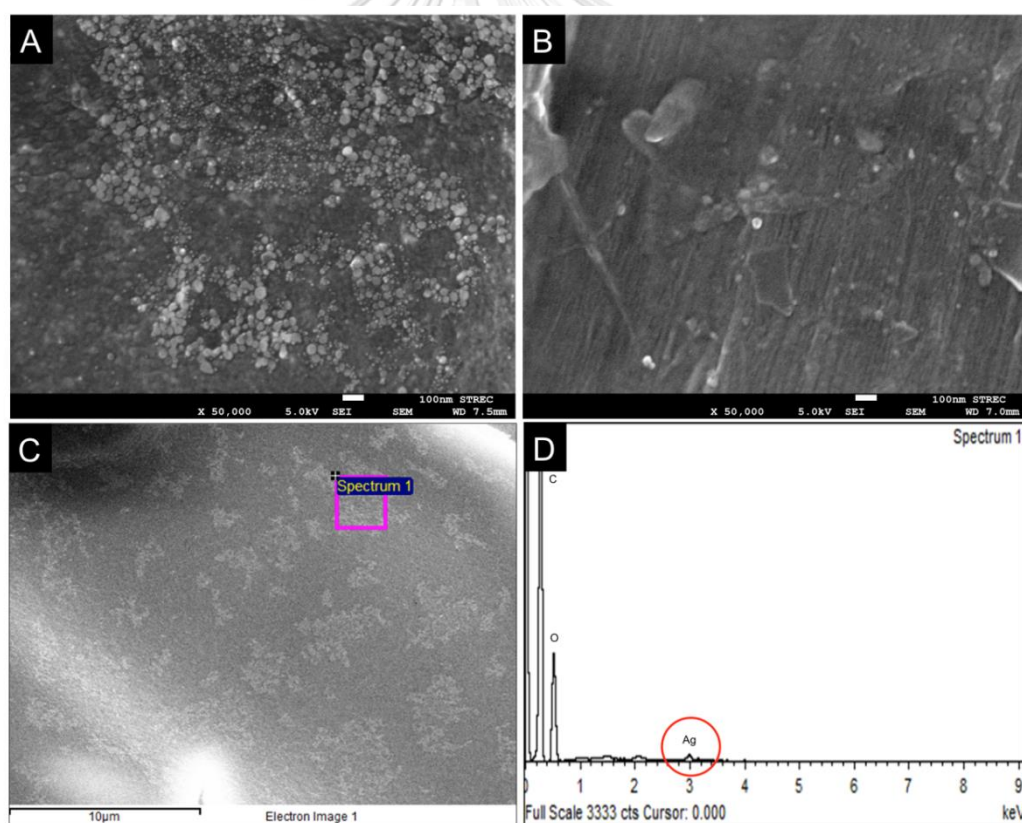


**Figure 3.1.4** SEM images of the AgNPrs on a paper-based sensor at 50,000 x magnification without (A) and with (B) the existence of 1000 mg L$^{-1}$ Cl$^-$; the photomicrograph (C) and the corresponding EDX spectra (D) of the AgNPrs.

### 3.1.3.2 Detection principle

Unlike other works, which generally used electrostatic stabilized silver nanoparticles that caused aggregation/anti-aggregation of the nanomaterials, herein, no charge on the surface of nanomaterials is involved in the size alteration mechanism of AgNPrs. According to the experimental result, it was expected that these phenomena could arise from the oxidation of AgNPrs with oxygen ($O_2$) in the presence of $Cl^-$, resulting in a reduction in particle size of the AgNPrs. In order to confirm the detection mechanism, various sodium salts were tested. As hypothesized, only $Cl^-$ from NaCl could cause obvious color change (Figure 3.1.5). Furthermore, a control experiment was also performed under nitrogen ($N_2$) atmosphere instead of air to avoid the presence of oxygen ($O_2$). It can be seen that there no color change is observed (Figure 3.1.6). Thus, it could be deduced that the oxygen ($O_2$) played a key role in the etching of the AgNPrs. In the absence of $Cl^-$, AgNPrs could not be oxidized by oxygen ($E^\circ O_2/OH^- = +0.401$ V) due to its relatively high standard reduction potential of $Ag^0$ ($E^\circ Ag^+/Ag^0 = +0.799$ V). However, the standard reduction potential of Ag in the presence of $Cl^-$ was decreased ($E^\circ AgCl/Ag^0 = +0.222$ V). Thus, AgNPrs could be oxidized, as shown in Eq. (1), and the proposed mechanism was illustrated in figure 3.1.7. Therefore, a rapid colorimetric assay for $Cl^-$ detection could be established using the AgNPrs as the colorimetric agent.

$$Ag^0 + Cl^- + O_2 + 2H_2O \rightarrow AgCl + 4OH^- \qquad (3.1)$$
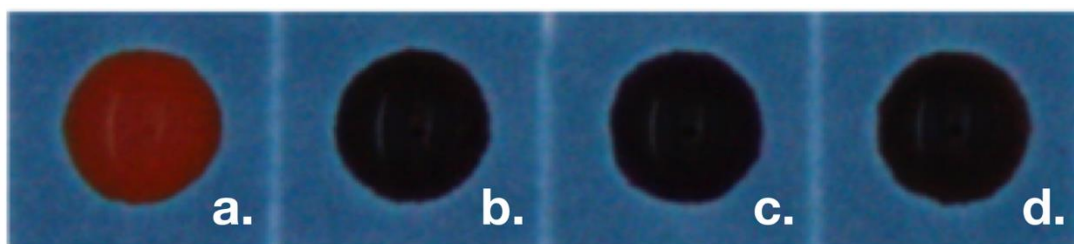
**Figure 3.1.5** The visual image of the AgNPrs on PADs after the addition of (a) NaCl, (b) $Na_2SO_4$, (c) $NaHCO_3$, and (d) $Na_3PO_4$ at concentration of 1000 mg $L^{-1}$ with the measurement time of 5 minute.
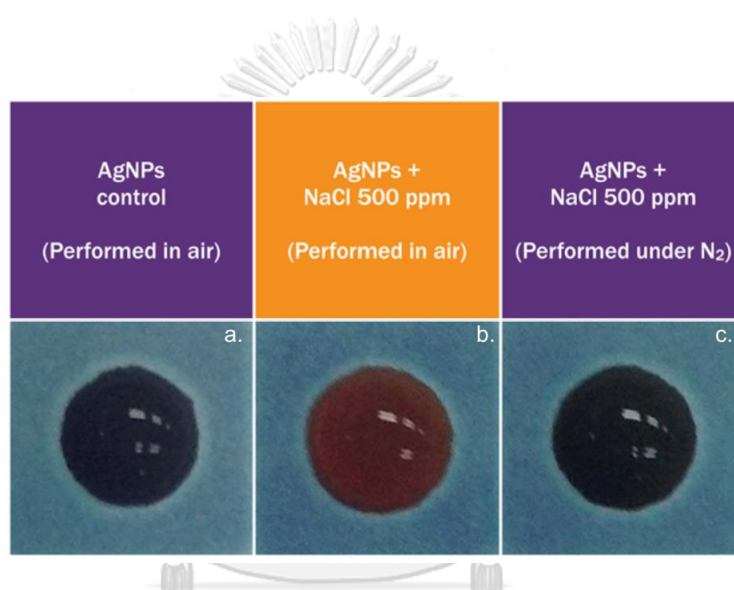


**Figure 3.1.6** The visual image of the AgNPrs; (a) in absence of $Cl^-$ under air atmosphere and (b) in the presence of 500 mg $L^{-1}$ $Cl^-$ under air atmosphere and (c) $N_2$ atmosphere, respectively.
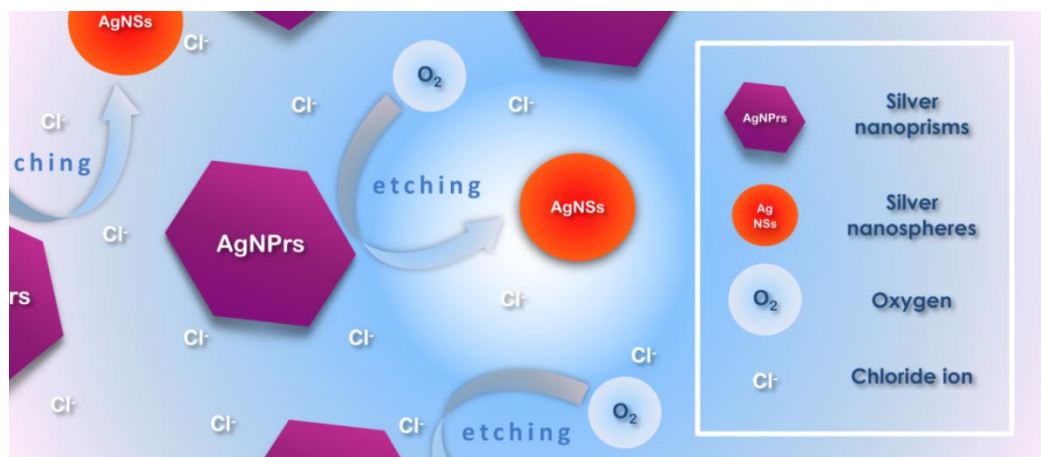
**Figure 3.1.7** Schematic representation of the proposed mechanism between AgNPrs and Cl$^-$ for Cl$^-$ measurement.

### 3.1.3.3 Optimization of the assay conditions

The performance of the colorimetric paper-based sensor is influenced by the various assay conditions including particle sizes and concentrations of the silver nanomaterial, and measurement time. These parameters were optimized in this study using 1000 mg L$^{-1}$ of Cl$^-$ to obtain the maximum response for Cl$^-$ analysis.

The different particle sizes of the AgNPrs and AgNPs were investigated for the efficiency of Cl$^-$ detection on paper-based sensor. Figure 3.1.8A exhibits the influence of the size of nanostructure on color change when adding Cl$^-$ into solution. The difference in the mean color intensity values before and after the addition of Cl$^-$ ($\Delta I$ = $I_{sample} - I_{blank}$) was considered for determining the optimal conditions. The results of color change obtained by the AgNPrs with a diameter of 35 nm (pink to yellow) and 45 nm (dark-violet to red) can be more clearly seen than the others. However, the AgNPrs with a diameter of 45 nm were selected for further evaluation because their mean color intensity difference ($\Delta I$) of the AgNPrs measured by ImageJ software exhibited the highest value which can be distinguished from the original color, leading to the highest sensitivity. Thus, the AgNPrs with a diameter of 45 nm was

used as the colorimetric agent for all experiments. For the effect of AgNPrs (45 nm) concentration, different levels in the range of 60-300 mg $L^{-1}$ were investigated as shown in Figure 3.1.8B. Even though the best $\Delta I$ was determined at 60 mg $L^{-1}$, this AgNPrs concentration resulted in a narrow linear dynamic range compared with 300 mg $L^{-1}$ AgNPrs. At low concentration of AgNPrs, the dark violet color of nanoprisms became brighter which led to a high color intensity value. Whereas, the darker color is observed at high concentrations of AgNPrs resulting in a less color intensity value. Therefore, signals to blank ratios obtained from darker color provide the higher sensitivity in detection. The working curve was also compared between 60 mg $L^{-1}$ and 300 mg $L^{-1}$ (data not shown). It was observed that the use of 60 mg $L^{-1}$ AgNPrs as a colorimetric agent exhibited a narrower linear dynamic range. This is primarily due to the saturation in response at relatively low concentrations where available silver atoms to react with excess $Cl^{-}$ is limited. Meanwhile, at a high AgNPrs concentration, a number of silver atoms can entirely react with the excessive amount of $Cl^{-}$. Hence, to extend the linear dynamic range, 300 mg $L^{-1}$ was chosen as the optimal concentration of the AgNPrs.

The detection time is also a key point, affecting colorimetric results. The relationship between mean intensity and measurement time ranging up to 20 minutes was studied as shown in Figure 3.1.8C. It can be seen that the mean color intensity gradually increased from 1 to 5 minutes, and remained steady at 5 minutes, demonstrating that the etching of the AgNPrs was completed within 5 minutes. Thus, the measurement time was chosen at 5 min for the following experiment.
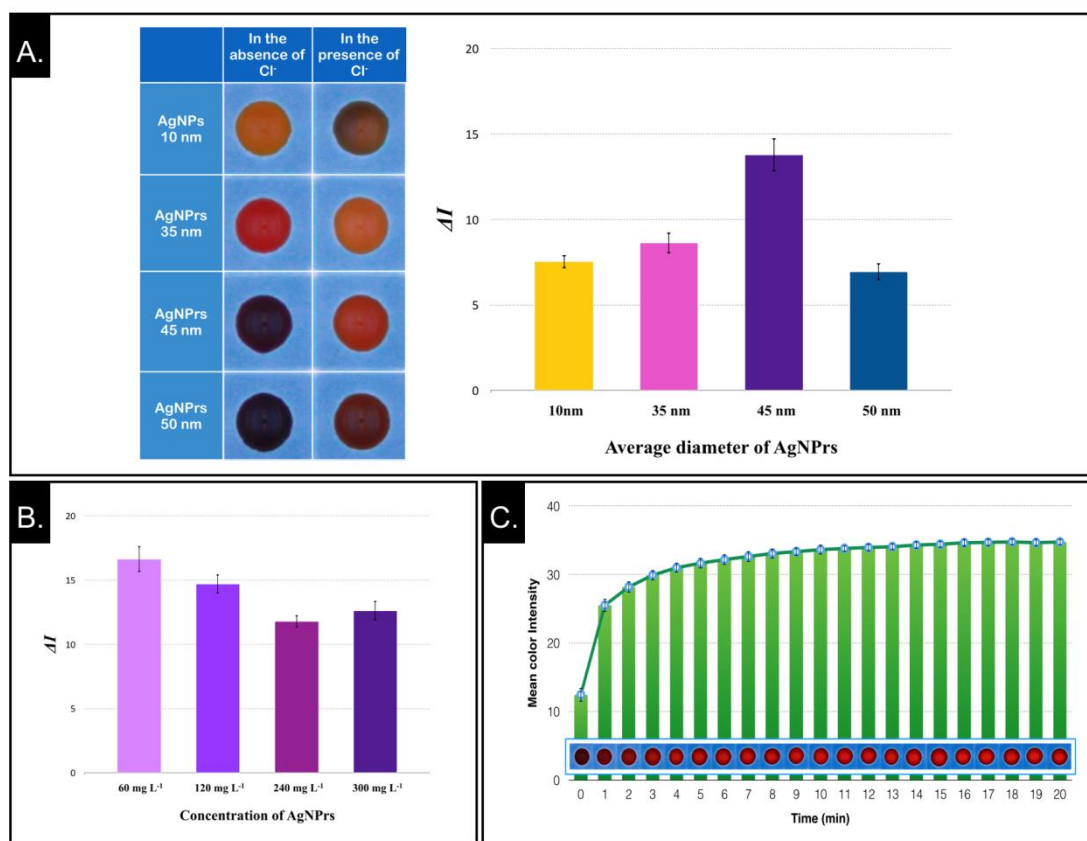
**Figure 3.1.8** Effect of the experimental conditions for Cl⁻ detection on paper-based sensor; (A) photograph of the different particle size of AgNPs and the corresponding mean color intensity difference ($\Delta I$) between before and after addition of Cl⁻, and (B) photograph of an AgNPrs varied in time and a plot between mean color intensity and measurement time ranging up to 20 min in the presence of 10 μL of 1000 mg L⁻¹ Cl⁻.

### 3.1.3.4 Analytical performance of the AgNPrs-based colorimetric sensor

In order to measure Cl⁻ using the AgNPrs as the colorimetric agent, the performance of the proposed method was also investigated. With the addition of the Cl⁻, the mean color intensity of the AgNPrs increased gradually, corresponding to the color of the mixture solution obviously changed from dark-violet to red (Figure 3.1.9A). Under optimal conditions, the mean color intensity measured from ImageJ

software is related linearly to the logarithmic concentration of the Cl$^-$ (log Cl$^-$ concentration) in the range of 10 to 1000 mg L$^{-1}$ (R$^2$ = 0.996) with a limit of detection (LOD) and limit of quantitation (LOQ) from a calculation of 1.3 and 4.3 mg L$^{-1}$, respectively (Figure 3.1.9B). This indicates that the proposed sensor can be used for the quantitative analysis of Cl$^-$.
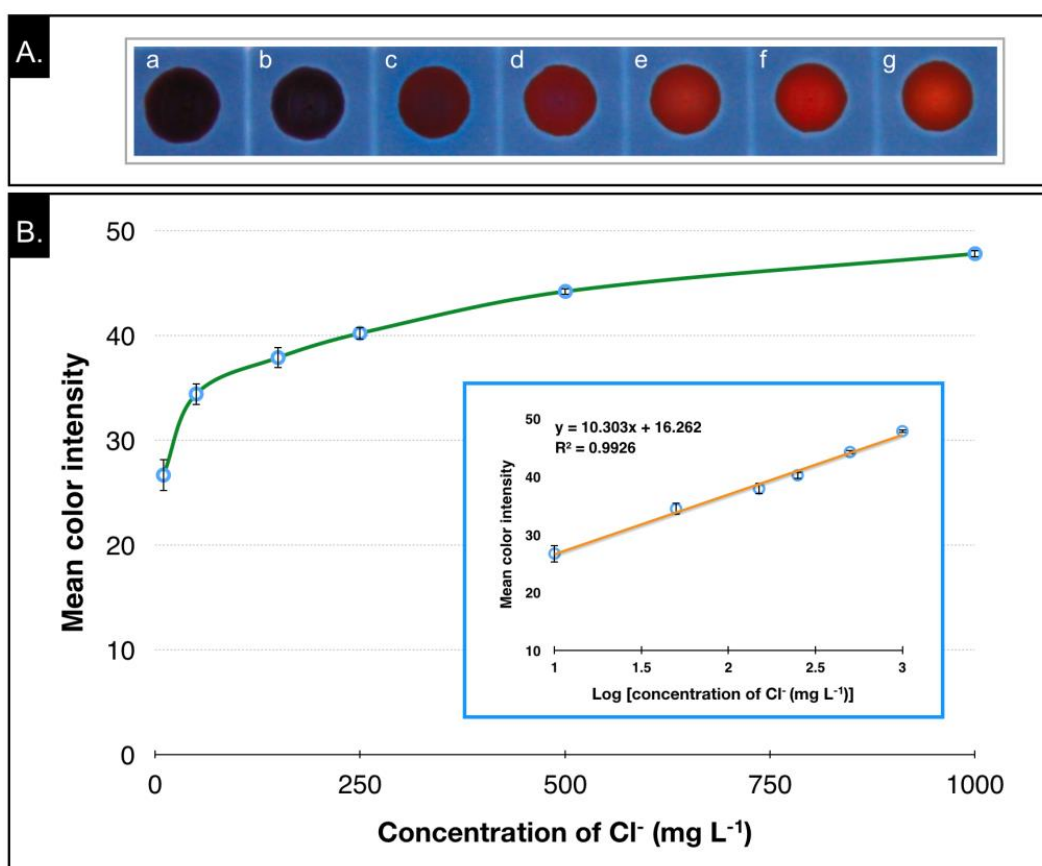


**Figure 3.1.9** (A) A visual image of the paper-based sensor for the detection of Cl$^-$ at concentrations of (a) 0, (b) 10, (c) 150, (d) 250, (e) 500, (f) 750 and (g) 1000 mg L$^{-1}$ with 10 µL of the AgNPrs. (B) the plot of the mean color intensity of the AgNPrs determined by digital image analysis using ImageJ software versus Cl$^-$ concentration (0-1000 mg L$^{-1}$). Inset: the calibration graph for Cl$^-$ measurement plotted as the mean color intensity and logarithmic Cl$^-$ concentration.

Furthermore, to evaluate the reproducibility of the proposed sensors, relative standard deviation (%RSD) was examined using three concentrations of $Cl^-$ (10, 250 and 750 mg $L^{-1}$). %RSD for triplicate measurements of each concentration were found to be less than 7%, suggesting that this sensor is precise enough for detection of $Cl^-$ in real sample with excellent sensitivity and reproducibility.

### 3.1.3.5 Selectivity and interference studies for the $Cl^-$ detection

To further assess the selectivity of the AgNPrs, several environmental relevant species including $NH_4^+$, $Mn^{2+}$, $Fe^{2+}$, $Cu^{2+}$, $Zn^{2+}$, $H_3BO_3$, $SO_4^{2-}$, $CO_3^-$ and $PO_4^{3-}$ was first examined individually at 500 mg $L^{-1}$. This concentration is typically much higher than that found amount in water samples. The results demonstrated that no apparent color changes ofAgNPrs are observed from any tested interfering species. Additionally, the mean color intensity difference ($\Delta I = I_{tested\ species} - I_{blank}$) between the tested species and control justified that only $Cl^-$ was found to significantly increase the mean color intensity of the AgNPrs (Figure 3.1.10A). This could be explained by the high standard reduction potential of AgNPrs ($E° Ag^+/Ag^0 = +0.799$ V) in which none of the tested interfering species could oxidize. However, it has been reported that $Br^-$, $I^-$ can also promote the morphological transformation of triangular silvernanoprisms [46, 47]. Therefore, other halide anions ($F^-$, $Br^-$ and $I^-$) were further tested in this approach (figure 3.1.11). It is obvious that some of the halide anions also behave like $Cl^-$, especially $Br^-$ which shown stronger reducing ability than $Cl^-$ (figure 3.1.11 (upper)). Nevertheless, the existence of these halide anions in natural water was extremely low compared to $Cl^-$. For instances, concentration of $Br^-$ in water typically ranges from trace amount to about 0.5 mg $L^{-1}$ [48]. In ground water, the average concentration of $I^-$ is approximately 1 μg $L^{-1}$ [49]. The content of natural $F^-$ in water ranges from 0.01 up to 7.2 mg $L^{-1}$ [50]. Therefore, additional tested at

possible found concentration was also performed (Figure 3.1.11 (lower)). The result indicates no significant interfered from these tested ions. Hence, it can be said that this proposed sensor can be applied to use in a real sample application with good selectivity.

To confirm the results, a mixture of potential interfering at a concentration of 500 mg L$^{-1}$ in the presence of 500 mg L$^{-1}$ Cl$^{-}$ were tested by the proposed sensors. The results obtained from the mixture solution and solely of Cl$^{-}$ were not significantly different (Figure 3.1.10B). Thus, it can be taken for granted that this sensor offers a high selectivity toward Cl$^{-}$ detection.
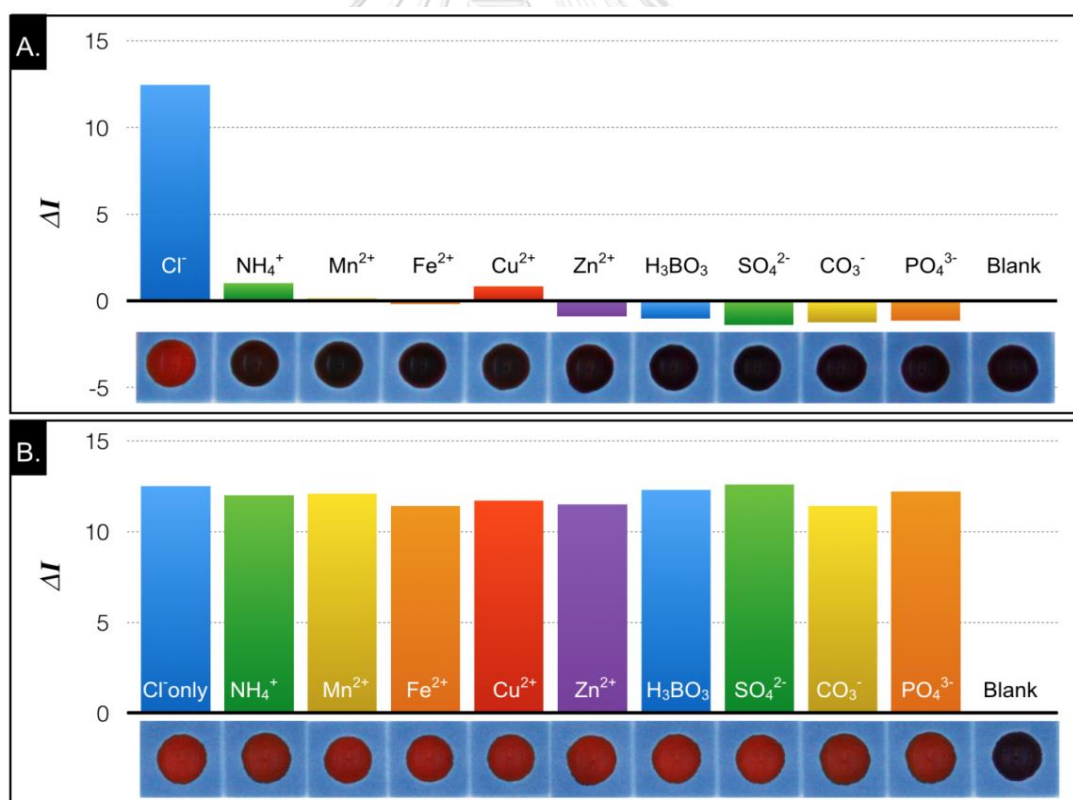


**Figure 3.1.10** The photographic image results of the colorimetric detection on PADs and the mean color intensity difference of the AgNPrs ($\Delta I = I_{tested\ species} - I_{blank}$) on the paper-based sensor; (A) after the addition of the indicated interfering

substances at concentration of 500 mg L$^{-1}$ and (B) after the addition of the mixture solution comprising Cl$^-$ (500 mg L$^{-1}$) and indicated interfering substances (500 mg L$^{-1}$).
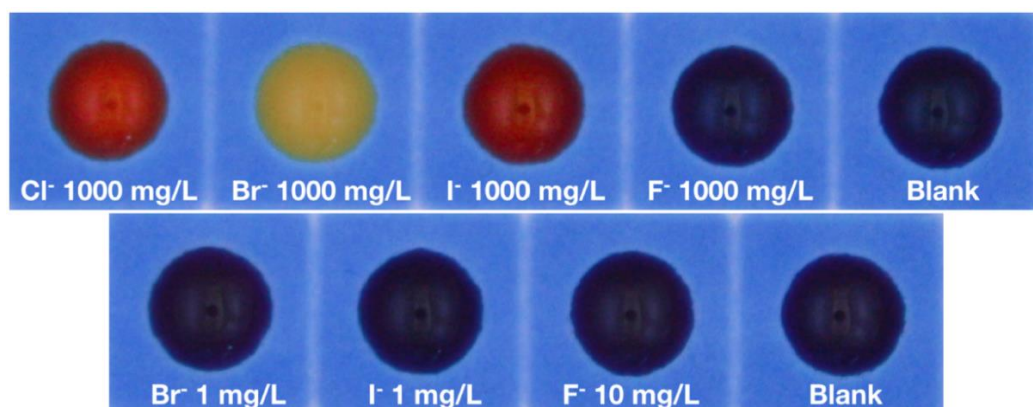


**Figure 3.1.11** Interference study for halide anions at 1000 mg/L (upper) and possible found concentration in nature (lower).

### 3.1.3.6 Chloride ion determination in water samples

To validate the applicability of this sensor, several local water samples including tap water, drinking water, and groundwater from salt evaporation ponds were determined by both the proposed method and the standard spectrophotometric method [28]. The comparison of the results obtained from the two techniques is shown in Table 3.1.1. It was found that the results from the proposed method were in good agreement with those obtained from the UV-Vis spectrophotometry (paired $t$-test at the 95% confidence level gave $t_{calculated}$ (1.861) below $t_{critical}$ at $t$ = 2.306). These results indicate that the colorimetric sensor developed here is potentially applicable to be used in the reliable determination of the Cl$^-$ in real natural water samples.

**Table 3.1.1** Summarized results of the determination of $Cl^-$ in water samples by the proposed method compared with the standard method [23].

| Sample | | $Cl^-$ concentration (mg $L^{-1}$) | |
|---|---|---|---|
| | | Proposed method | UV-Vis |
| | | Found amount (mg $L^{-1}$) | Found amount (mg $L^{-1}$) |
| Drinking water | Sample 1 | 16.90 ± 0.52 | 18.88 ± 0.19 |
| | Sample 2 | 24.41 ± 1.1 | 20.36 ± 0.01 |
| | Sample 3 | 40.21 ± 0.92 | 38.75 ± 0.08 |
| Tap water | Sample 1 | 27.79 ± 1.2 | 29.04 ± 0.20 |
| | Sample 2 | 27.65 ± 1.2 | 30.45 ± 0.15 |
| | Sample 3 | 29.82 ± 1.4 | 29.41 ± 0.26 |
| Ground water | Sample 1 | 4345 ± 26 | 4280 ± 0.84 |
| | Sample 2 | 8468 ± 29 | 8429 ± 1.9 |
| | Sample 3 | 3018 ± 37 | 2930 ± 1.1 |

### 3.1.4 Conclusions

By taking advantage of the unique optical properties of the AgNPrs, a new AgNPrs-based colorimetric approach for the determination of $Cl^-$ was successfully developed. Unlike the usual plasmonic sensors, which principally depend on the aggregation/anti-aggregation of the nanoparticles, this assay is based on the oxidative etching of the AgNPrs with $O_2$ / $Cl^-$. No surface modification is required. The shape and size of the nanoprisms are altered which can be visibly monitored through a color change from dark-violet to red without the need for a sophisticated experimental procedure or apparatus. Under optimal conditions, this colorimetric sensor exhibited good selectivity towards the $Cl^-$ against other environmental relevant species. Furthermore, the proposed method has successfully been applied to determine the $Cl^-$ levels in water samples using a smartphone with good agreement to those obtained by the standard method. Considering the versatility and simplicity provided by the proposal, this colorimetric sensor is promising for on-site determining and screening of $Cl^-$ levels in an environmental area.

**Part II**

## 3.2 Screen-Printed Electroluminescent Lamp Modified with Graphene Oxide as A Sensing Device

<u>Abdulhadee Yakoh</u>[a], Ruslan Álvarez-Diduk[b], Orawon Chailapakul[a,c]*, Arben Merkoçi[b,d]*

[a] Electrochemistry and Optical Spectroscopy Center of Excellence (EOSCE), Department of Chemistry, Faculty of Science, Chulalongkorn University, 254 Phayathai Road, Patumwan, Bangkok 10330, Thailand

[b] Nanobioelectronics and Biosensor Group, Catalan Institute of Nanoscience and Nanotechnology (ICN2), CSIC. The Barcelona Institute of Science and Technology, Campus UAB, Bellaterra, 08193, Barcelona, Spain

[c] Center for Petroleum, Petrochemicals and Advanced Materials, Chulalongkorn University, 254 Phayathai Road, Pathumwan, Bangkok 10330, Thailand

[d] Catalan Institute of Nanoscience and Nanotechnology (ICN2), CSIC and BIST, Campus UAB, Bellaterra, 08193 Barcelona, Spain

* Corresponding author

**Abstract**

A screen-printed electroluminescent display with different sensing capabilities is presented. The sensing principle is based on the direct relationship between the light intensity of the lamp and the conductivity of the external layers. The proposed device is able to detect the ionic concentration of any conductive species. Using both top and bottom emission architectures, for the first time, a humidity sensor based on electroluminescent display functionalized by graphene oxide nanocomposite is introduced. In this regard, just by coupling the display to a smartphone camera sensor, its potential was expanded for automatically monitoring human respiration in real time. Besides, the research includes a responsive display in which the light is spatially turned on in response to pencil drawing or any other conductive media. The above-mentioned features together with the easiness of manufacturing and cost-effectiveness of this electroluminescent display can open up great opportunities to exploit it in sensing applications and point of care diagnosis.

**Keywords:** Electroluminescent lamp, Graphene, Sensor, Screen-printing, Breath control, Smartphone-based sensing

### 3.2.1 Introduction

The growing and continuous demand for flexible optoelectronics [51-58] together with the evolution of wearable/portable electronics accessories have made possible that devices with good mechanical manipulation as folding, bending or rolling open up new opportunities for diverse applications [59-67]. In this perspective, alternating current electroluminescent (ACEL) displays are very promising due to their intrinsic ability of uniform light emission, low heat generation, flexible architecture and low power consumption [68-71]. Also, this type of devices can be easily fabricated by inexpensive screen-printing methods. So far, ACEL has been extensively used in commercial applications such as black lighting, decorative lighting, panel display or even large-scale billboard [4, 69, 72, 73]. Nevertheless, the expansion of ACEL display technology toward the sensing field is still rather limited and have been barely exploited [74, 75] representing, therefore, a big challenge for the scientific community.

Usually, to build a conventional ACEL display, transparent conductive materials on a transparent substrate are strictly required as a rear electrode in which the emitted light goes through the substrate located at the bottom [70, 76-78]. The transparent electrode produced from indium tin oxide (ITO) is typically used for this purpose. Alternatively, top-emission structure (TES) has been explored [69]. In TES architecture, the light from the phosphor layer is emitted directly through a top transparent conductive material, while the substrate is at the bottom (see Figure 3.2.1a). In contrast to bottom-emission structure (BES), this reversed architecture usually yields a higher brightness (under the same applied voltage) due to the shorter light path [69]. Besides, various substrates (e.g. paper, plastic or textile) can be chosen since there is no requisite for the substrate to be transparent [79, 80]. By taking advantage of the different configurations, we envisioned that an ACEL display

would be useful to create a versatile sensing platform. The light emission of an ACEL display mainly relies on the conductivities of the top conductive layer [81]. Hence, the change in conductance in the top layer of the ACEL display coming from an exposure of ions/charge carriers could alter the intensity of the emitted light. The direct relationship between the luminance and the conductivity could lead to sensing of a variety of conductive species, through the electroluminescence monitoring.

In this study, a powerful sensor based on ACEL display architecture lacking in the top electrode was engineered. This sensor is capable to detect and directly visualize the target analyte. To demonstrate its sensing ability, the ionic concentration of various water samples was monitored as proof of concept. In addition, this research took advantages of graphene oxide (GO) and its interesting properties in devices applications [82-84]. Using both TES and BES architectures, for the first time, a humidity sensor based on ACEL display functionalized by GO nanocomposite is introduced. Furthermore, this research demonstrated the high-performance of the developed sensor as point-of-care (POC) device to monitor human breath which may be interesting for further applications.

### 3.2.2 Experimental

#### 3.2.2.1 Reagents and apparatus

All commercial reagents were of analytical grade and handled according to the material safety data sheets suggested by the suppliers. A flexible silver paste (C2131014D3), dielectric ink (D2070209P6), phosphor paste (C2150213D5), and clear conductive ink (C2100629D1) were purchased from Gwent group/SunChemical (Pontypool, UK). A water-based dispersion of single layer GO sheets (5 mg mL$^{-1}$) was purchased from Angstron Materials (OH, USA). 5% of Nafion 117 solution, NaCl, K$_2$CO$_3$,

and KNO$_3$ were purchased from Sigma-Aldrich (Madrid, Spain). CH$_3$CO$_2$K and KCl were purchased from Panreac (Barcelona, Spain). All aqueous solutions were freshly prepared in ultrapure water produced using a Milli-Q system (>18.2 M$\Omega$ cm$^{-1}$) purchased from Millipore. SEM was performed through a Magellan 400L SEM High-Resolution SEM (FEI, Hillsboro, OR, USA). Cross-sectional SEM and EDX analysis were investigated by Quanta 650F Environmental SEM (FEI, Hillsboro, OR, USA). X-ray photoelectron spectroscopy (XPS) measurement was performed using a Phoibos 150 analyser (SPECS GmbH, Berlin, Germany). The thickness of the GO nanocomposite film was characterized by profilometer (Alpha Step D-500 Stylus Profiler, KLA-Tencor). A semi-automatic screen-printing machine DEK 248 (DEK International, Switzerland) was used for the screen-printing process. A wax printing was patterned with a Xerox ColorQube 8580 (Connecticut, USA) wax printer.

### 3.2.2.2 Fabrication of ACEL display

A polyethylene terephthalate (PET) film was used as the substrate; unless stated otherwise. Firstly, a flexible silver paste was printed directly onto PET substrate as the rear electrode and front bus-bar. Then, two layers of dielectric ink, a single layer of phosphor and clear conductor were sequentially printed onto the printed electrode. After each screen-printing layer, the screen-printed film was cured at 130$^\circ$C in a box oven for 10 minutes. For the use of ACEL in sensing applications, the prepared film was used without a clear conductor screen-printing. A wax printing method was used to define circular sensing spots (diameter of 8 mm). The device was completed by drawing a straight line to connect the bus-bar and sensing area with a clear conductor. An AC voltage was powered by an EL inverter build in battery model UTF-EB900-4E (for DC 9.0V input).

### 3.2.2.3 Fabrication of GO/Nafion based humidity sensor

A 4-rectangular pattern was screen printed through a polyester screen directly on top of the ACEL display using flexible silver paste. To prepare the composite, 2.5 mg mL$^{-1}$ GO solution (average lateral (x,y) and through-plane (z) dimension range of ≈ 500 nm and 1–1.2 nm, respectively, and C/O ratio about one unit (supplier's data)) was mixed with Nafion and sonicated for 1 hr. The prepared composite was carefully drop-casted onto an ACEL device and allowed to dry in the oven at 60°C for 5 minutes.

### 3.2.2.4 Humidity measurement

The humidity measurement was conducted in a custom-made chamber consisting of an adaptable closed chamber, light sensor, and mouthpiece. To achieve a certain level of humidity, RH was controlled by a series of saturated salt solution ranging low to high humidity level ($CH_3CO_2K$, $K_2CO_3$, NaCl, KCl, $KNO_3$) at room temperature. Each humidity level is kept constant for 30 min to obtain steady RH. The solution chamber was removed from the setup when a human breath is monitored. The breath was then blown directly to an ACEL sensor through a mouthpiece while the light emission is recorded.

### 3.2.3 Results and discussion

#### 3.2.3.1 Device architectures and working concept

An ACEL lamp was fabricated using a screen-printing technique. The overall schematic of a lamp structure (5 x 5 cm) is shown in Figure 3.2.1a. For full fabrication of ACEL lamp with TES configuration, the process began with coating a layer of silver

paste ink onto the substrate as the rear electrode, followed by a sequential coating of the dielectric layer. The phosphor was then coated on top of the dielectric layer. Finally, another layer of clear conductive ink was coated as the top electrode. As was mentioned above, in TES structure, the range of substrates is not limited to a transparent substrate; opaque flexible substrates varying from papers to commercial fabric can be used. As illustrated in Figure 3.2.2, the screen-printed electroluminescent lamp was fully achieved with the subsequent white light emission on different substrates (paper and plastic). Such a wide range of substrate selection may tune the resulting electroluminescence as well as the elasticity of the device platform.
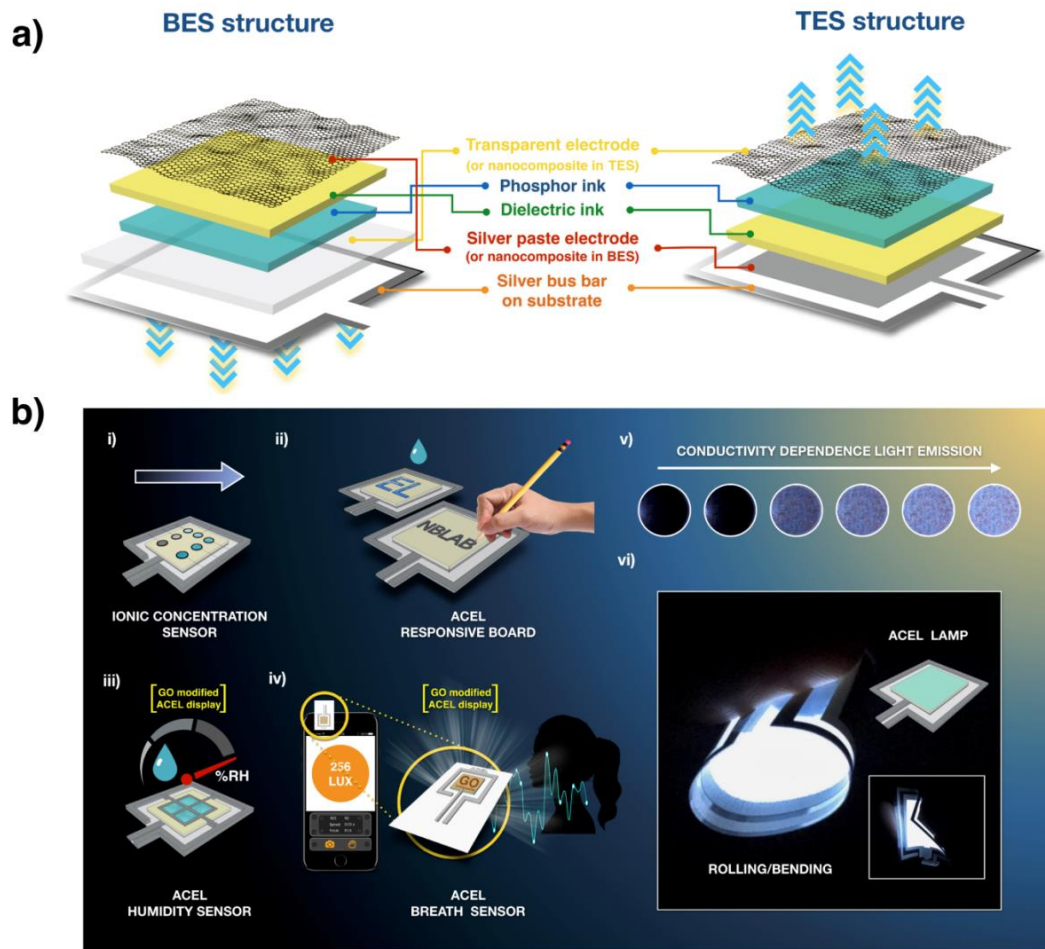
**Figure 3.2.1** (a) Schematic image of alternating-current electroluminescent (ACEL) display with BES and TES architectures. (b) Schematic illustration of the ACEL display working concept to sense (i) ionic concentration, (ii) writable conductance (responsive display), (iii) relative humidity level, and (iv) human breathing. (v) Photographs of the ACEL display on exposure of NaCl solution having different ionic concentrations/conductivities. (vi) Photographs of the ACEL display under bending/rolling conditions.
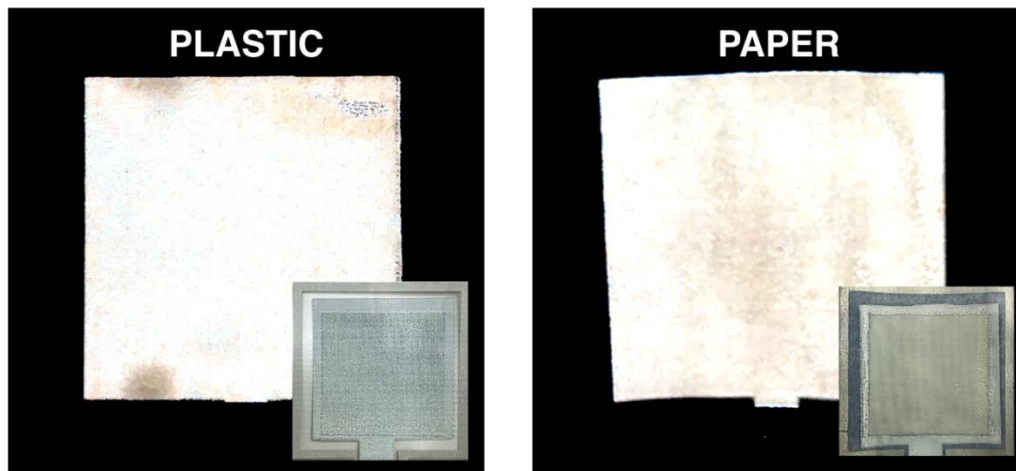
**Figure 3.2.2** Photographs of ACEL display printed on plastic (left) and normal white paper (right).

Other than being just a simple light panel, this ACEL display offers promising applications. As proof of concept, various sensing platforms based on flexible ACEL display are developed and proposed (Figure 3.2.1b). Using the dependence between light emission and conductivity of ACEL display as a primary tool, a variety of sensing approaches were designed and applied. For instance, the sense of (i) ionic concentration/conductance allowing water sample analysis, (ii) writable conductance (responsive board), (iii) relative humidity level, and (iv) human breathing using a smartphone will be demonstrated in this work.

### 3.2.3.2 Material characterizations and bending measurement

Fabrication of a multilayered ACEL display with TES configuration was further corroborated by scanning electron microscopy (SEM) cross-sectional image. As depicted in Figure 3.2.3a, the thickness of the silver paste electrode, dielectric layer,

and phosphor layer are about 18 μm, 89 μm and 71 μm, respectively. Energy dispersive X-ray (SEM/EDX) analysis in line-scan mode was also performed to analyze the elemental constituent of each layer (Figure 3.2.4). A major component of phosphor layer was substantiated to be ZnS particles, while the subsequence layer of dielectric is made of $BaTiO_3$ particles. The individual layer surface morphology was also characterized by SEM (Figure 3.2.5). Illustrating in figure 3.2.5a is an irregular shape of silver particles, which is extensively deposited over the whole substrate surface. As displayed in figure 3.2.5b, the dielectric layer exhibited a very rough surface, consisting of dense $BaTIO_3$ particles. In addition, in Figure 3.2.5c, together with the cross-sectional image, the light emitting phosphor layer appeared as a smoother surface compared to the underlying dielectric layer. The large grain phosphor particles distributed evenly over the surface.
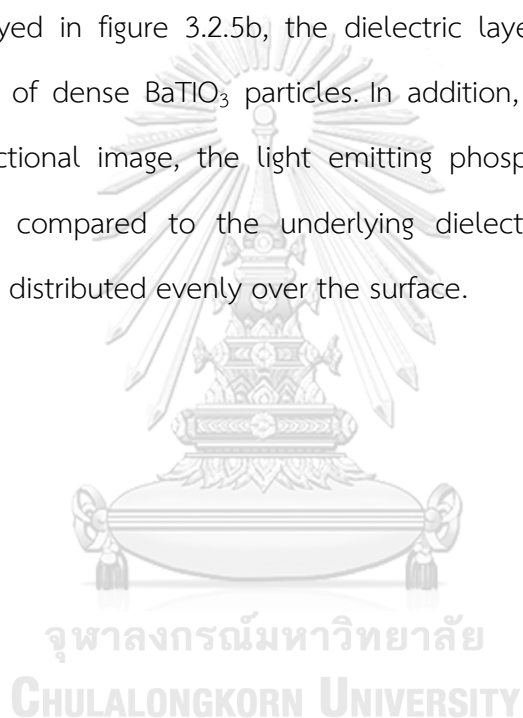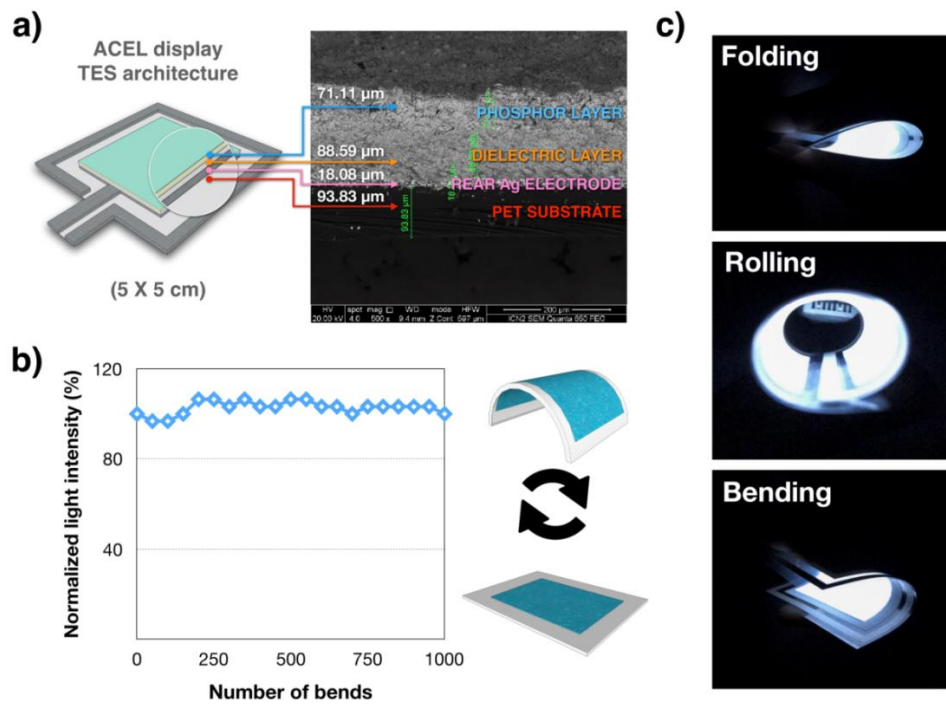
**Figure 3.2.3** (a) Schematic representation and scanning electron microscopy (SEM) cross-sectional image of an ACEL display structure. (b) Normalized light intensity as a function of the number of bends (bending measurement procedure is shown). (c) Images of ACEL display (TES) with clear conductive ink fabricated on PET substrate under different mechanical deformation conditions.
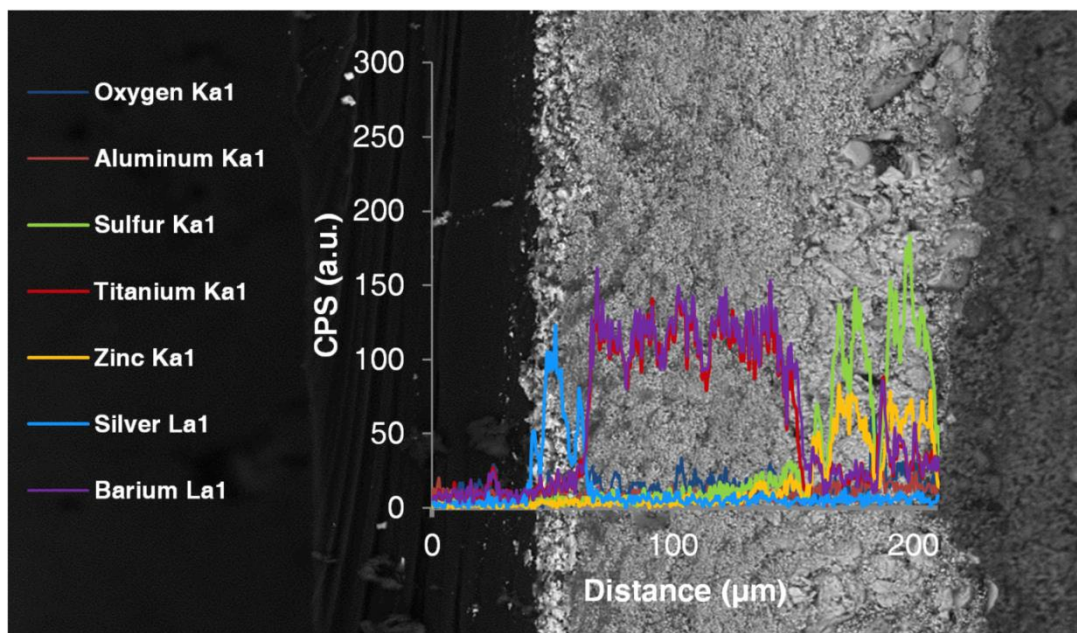
**Figure 3.2.4** SEM micrograph of cross-sectional ACEL display with SEM/EDX analysis in line-scan mode.
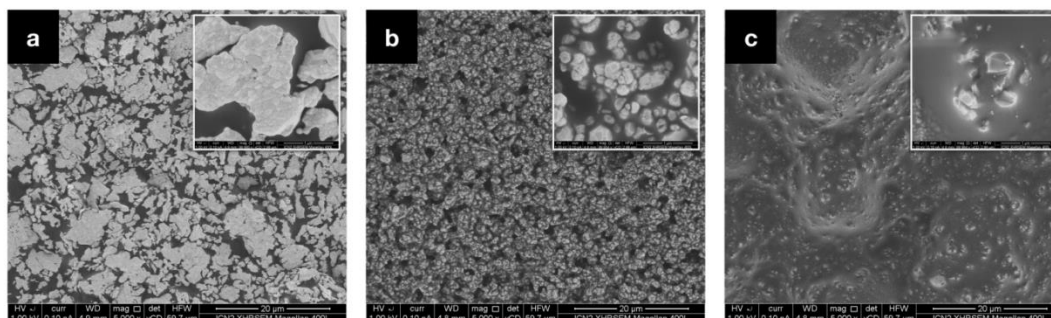


**Figure 3.2.5** SEM image characterization of each layer of ACEL display: a) Flexible silver paste as rear electrode and enlarge view (inset) on PET substrate; b) Dielectric layer and inset showing the image of $BaTiO_3$ particles; c) Phosphor layer and inset showing image of phosphor particles

To investigate the flexible and bendable ability of the electroluminescent display, the performance of the lamp in the presence of clear conductive ink electrode under bending condition was examined. The result from figure 3.2.3b shows that the emitted light intensity negligibly changed even after 1000 cycles of bending. The display could also be bent 180° or rolled meanwhile maintaining the functionality (figure 3.2.3c). This demonstrates that the ACEL display held an excellent flexibility and durability to mechanical deformation.

### 3.2.3.3 Light emission performance of the ionic concentration sensor and responsive ACEL board

Using the aforementioned TES ACEL lamp, a straightforward sensing platform based on electroluminescence was then sought to fabricate. In fact, the light emitted on an ACEL display is strongly affected by the conductivity of the materials over the phosphor layer. Hence, different conductivities would yield different electroluminescent intensities. To further investigate the relationship between conductivity and light emission, a solution of NaCl was carefully introduced on top of the phosphor layer of the ACEL display lacking in the top electrode. When the liquid solution spread over two electrodes that have the opposing phase of AC voltage (silver bus bar and underlying rear electrode), the light emission appears instantly (Figure 3.2.6). This phenomenon occurs because ions in the electrolyte solution can interconnect the electronic circuit, and then turns the light on. The light intensity as a function of solution conductivity was further studied. Various NaCl solutions having different ionic conductivities (MilliQ water $\approx$ 3.32 $\mu$S cm$^{-1}$; 1 mg L$^{-1}$ $\approx$ 4.72 $\mu$S cm$^{-1}$; 5 mg L$^{-1}$ $\approx$ 14.08 $\mu$S cm$^{-1}$; 10 mg L$^{-1}$ $\approx$ 24.0 $\mu$S cm$^{-1}$; 100 mg L$^{-1}$ $\approx$ 180.1 $\mu$S cm$^{-1}$; 1000 mg L$^{-1}$ $\approx$ 1789 $\mu$S cm$^{-1}$) were tested. It should be noticed that printed-wax circles were used to define the sensing area onto the display in order to reduce large

volume solution usage (Figure 3.2.7). Under the same applied voltage, the light intensity was proportional to the ionic concentration/conductivity of a saline solution (Figure 3.2.8a). This result indicates that the device can determine the ionic concentration/conductivity. Furthermore, using the light sensor embedded in a smartphone camera as an optical detection tool, the linear calibration between light intensity (lux) and logarithmic concentration of NaCl was established in the range of 1-100 mg $L^{-1}$ (Figure 3.2.8b-c). It allows the quantitative evaluation of the ionic concentration. As proof of concept, water samples including milli-Q, distilled, and tap water were inquired with the ACEL display. As expected, it was evident in the Figure 3.2.8d that tap and distilled water emit higher luminescence than milli-Q water owing to their larger dissolved ions concentration in the water.

As a result of this unique conductance-based light emission property, any conductive material could be visualized on this display. Thus, a simple responsive ACEL display with TES architecture has been exemplified in this work. Tap water or office pencil, for example, can be used as a conductive stylus to draw onto the surface of an ACEL panel. As indicated in Figure 3.2.8e, the light turns on instantaneously when this conductive media touched the electrode bar. Even though the electrode bar is inevitable, minimizing the bar size can make it invisible.
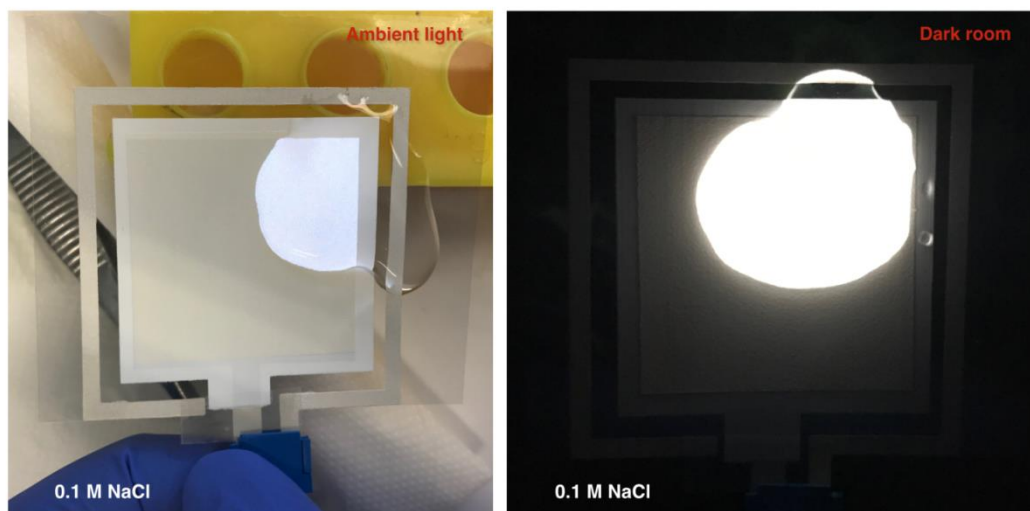
**Figure 3.2.6** Photographs of an ACEL display poured with 0.1M NaCl onto the surface under ambient room and dark room.
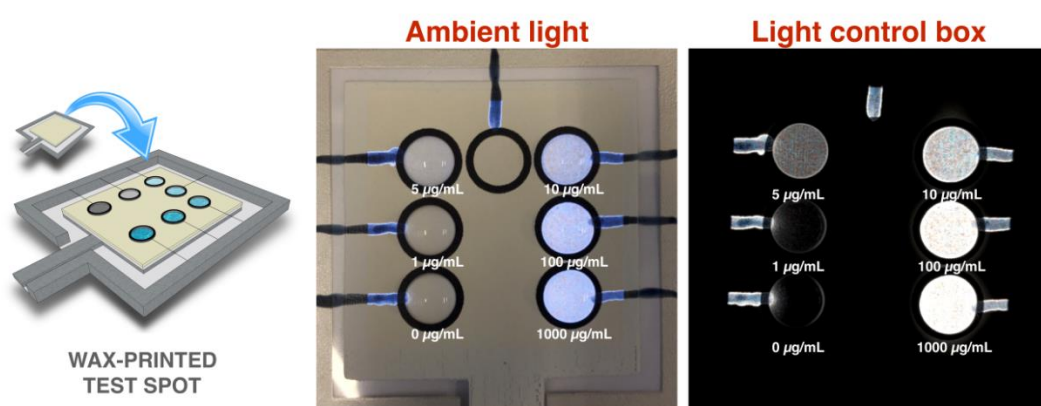


**Figure 3.2.7** Schematic illustration of a wax-printed ACEL device and Photographs of an ACEL display testing with different concentrations of NaCl ranging from 0-1000 mg L$^{-1}$ under ambient light (left) and light control box (right).
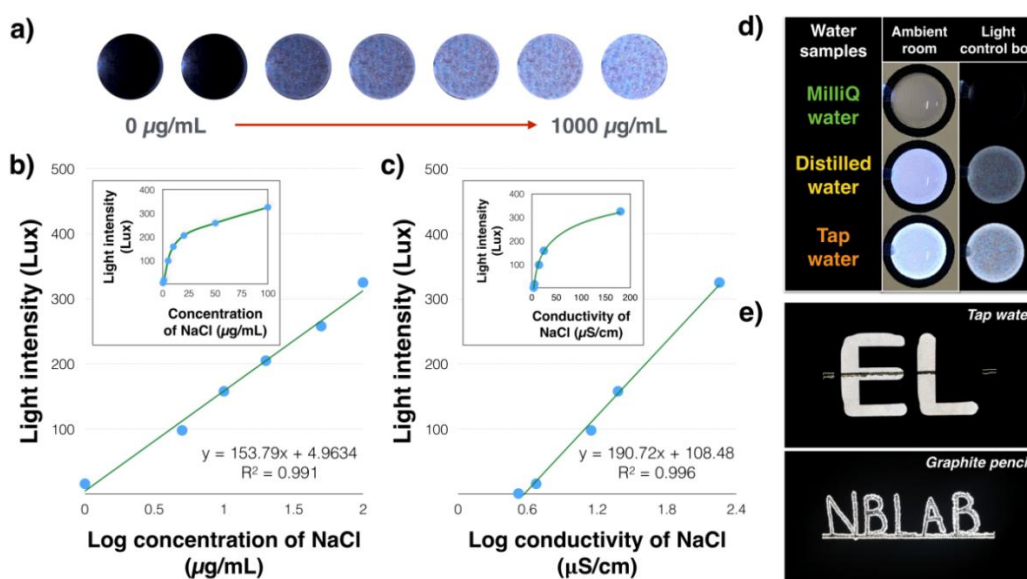
**Figure 3.2.8** (a) Photographs of the ACEL display on exposure of NaCl solution having different ionic concentrations/conductivities. (b) The linear calibration of a plot between light intensity (lux) and log concentration of NaCl; and inset depicting the dependence of the light intensity vs. concentration of NaCl. (c) The linear calibration of a plot between light intensity (lux) and log conductivity of NaCl; and inset depicting the dependence of the light intensity vs. conductivity of NaCl. (d) Photographs of the ACEL display testing with milli-Q, distilled, and tap water under ambient light (left) and light control box (right). (e) Photograph of alphabets on the responsive ACEL display written by tap water and graphite pencil.

### 3.2.3.4 ACEL humidity sensor and breath sensor

The potential of the electroluminescent platform was further broaden to humidity sensing application which is of prime importance in various fields. Numerous publications for humidity monitoring have been reported over years. Most of them are based on capacitive and resistive change [85-92]. However, to the best of our knowledge, there is no report for humidity sensor based on electroluminescence. Therefore, a humidity sensor based on ACEL lamp using BES

and TES structure functionalized by graphene oxide (GO)/Nafion nanocomposite as a sensitive material was applied here for the first time.

In this application, the sensing mechanism for an ACEL-based humidity sensor could be attributed to the proton conduction of nanocomposite formed between the 2D material (GO) and Nafion under a hydrated environment. In particular, GO derivative with oxygen-containing functional groups (−O−, −OH, and −COOH) possesses super-permeability to water molecules [93]. At low relative humidity (RH), the physisorbed water molecules on active site of GO (oxygen-containing functional groups) cannot move freely because of the restriction from double H−bond. For this reason, large energy is required for the hopping transfer of protons between adjacent active site, and therefore, results in strong electrical resistance. However, as %RH increases, the physisorbed water layer becomes mobile and behaves like a bulk liquid. Thus, the proton hopping mechanism between water molecules occurs in GO with charge transport taking place via the conductivity generated by a Grotthuss chain reaction, which in turn yields in an increase of conductance [94, 95]. Correspondingly, Nafion, a sulfonated fluoropolymer is also used to synergistically enhance ultrahigh proton conductivity in hydrated conditions [96-98]. This sulfonic acid hydrophilic group attached to the hydrophobic backbone in Nafion enables proton transport through hydrated ionic clusters and varies influentially with the humidity [97]. Moreover, the microstructures especially the percolated channel formed by these ionic clusters which may be sculptured by phase separation or colloidal packing is the key factor related to the proton conductivity of Nafion membrane [97, 99].

In this study, a larger light emission sensing area with surrounding square electrode was designed for both TES and BES to obtain maximum light intensity for humidity measurement. A simple drop-casting of the nanocomposite between GO

and Nafion onto the phosphor layer of ACEL display raises interesting sensing applications. The nanocomposite based ACEL sensor was then characterized by SEM. SEM image of the composite device was then compared with those made with individual GO and Nafion. The formed GO film (figure 3.2.9a) exhibited a crumpled surface of nanosheet whereas Nafion film (figure 3.2.9b) displayed a smooth surface with several pores in the films. By contrast, the pore was not observed on the nanocomposite film covering ACEL display (figure 3.29c). The mixing of the Nafion with GO was responsible for the increase in the smooth surface with random nanoflakes of GO. The fabrication of the GO/Nafion nanocomposite was also confirmed by SEM/EDX analysis (figure 3.2.10). The presence of the F peak verified the presence of Nafion in GO films. It should be noted that the peaks of Zn, Al, S, Ba, and Ti could be ascribed to the elemental constituent of underlying layer of ACEL display. XPS technique was further use for confirmation of the Nafion composition in GO (figure 3.2.11). In addition, the thickness of the drop-cast film was found to be 1.488 µm, as measured by stylus profilometer (figure 3.2.12).
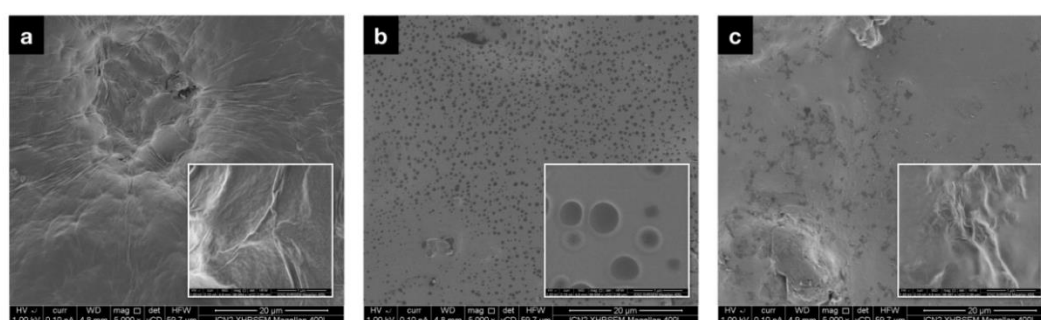


**Figure 3.2.9** SEM images of an ACEL display coating with (a) GO; (b) Nafion; and (c) GO/Nafion nanocomposite.
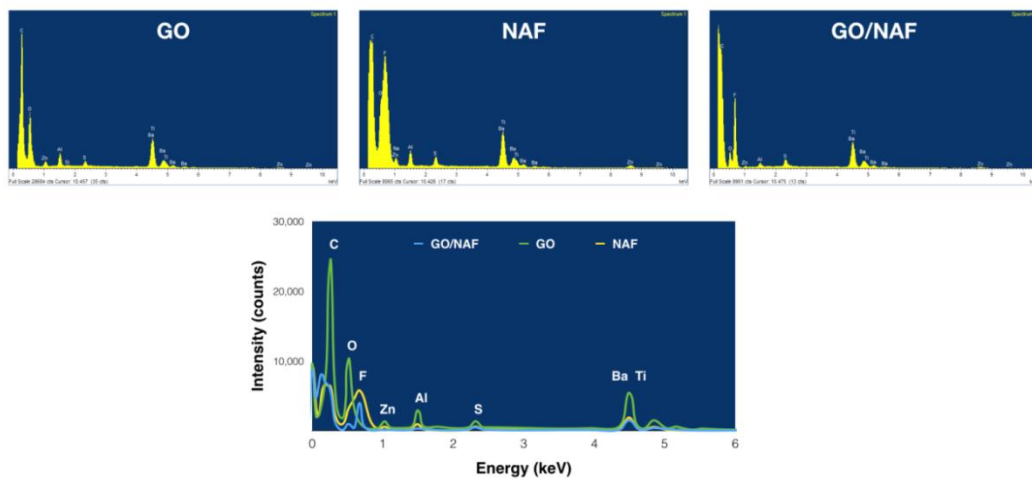
**Figure 3.2.10** EDX spectra of GO, Nafion, and GO/Nafion nanocomposite.
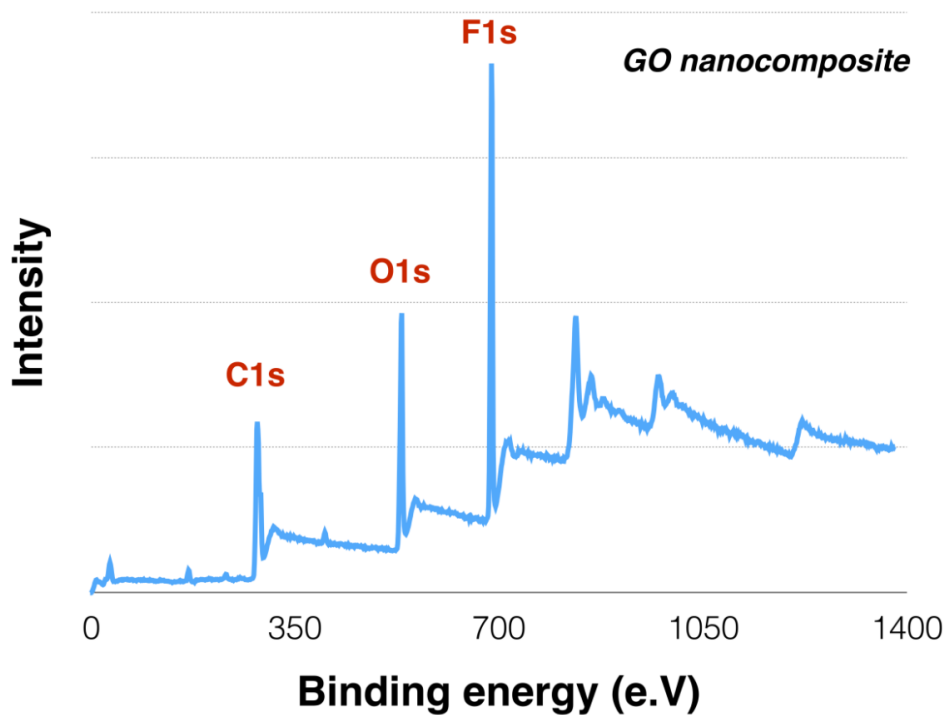


**Figure 3.2.11** XPS spectra of GO/Nafion nanocomposite.
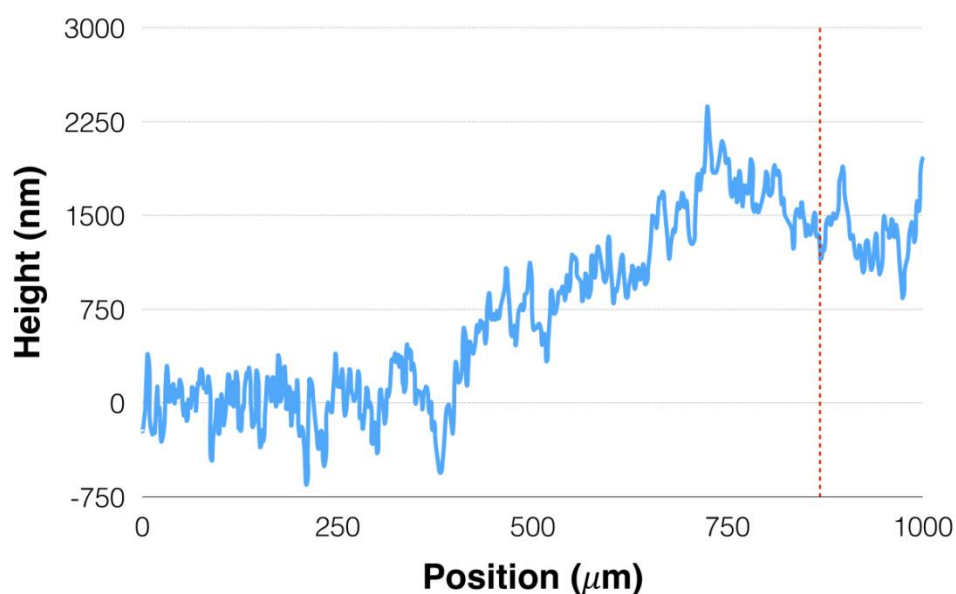
**Figure 3.2.12** Profilometer height profile of the GO/Nafion film on ACEL display.

To obtain the best sensitivity towards humidity, different proportions of GO and Nafion (1:9, 3:7, 5:5, 7:3 and 9:1) were then investigated at different relative humidity (RH), where RH was controlled in a custom-made chamber (figure 3.2.13a (i)) using vapor pressure from a set of saturated salt solution. As illustrated in Figure 3.2.13b, the light intensity response was inferior when GO was the major component (proportion) in the composite. The coverage of a phosphor layer with a brownish solution of GO can lead to a poor response. In contrast, when Nafion was in major proportion in the nanocomposite, higher sensitivity was achieved owing to its ultrahigh proton conductivity, especially for 3:7 ratio which exhibited maximum response. It is important to remark that the synergistic effect between GO and Nafion also resulted in higher light intensity response regarding humidity compared to the

role of Nafion alone. The GO:Nafion composition of 3:7 was finally selected to obtain maximum efficiency for both TES and BES.

The performance of the sensor with TES configuration was firstly studied. It was obvious that no light is emitted at low RH. However, the light is automatically turned on in high humidity conditions (inset of Figure 3.2.13c (lower)). The exponential behavior of light intensity (lux) on the humidity is observed within studied range (inset of Figure 3.2.13c (upper)). This exponentially-sensitive behavior has been reported in several GO-based humidity sensors elsewhere, which might arise from mass loading effect of water adsorption at high RH [100, 101]. Figure 3.2.13c shows the dependence of the logarithmic conductance-related light intensity (lux) on different RH values at room temperature. It is obvious that the logarithmic light intensity response increases linearly with the increment of %RH. Additionally, the humidity sensing capability of the ACEL display with BES architecture was further investigated. In this way, an ACEL light panel was fabricated on a transparent electrode of ITO, following BES structure (see Figure 3.2.1a). However, a silver top-electrode was replaced by a sensitive layer of GO nanocomposite as is schematically shown in figure 3.2.13d. With this modified architecture, the direct feedback from humidity on nanocomposite layer would allow the phosphor layer on the opposite side to emit light. A light intensity response to different RH degrees is shown in Figure 3.2.14. A similar trend can be clearly observed, as in case of TES, whereby the light intensity increases exponentially with %RH. An enhanced sensitivity might be caused by the protective phosphor layer which is not hindered by the layer of GO nanocomposite. This humidity related light emission response holds a great promise to develop an innovative ACEL based humidity sensor for practical applications.
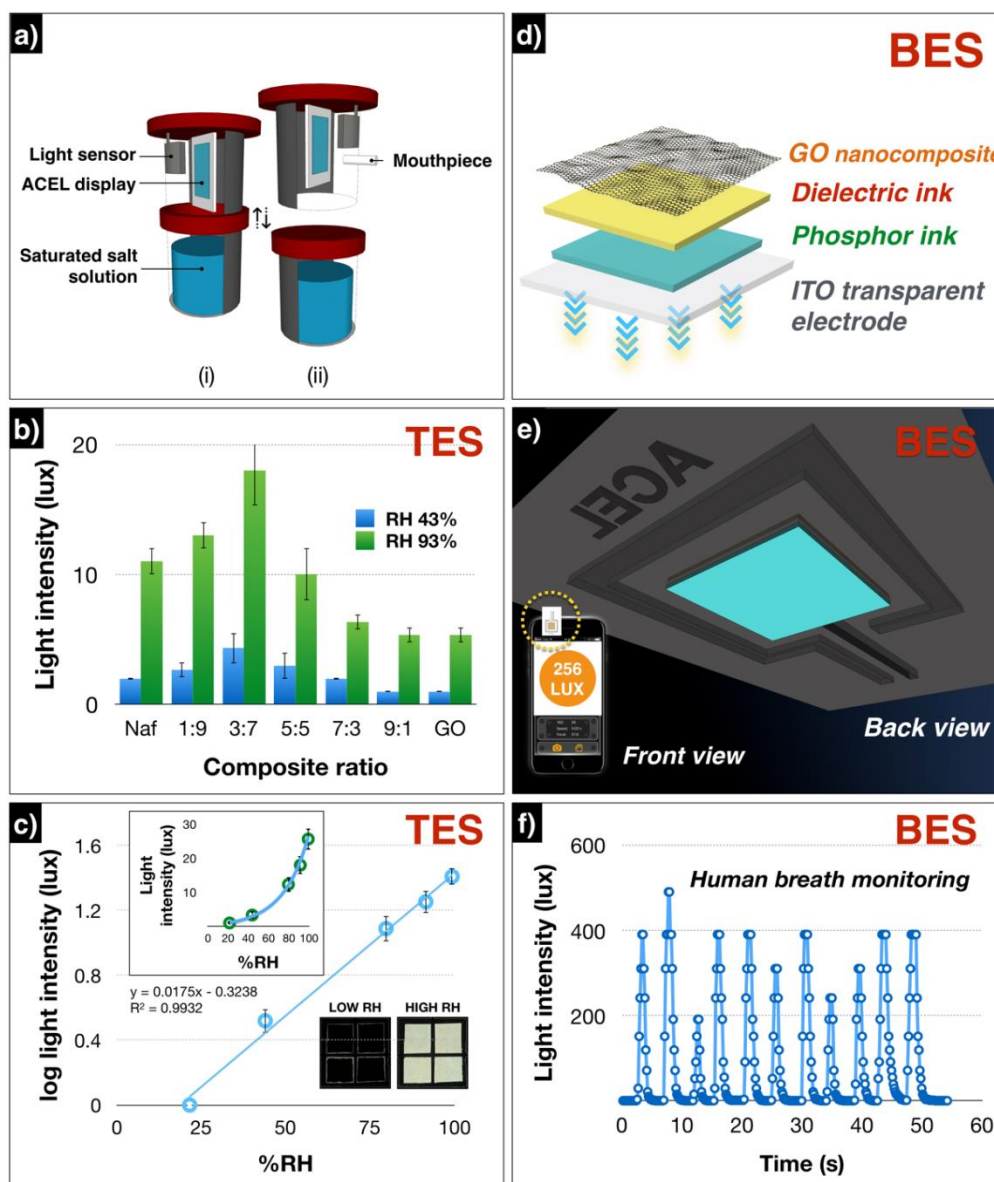
**Figure 3.2.13** (a) Schematic illustration of a custom-made chamber for (i) controlling humidity and (ii) breath monitoring measurements. (b) Responses obtained for different GO / Nafion ratios using ACEL with TES configuration. (c) A linear calibration plot between the logarithmic light intensity (lux) and %RH; and inset (upper) showing the exponential behavior between the light intensity response under different RH, (lower) real image results of an ACEL sensor upon exposure to different humidity levels. (d) Schematic image showing an ACEL sensor with BES architecture functionalized with GO nanocomposite. (e) Schematic illustration of the

back view of ACEL sensor with BES and inset showing device arrangement with a smartphone. (f) The performance of an ACEL sensor with BES architecture for human breath monitoring.
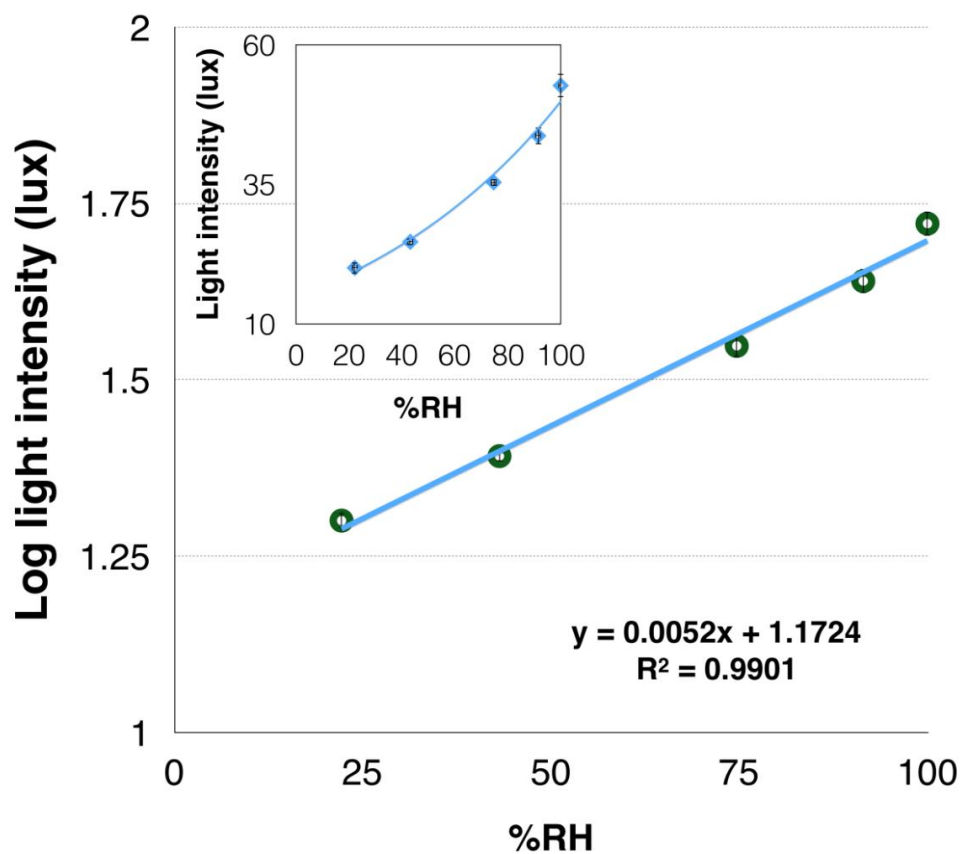


**Figure 3.2.14** A linear calibration plot between the logarithmic light intensity (lux) and %RH; and inset showing the exponential behavior between the light intensity response under different RH using ACEL sensor with BES architecture.

The capability of ACEL humidity sensor can be extended to further uses as point-of-care (POC) sensing device. Such a humidity-dependence light emission enables monitoring of human breathing through the moisture content in the exhaled

air. The physical characteristics of the breath, such as breath frequency can provide helpful health condition information about pulmonary and cardiac symptoms [102-104].

In this experiment, the air exhaled was introduced using cylindrical mouthpiece connected to the custom-made chamber as illustrated in the experimental setup in the Figure 3.2.13a (ii). The response was then monitored through the light emission from ACEL sensor with TES architecture. The breath sensor performance of repeated exhale/inhale cycles is displayed in Figure 3.2.15. Once the breath was blown, the substantial response from light emission is rapidly detected. After the breath is off, the light emission was then gradually decreased. Different exhaled patterns including normal, deep and shallow breath were also reflected in different light intensity responses (dashed circle).
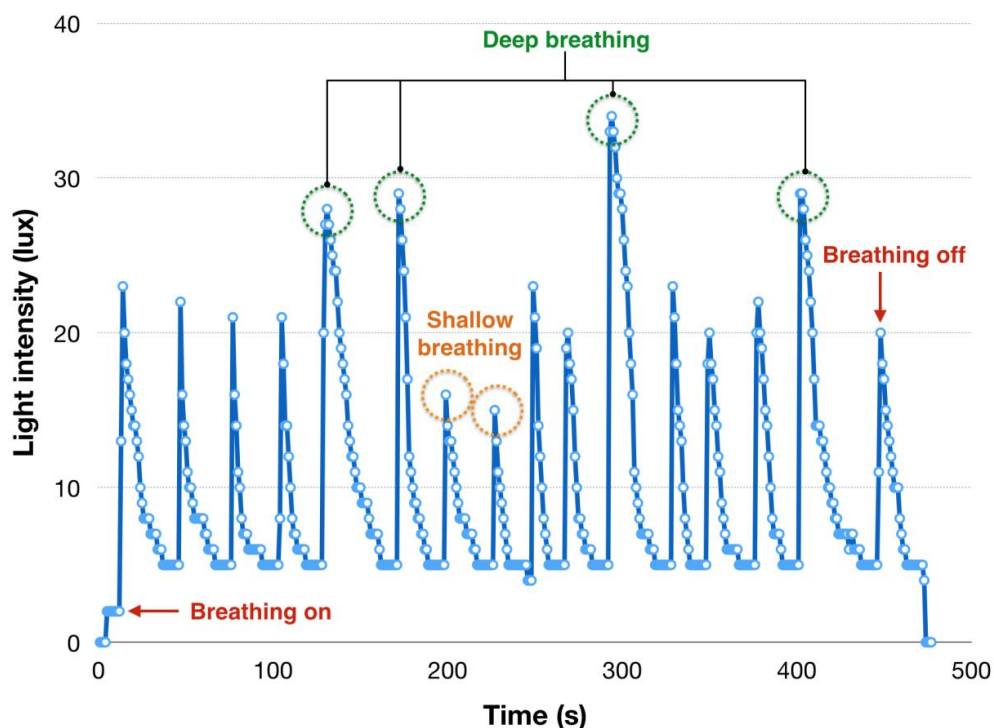
**Figure 3.2.15** The performance of an ACEL sensor with TES architecture for breath monitoring under different exhaled patterns.

The response and recovery times were further evaluated from single exhale/inhale cycles. As is observed in Figure 3.2.16, the sensor response to a breath could be as fast as 1s (time interval of the light sensor was limited at 1s), while the recovery time (defined as the time required to recover up to 90% of initial baseline) was varied depending on breathing patterns. For shallow and normal breathing, the recovery time was around 7s. However, in the case of deep breathing, the recovery time may take up to 12.5s (without applying any heat treatment). A huge difference between response and recovery time could be assigned to the generous hydrophilic functional moiety in GO and Nafion which required a longer time to desorb water molecules [105]. This experiment suggests that the developed breath monitoring sensor is capable to track the breathing frequency by a sensitive ACEL display.
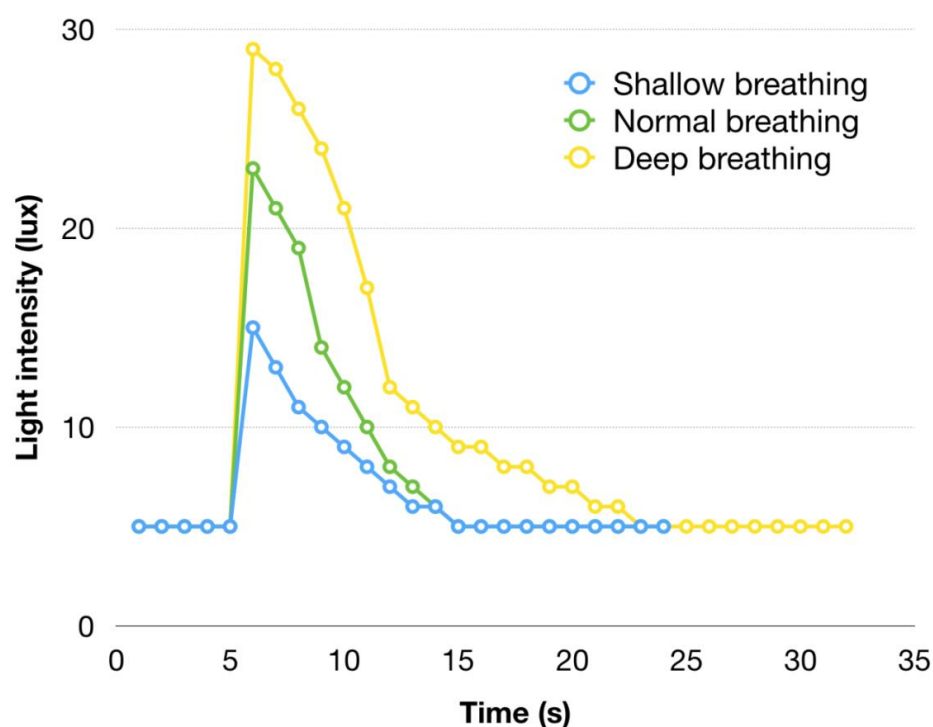
**Figure 3.2.16** The response and recovery profile of an ACEL breath sensor.

To allow portability and simplicity for on-field POC testing, an ACEL humidity sensor integrated with the smartphone was then developed and demonstrated. Taking advantages of the BES configuration, the light emitted from the bottom of the ACEL sensor can be directly monitored through the light sensor embedded in a digital camera. As represented in Figure 3.2.13e, the back side of the ACEL display (1.3 × 1.3 cm) was attached to the front light sensor of a smartphone. Clearly, the smartphone-based sensor exhibits a notable response towards human breathing (Figure 3.2.13f). Interestingly, both response and recovery time were estimated to be less than 1s. This ultrafast response/recovery time facilitates the detection of a broad range of respiratory rate in the patient. Although a clear electrode is mandatory for this architecture, an immediate and straightforward analysis was achieved without the need to use advanced equipment. A simple operation together with real-time

monitoring enables it to use even by the untrained user. Based on this result, the smartphone-based ACEL sensor for human breath monitoring offers an excellent performance to become a smart tool for clinical diagnosis.

### 3.2.4 Conclusions

In summary, this research has demonstrated the performance of a flexible ACEL display in sensing applications. The proposed device can be simply fabricated by a screen-printing method. In this platform, light emission occurs when conductive materials touched the sensing area of the phosphor layer, without requiring any top-transparent electrode. This conductance-dependence light emission enables the display to sense and visualize different water samples with various ionic concentrations. The direct response from pencil writing on ACEL display is also illustrated in this platform. For the first time, GO nanocomposite is integrated within an ACEL sensor and used to measure humidity. This innovative sensor can also be applied to human breath monitoring, where the light is automatically turned on when the exhaled air is in contact with the device. This flexible ACEL sensor holds a great potential for future advancement in wearable sensor technology in addition to other applications with interest for diagnostics as well as environmental monitoring, safety and security.

# CHAPTER IV

# DEVELOPMENT OF NANOMATERIALS-BASED MINIATURIZED PLATFORMS FOR ELECTROCHEMICAL SENSING APPLICATIONS

This chapter is divided into two main parts. Part I (section 4.1) reports on fabrication and characterization of graphene-Nafion nanocomposite and its application in highly sensitive electrochemical sensor for vitamin D determination. Part II (section 4.2) describes a development of a 3D capillary-driven paper-based sequential microfluidic device for sensing applications.
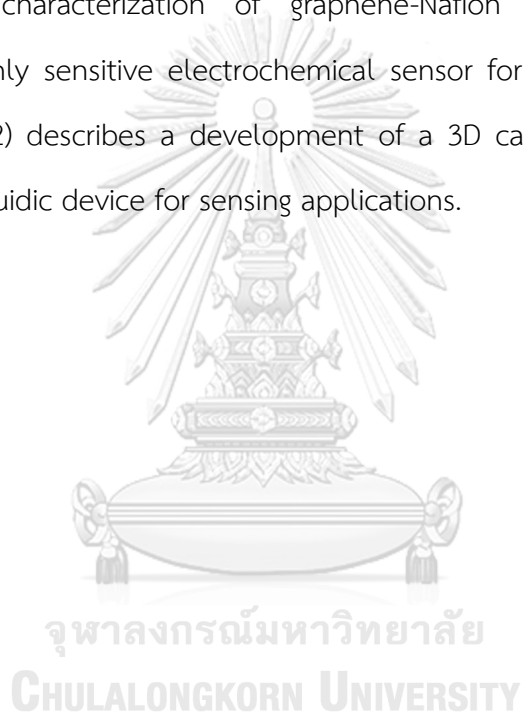
PART I

## 4.1 Fabrication and Characterization of Graphene-Nafion Nanocomposite and Its Application in Highly Sensitive Electrochemical Sensor for Vitamin D Determination

Abdulhadee Yakoh[a], Orawon Chailapakul[a,b*] and Weena Siangproh[c*]

[a] Electrochemistry and Optical Spectroscopy Center of Excellence (EOSCE), Department of Chemistry, Faculty of Science, Chulalongkorn University, 254 Phayathai Road, Patumwan, Bangkok 10330, Thailand

[b] Center for Petroleum, Petrochemicals and Advanced Materials, Chulalongkorn University, 254 Phayathai Road, Pathumwan, Bangkok 10330, Thailand

[c] Department of Chemistry, Faculty of Science, Srinakharinwirot University, Sukhumvit 23, Wattana, Bangkok 10110, Thailand

* Corresponding author

## Abstract

This paper describes the fabrication, characterization and application of graphene/Nafion nanocomposite for the electroanalysis of fat-soluble vitamin D. The electrochemical properties of the graphene/Nafion nanocomposites were investigated using cyclic voltammetry and electrochemical impedance spectroscopy using $Fe(CN)_6^{3-/4-}$. Interestingly, a greatly enhanced faradaic signal current with respect to the background current (S/B ratio) was clearly achieved. The optimum conditions for the determination of vitamin D in ethanol:NaClO4 (60:40%v/v) were established using adsorptive stripping square wave voltammetry. The sensor demonstrates an excellent linear relation in the range of 0.5-30 μg mL$^{-1}$ with a correlation coefficient of 0.9916. The limit of detection (LOD) and quantitation (LOQ) from the calculation were found to be 68.8 and 229.6 ng mL$^{-1}$, respectively, therefore, it can be used to determine vitamin D in real samples. In addition, an anti-fouling electrode based on a graphene/Nafion nanocomposite was first introduced for the electroanalysis of vitamin D, and the possibility of multiple usages of the electrode without any of the usual electrode adsorption restrictions was explored. The direct analysis of vitamin D was successively analyzed with satisfying results of up to 10 repeated usages. Compared to conventional chromatographic methods, the electrochemical sensor outlined here demonstrated a faster, easier, and much cheaper approach that enables the continuous monitoring of the total quantity of vitamin D in supplementary samples with good reliability, selectivity and accuracy.

**Keywords**: Vitamin D, Graphene, Nafion, Anti-fouling, Electroanalysis

### 4.1.1 Introduction

Vitamin D is a lipid-soluble nutrient that primarily exists in two forms: vitamin $D_2$ (ergocalciferol) and vitamin $D_3$ (cholecalciferol). Vitamin D originates from two sources: endogenous, which is from the dermal synthesis from cholesterol; and exogenous, which is ingested from the diet and supplements [106]. The vital functions of vitamin D are regulating the blood levels of calcium and phosphorous and facilitating normal immune system function [107, 108]. An insufficient amount of vitamin D can cause abnormal growth and development of bones and teeth (rickets, osteomalacia, osteoporosis) and increase the risk of certain diseases [109, 110].

The association of official analytic chemists international (AOACI) has established official chemical methods for vitamin D analysis based on liquid chromatography: Method 992.26—vitamin $D_3$ in ready-to-feed milk-based infant formula (AOAC, 2007b), Method 995.05—vitamin D in infant formulas and enteral products (AOAC, 2007a), and Method 2002.05—vitamin $D_3$ in selected foods (milk and cheese) (AOAC, 2007d). Likewise, several approaches involving liquid chromatography/mass spectrometry have been extensively reported and developed by many researchers [111-121]. Unfortunately, these previously reported methods suffer from the drawbacks of tedious procedures, complex instrumentation, long analysis time, and the requirement for a skilled analyst. Alternatively, electrochemical detection is a promising method to circumvent these inherent shortcomings owing to their remarkable sensitivity and accuracy, experimental simplicity, fast response time, and compact setup. To date, the electrochemical detection of the vitamin D has been rarely explored on account of the lipid-soluble nature of the vitamin and needs to be performed in non-aqueous media. In addition, one common issue with vitamin D is that it undergoes adsorption during the oxidation steps, which blocks the surface and yields electrode fouling [121-124]. This

phenomenon can limit the repeated usage of the electrode, especially in continuous monitoring applications. Therefore, for a long-running electrode, electrode modification is a crucial step to eliminate or minimize this effect.

Several means have been reported to prevent the adsorption on an electrode surface for electrochemical sensing applications. Electrode modification using some additives as anti-fouling agents is also gaining attention because of their excellent character. Poly(3,4-ethylenedioxythiophene) (PEDOT), for instance, has been widely applied to modify electrodes through electropolymerization methods [125-128]. However, this material demands tight process control during the polymerization procedure because changing parameters can lead to widely different final results [129-131]. Therefore, it has been difficult to conduct this procedure. Furthermore, the use of Nafion, a hydrophobic Teflon-like backbone with hydrophilic perfluoroether side chains bearing terminal sulfonic acid groups, has been a long-standing goal in the community for the development of various electrochemical sensors. Nafion exhibits not only excellent chemical inertness, catalytic activity, and high permeability to the cation but also an anti-fouling capability [132-134]. Modification with Nafion offers experimental simplicity and eliminates prolonged additional steps in electrode pretreatment, making it a very attractive material from an electrochemical viewpoint.

Lately, the integration of nanomaterials and Nafion for the preparation of hybrid nanocomposites has gained popularity, as these materials can synergistically enhance the performance of the electrochemical sensor. Graphene, the well-publicized and prominent allotrope of carbon, is notably one of the most powerful nanomaterials and is widely used in the development of hybrid materials. Many studies of graphene/Nafion-based electrochemical sensors have shown that the use of Nafion prevented electrode fouling and served as an effective dispersing agent to

exfoliate graphene sheets to prevent aggregation [29, 135-137]. Due to the extraordinary electron transfer ability of graphene incorporated with the excellent properties of Nafion as mentioned earlier, a graphene/Nafion hybrid nanocomposite holds a great promise for electrochemical applications.

Herein, an anti-fouling strategy for the highly sensitive determination of fat-soluble vitamin D based on a graphene/Nafion nanocomposite was described. In this paper, a graphene-based screen-printable ink was used to fabricate a graphene/Nafion nanocomposite with good reproducibility. In addition to improved sensitivity, the graphene/Nafion nanocomposite exhibited a lower background current in comparison with the graphene screen-printed electrodes (SPEs), which exhibited a larger signal-to-background (S/B) ratio. Eventually, under the synergistic effect of graphene and Nafion, a sensitive, reusable, and simple electrochemical sensor was developed for evaluating the total level of vitamin D. Diverse pharmaceutical drugs and dietary supplements were analyzed, and the results obtained from the developed sensor were highly consistent with results from the LC-MS/MS method.

### 4.1.2 Experimental

#### 4.1.2.1 Materials and reagents

Fat-soluble vitamins (cholecalciferol (vitamin $D_3$), ergocalciferol (vitamin $D_2$), retinyl acetate (vitamin A), DL-$\alpha$-tocopherol acetate (vitamin E) and phylloquinone (vitamin $K_1$)), thiamine (vitamin $B_1$), riboflavin (vitamin $B_2$), Nafion 117 (5% in lower alcohol), potassium ferricyanide ($K_3Fe(CN)_6$), sodium chloride, and potassium dihydrogen phosphate were acquired from Sigma-Aldrich (www. sigmaaldrich.com). Potassium chloride, disodium hydrogen phosphate, and ethanol were acquired from Merck (http://www.merckmillipore.com). Sodium perchlorate monohydrate and

tetrabutylammonium hexafluorophosphate were purchased from Fluka Chemika (https://www.fishersci.ch/content/fishersci/eu/en_CH/brands/h/honeywellfluka.html). Potassium sulfate, calcium sulfate, and zinc nitrate were obtained from Ajax Finechem (http:// www.ajaxfinechem.com). All chemicals were of analytical grade and used as received, and all solutions were prepared by using purified water (18.2 M$\Omega$ cm) from a Milli-Q, Millipore water purification system (http://www.merckmillipore.com).

### 4.1.2.2 Instrumentation

Transmission electron microscopy (TEM) images were recorded by an H-7650 transmission electron microscope (Hitachi model, http://www.hitachi.com). The surface morphologies were studied using a JSM-7610F field emission scanning electron microscope (FESEM) (JEOL Ltd., https://www.jeol.co.jp).

### 4.1.2.3 Electrode fabrication

A wax printing technique was used to define a hydrophobic barrier. An Adobe illustrator CC (Adobe systems, USA) was used to create the device design. The wax pattern was printed onto an inkjet printable PVC sheet using a wax printer (Xerox ColorQube 8570, http://www.office.xerox.com). For the electrochemical measurements, three electrodes were fabricated onto the wax-patterned sheet using a silk screen-printing method. To prepare the graphene/Nafion nanocomposite, 0.5 g of the graphene ink (Gwent group, http://www.gwent.org) was finely homogenized with 100 µL of 0.1% w/v Nafion solution. This composite ink was then printed on a patterned substrate, serving as a working electrode (WE) and a counter electrode (CE). A silver/silver chloride ink (Gwent group, http://www.gwent.org) was

subsequently printed as a reference electrode (RE) and the conductive pads. After each screen-printing step, the printed electrode was allowed to dry in an oven at 65°C for 1 hour. Lastly, to complete the device, an adhesive tape was attached to the bottom of the WE to confine the surface area of the working electrode.

### 4.1.2.4 Electrochemical measurements

Cyclic voltammetry and adsorptive stripping square-wave voltammetry were performed with a potentiostat model 1232A (CH instrument, https://www.chinstruments.com) at room temperature. For vitamin D detection, standard solutions of vitamin $D_3$ were prepared in an ethanol:$NaClO_4$ (60:40% v/v), and a 30 μL aliquot was used throughout the experiments. For adsorptive stripping square-wave voltammetry (SWV), an amplitude of 25 mV, a potential increment of 4 mV, and a frequency of 10 Hz were selected.

Electrochemical impedance spectroscopy (EIS) was carried out using an Autolab electrochemical system with a potentiostat PGSTAT 204 (Eco-Chemie, http://www.metrohm-autolab.com) in a solution of 5.0 mM $K_3Fe(CN)_6$ with a sinusoidal potential modulation of 0.1 V amplitude in the 0.1 Hz to 100 kHz frequency range and a logarithmic scale of 10 points per decade.

### 4.1.2.5 Real sample preparation

Dietary supplements and pharmaceutical drugs containing vitamin D were bought from the drugstore (Bangkok, Thailand). These tablets were finely ground and then solubilized in ethanol:$NaClO_4$ (60:40%v/v). Additionally, ultrasonic agitation was used for 10 min to complete the solubilization of vitamin D, and then the sample was further analyzed by optimized square-wave voltammetry (SWV).

### 4.1.3 Results and discussion

#### 4.1.3.1 Electrochemical characterization of the screen-printed electrodes

The electrochemical properties of the graphene/Nafion nanocomposites were initially investigated using cyclic voltammetry. Cyclic voltammograms of 5 mM $Fe(CN)_6^{3-/4-}$ in 0.1 M KCl using various screen-printed electrodes (SPEs) are presented in the inset of Figure 4.1.1A. As observed with graphene and the graphene/Nafion nanocomposite (green dashed line and blue line, respectively), the magnitude of current response is far greater than that of the carbon SPE (red dashed line), which can be attributed to the excellent rate of electron transfer of the graphene material. Nevertheless, in 0.1 M KCl (Figure 4.1.1A), the background current recorded with the graphene/Nafion nanocomposite was smaller than the currents measured using the other materials. This behavior is likely due to the background reduction capability of Nafion. In particular, Nafion consists of three regions: the hydrophobic fluorocarbon backbone, the hydrophilic cluster of sulfonic acid group, and the interfacial region. These structures provide a strong charge exclusion, which prevents much of the redox-active interferents from affecting the sensor responses [133, 138]. Based on the large faradaic current with respect to the small capacitive current, the signal-to-background (S/B) ratio can effectively be enhanced. The S/B ratios of the CV current for $Fe(CN)_6^{3-/4-}$ reduction in 0.1 M KCl were exhibited in the following order: the graphene/Nafion SPE (S/B = 125.9) > the graphene SPE (S/B = 90.09) > the carbon SPE (S/B = 40.53), as shown in Table 4.1.1.
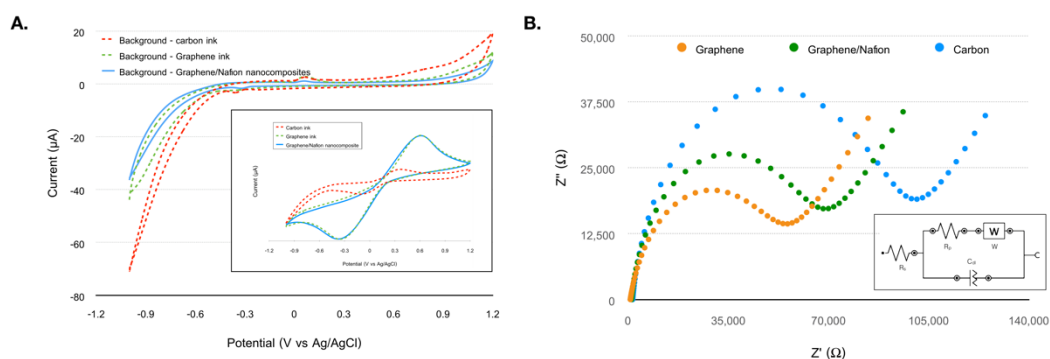
**Figure 4.1.1** (A) Cyclic voltammograms for 0.1 M KCl and 5 mM Fe(CN)$_6^{3-/4-}$ (inset) using the screen-printed carbon, graphene, and graphene/Nafion electrodes. The potential sweep rate was 100 mV s$^{-1}$. (B) Nyquist plots for 5 mM Fe(CN)$_6^{3-/4-}$ in 0.1 M KCl using the screen-printed carbon, graphene, and graphene/Nafion nanocomposite electrodes.

**Table 4.1.1** S/B ratio (estimated from the CV current for Fe(CN)$_6^{3-}$ reduction) and double layer capacitance in 0.1 M KCl and EtOH:NaClO$_4$ system at different SPEs.

| Electrode materials | E | S | B | S/B | C (0.1 M KCl) | C (60:40 EtOH:NaClO$_4$) |
|---|---|---|---|---|---|---|
| Carbon | -0.096 | -23.91 | -0.590 | 40.53 | 23.32 | 208.3 |
| Graphene | -0.331 | -104.5 | -1.16 | 90.09 | 3.880 | 40.89 |
| nanocomposite | -0.353 | -107.0 | -0.850 | 125.9 | 3.140 | 24.81 |

Where E: potential (V vs Ag/AgCl), S: signal current (μA), B: background current (μA), and C: capacitance (μF cm$^{-2}$)

For a better understanding, a background electrolyte (0.1 M KCl) was measured using CV at different scan rates to assess any change in the double-layer

capacitance ($C_{dl}$) of different SPEs. The background current originates from a charging of the double layer at the electrolyte/electrode interface and should be directly proportional to the total active surface exposed to the electrolyte [139]. As listed in the Table 4.1.1, the $C_{dl}$ value for the bare carbon electrode was 23.32 µF cm$^{-2}$ in 0.1 M KCl. For the graphene SPE, the $C_{dl}$ value substantially decreased to 3.88 µF cm$^{-2}$ in the 0.1 M KCl system. Even though the capacitance for the carbon materials remains unclear, it was believe that the oxygen functional group impurities presented on the graphite material and the charge density in a stacked layer of graphene in the carbon electrode might lead to a pseudocapacitive contribution, resulting in larger charge storage. In comparison, the graphene/Nafion nanocomposite SPE also decreased the $C_{dl}$ value to 3.14 µF in 0.1 M KCl system. These results suggest that the decrease in the $C_{dl}$ value of the graphene/Nafion nanocomposite relative to the graphene SPE was related to a decrease in the electroactive surface area. This reduction in the $C_{dl}$ value can possibly be due to the partial coverage of the active surface of graphene by Nafion. A similar behavior was also reported by Gayen et al., in which the coverage of the BDD electrode by Nafion could further decrease the $C_{dl}$ value compared to that of the bare BDD [140]. To address this issue, a further inspection of the electrode morphology and effective surface area will be investigated in the next section.

The electrochemical impedance characterizations of various SPEs were further investigated using electrochemical impedance spectroscopy (EIS). Figure 4.1.1B shows the Nyquist plots for 5 mM Fe(CN)$_6^{3-/4-}$ in 0.1 M KCl. For the carbon SPE (blue dots), the plot shows a semicircle and a straight line with an angle of 45°, which indicates typical diffusion-controlled redox behavior at the planar electrode [139]. A decrease in the semicircle radius was observed in the graphene SPE (orange dots), indicating a depletion in the charge transfer resistance ($R_{ct}$). This depletion is

due to the superior electron transfer ability of graphene, which causes the apparent reduction in $R_{ct}$. However, when the nanocomposite SPE was performed (green dots), the $R_{ct}$ slightly increased, which indicates the successful integration of Nafion into graphene [141]. This phenomenon could be attributed to the Nafion itself, which may present an electrostatic repulsion blocking layer toward the electron exchange of $Fe(CN)_6^{3-/4-}$ at the electrode-solution interface [141]. Despite the considerable increase in $R_{ct}$, the selection of the electrode material may have been biased toward the graphene/Nafion nanocomposite regarding the S/B ratio enhancement and the anti-fouling character of the electrode.

### 4.1.3.2 Morphological characterization and effective surface area estimation

The morphologies of the three different electrodes, carbon, graphene and the graphene/Nafion nanocomposite, were characterized by SEM. In Figure 4.1.2, panels a and d show SEM images of the carbon electrode at 5,000x and 10,000x amplification, respectively. A smooth textured region with the irregular shape of carbon was clearly seen over the surface of the SPE. Nevertheless, the SEM images of graphene, as displayed in panels b and e (5,000x and 10,000x amplification, respectively), illustrated a rough and crumpled surface of the graphene sheets that majorly covered the surface, leading to a considerable sensitivity improvement over the carbon materials. With the addition of Nafion (panels c and f at 5,000x and 10,000x amplification, respectively), the prepared composite exhibited a smoother and more film-like texture than the entire graphene surface. The SEM images thus confirmed the aforementioned hypothesis, in which the nanocomposite possessed less surface area than the graphene electrode.

In Figure 4.1.2, panels g and h show TEM images and the corresponding diffraction patterns of the graphene sheet, respectively. These image results further confirm the existence of graphene in the ink composition.
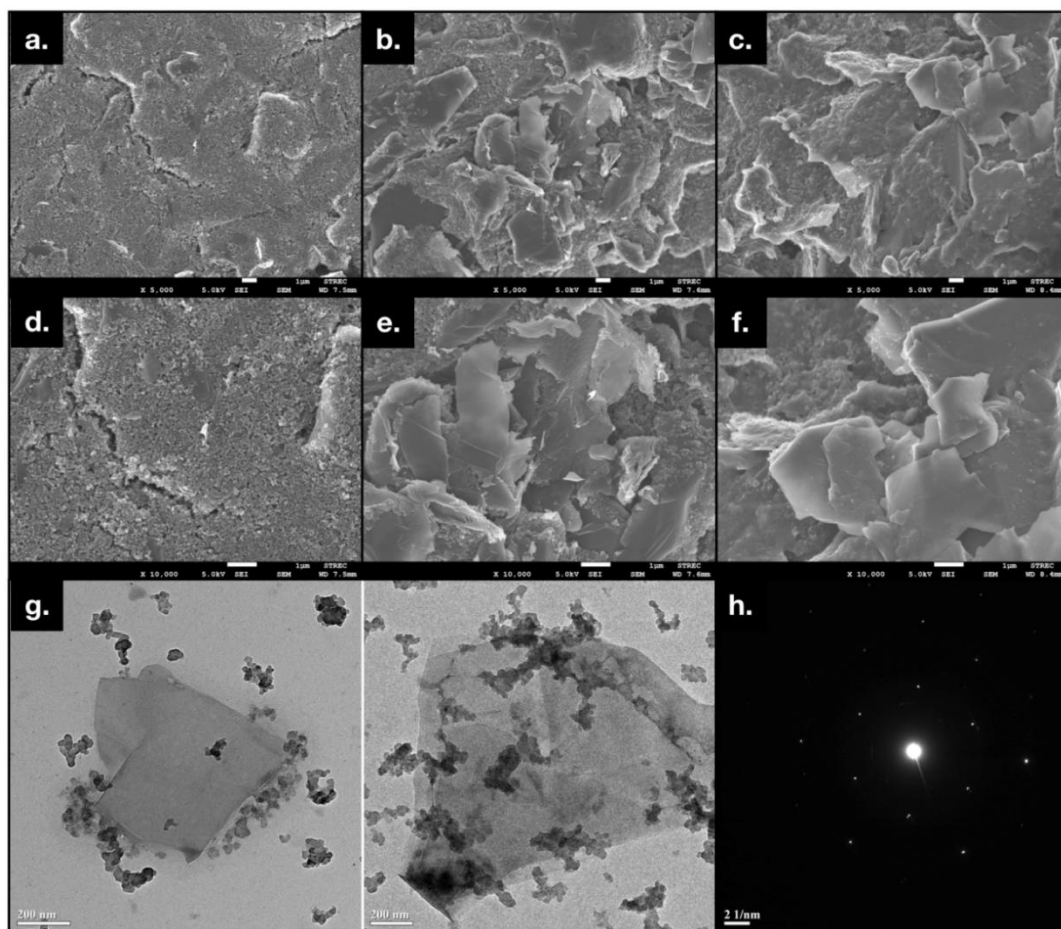


**Figure 4.1.2** SEM images of the screen-printed carbon (a, d), graphene (b, e), and graphene/Nafion nanocomposite (c, f) electrodes at 5,000X (a, b, c) and 10,000X (d, e, f) magnification. TEM images (g) and corresponding diffraction pattern (h) of the graphene sheet in the ink composition.

Furthermore, to illustrate the effective background current reduction in the nanocomposite electrode, the electroactive surface areas of the studied SPEs were

determined employing CV in a 1.0 mM $Fe(CN)_6^{3-/4-}$ solution at various scan rates ($V$). According to the Randles-Sevcik equation ($i_{pa} = (2.69 \times 10^5)\, n^{3/2} A D_o^{1/2} V^{1/2} C_o^*$), where $i_{pa}$ is the peak current in A, $A$ is the area of the electrode in $cm^2$, $C_o^*$ is the concentration of the electroactive species in mM and $D$ is the diffusion coefficient in $cm^2\,s^{-1}$), the approximate electrochemically active surface areas of the carbon, graphene, and graphene/Nafion composite SPEs were estimated (Figure 4.1.3). The electroactive surface areas were calculated to be 0.191, 0.342, and 0.315 $cm^2$ for the carbon, graphene, and the graphene/Nafion nanocomposite electrodes, respectively. Undoubtedly, a nearly two-fold enlargement in the active surface area promoted by graphene compared to the carbon electrode is important for enhancing the sensitivity of the graphene electrode. With the synergistic effect of Nafion, a further background current alleviation arising from a slighter active area was achieved. Some parts of the graphene electrode surface are expected to be covered with Nafion; therefore, the total surface area of the electrode should be less than that of the bare graphene electrode. Based on the experimental observations, these effective surface area results are consistent with the $C_{dl}$ evaluation, SEM images, and background current measurements obtained from cyclic voltammetry, whereby the graphene/Nafion nanocomposite could synergistically enhance the sensitivity while reducing the charging current. Consequently, the graphene/Nafion nanocomposite SPE could clearly enhance the sensitivity for vitamin D determination.
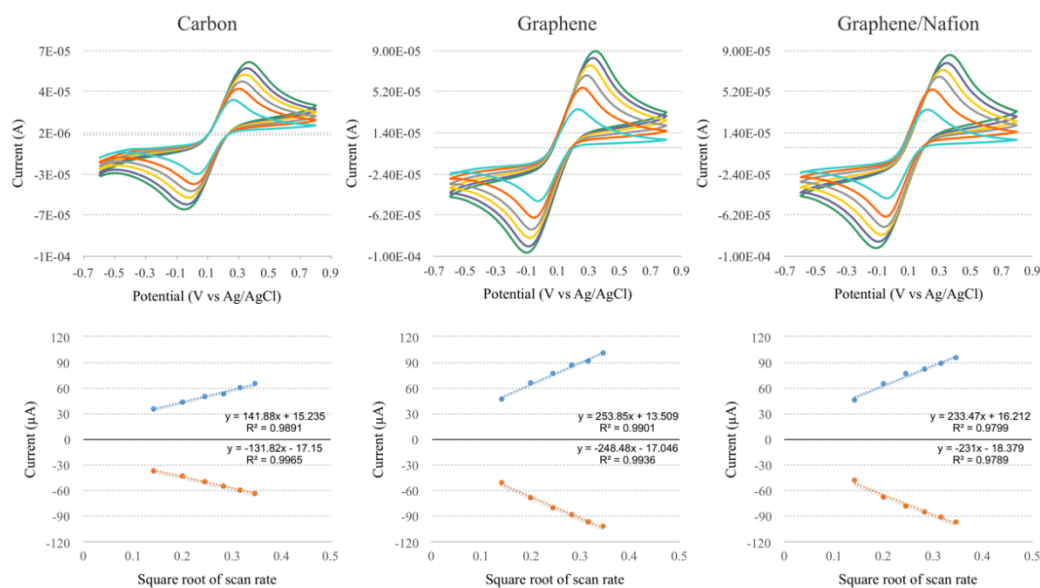
**Figure 4.1.3** (top) Cyclic voltammograms of 1.0 mM Fe(CN)$_6^{4-/3-}$ in 0.1 M KNO$_3$ on the carbon, graphene, and graphene/nafion nanocomposite at different scan rates ranging from 20 to 120 mV s$^{-1}$ and (bottom) the plots between the peak current and square root of the scan rates.

### 4.1.3.3 Electrochemical characterization of vitamin D using different SPEs

The electrochemical measurement of vitamin D on various electrode materials was carried out using cyclic voltammetry within a potential range of 0.5 V - 0.9 V and a scan rate of 20 mV s$^{-1}$. In Figure 4.1.4a-c, voltammograms at various concentrations of vitamin D on the carbon, graphene, and graphene/Nafion SPEs are shown. A similar trend can be clearly observed in the case of Fe(CN)$_6^{3-/4-}$ in 0.1 M KCl. Note that the carbon SPE presents a small peak for only the high concentration of vitamin D (10 µg mL$^{-1}$), and no peak was observed at lower concentrations (Figure 4.1.4a). For graphene and the graphene/Nafion SPE (Figure 4.1.4b and 3c, respectively), the CV curve of vitamin D show a single anodic peak, where the peak current is comparable. However, the background current response recorded in

60%v/v EtOH with the graphene/Nafion SPE was inferior compared to the responses with the graphene and carbon SPEs (Figure 4.1.4d); therefore, the S/B ratio with the graphene/Nafion SPE was almost 2 and 4.5 times larger than the ratios with the graphene and carbon electrodes, respectively, at a vitamin $D_3$ concentration of 10 μg mL$^{-1}$ (Figure 4.1.4e).
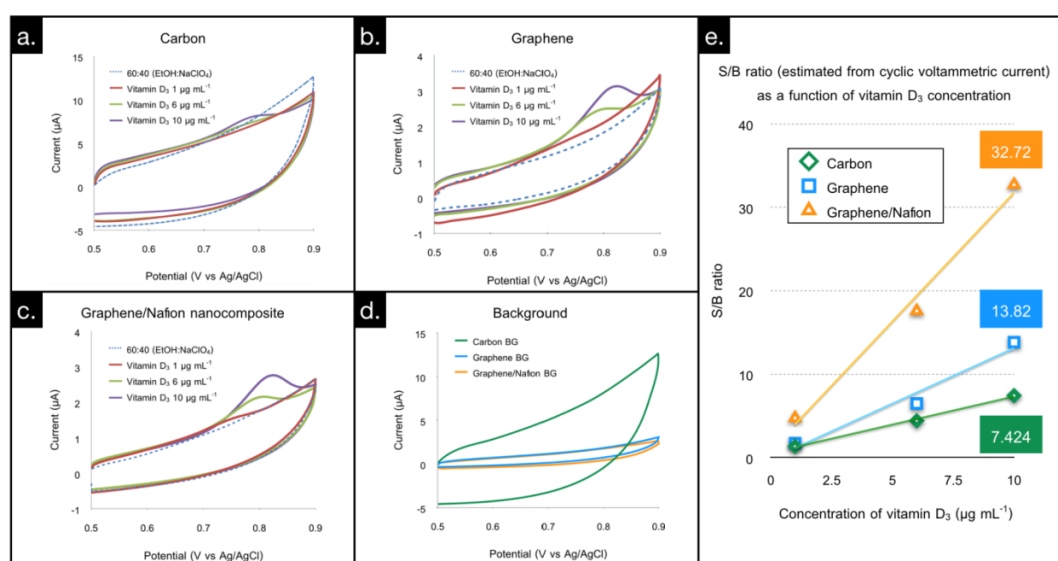


**Figure 4.1.4** Cyclic voltammograms for various concentrations of vitamin $D_3$ using the screen-printed (a) carbon, (b) graphene, and (c) graphene/Nafion nanocomposite electrodes. (d) Cyclic voltammograms for ethanol:NaClO$_4$ (60:40% v/v) background electrolyte using the screen-printed carbon, graphene, and graphene/Nafion electrodes. The potential sweep rate was 20 mV s$^{-1}$. (e) S/B ratio (estimated from cyclic voltammetric current) for vitamin D detection as a function of the vitamin $D_3$ concentration.

In parallel with capacitance measurement performed in 0.1 M KCl, a background solution of ethanol (EtOH) and 0.1 M sodium perchlorate (NaClO$_4$) (60:40%v/v) was also utilized. The electrical double-layer capacitance was exhibited

in the following order: the carbon SPE > the graphene SPE > the graphene/Nafion nanocomposite SPE, which is consistent with $C_{dl}$ value in the 0.1 M KCl system (Table 4.1.1). The results indicated that the nanocomposite electrode of graphene and Nafion could be useful for the high sensitivity determination of vitamin D, which is attributable to the larger faradaic current with respect to a lower charging current relative to the values obtained from the carbon and graphene SPEs.

To further elucidate the electrode reaction of vitamin D at the graphene/Nafion SPE, the influence of the potential scan rate ($V$) on a peak current ($i_{pa}$) of 10 μg mL$^{-1}$ vitamin D$_3$ was studied by cyclic voltammetry at various sweep rates (40-200 mV s$^{-1}$), as shown in Figure 4.1.5. The oxidation peak current of vitamin D increases with an increasing scan rate. Furthermore, a good linear relationship between $i_{pa}$ and $V^{1/2}$ was established, indicating that the mass transport of vitamin D is diffusion controlled.
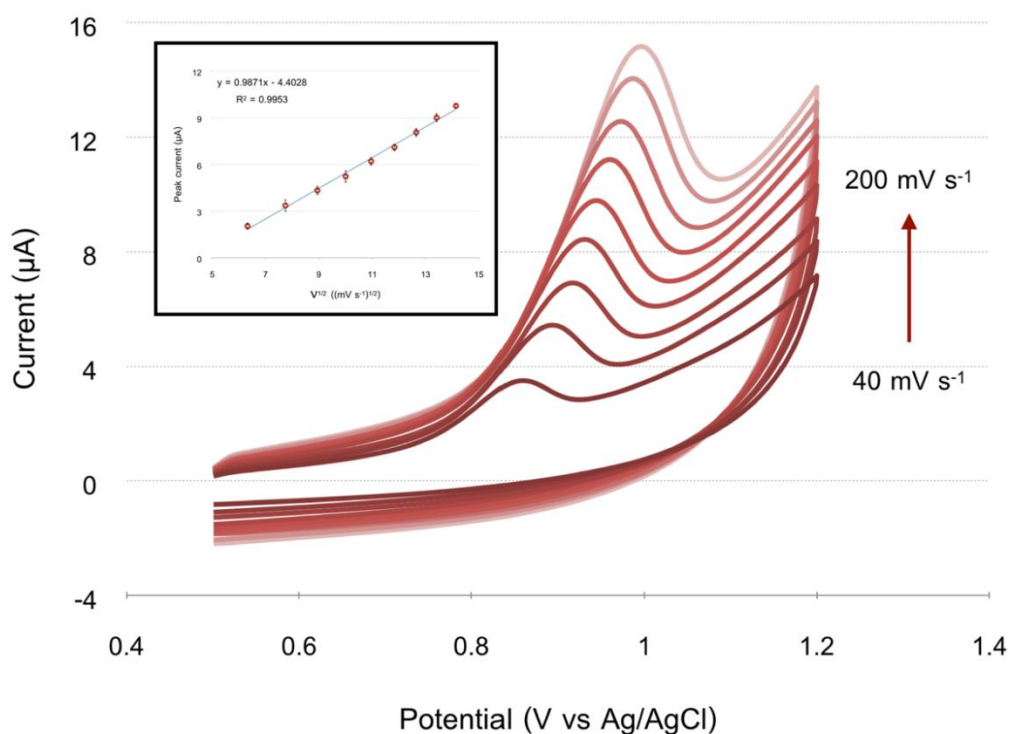
**Figure 4.1.5** Cyclic voltammograms of 10 μg mL$^{-1}$ vitamin D$_3$ in ethanol:NaClO$_4$ (60:40) under different scan rates (40 - 200 mV s$^{-1}$) and the plots between the peak current and square root of the scan rates (inset).

### 4.1.3.4 Optimization conditions for vitamin D determination
### 4.1.3.4.1 Effect of EtOH/NaClO$_4$ ratio (% v/v)

In this work, to obtain a further understanding of the electrochemical behavior of vitamin D, experiments were conducted in solution mixtures between EtOH and water in the presence of 0.1 M sodium perchlorate electrolyte (20, 40, 60 and 80% v/v EtOH) and in a non-aqueous system (100% EtOH). As seen from cyclic voltammograms in Figure 4.1.6a, the ratio of EtOH/water exhibited a significant impact on the oxidative peak current ($i_{pa}$) and oxidative peak potential (E$_{pa}$) of vitamin D. Evidently, 60% EtOH and 40% water yields the highest peak current at a potential of approximately +0.8 V. Even though a less positive peak potential was

observed at a lower percentage of EtOH, the peak current was significantly less than that of 60% EtOH. This finding could be associated with the low solubility of vitamin D in an aqueous-rich solution. Meanwhile, at percentages of EtOH higher than 60% v/v, a smaller peak current with a slight shift toward a positive potential occurred. This small shift is probably because of the high solution resistance in the non-aqueous system that may hinder the electron transfer process. It was reported that the diffusion of ethanol-solvated molecules to the electrode surface was less efficient when the electrode surface was not preferentially hydrated [142]. Therefore, a percentage of the EtOH-water mixture at 60% v/v was chosen as the optimal condition for the determination of vitamin D.
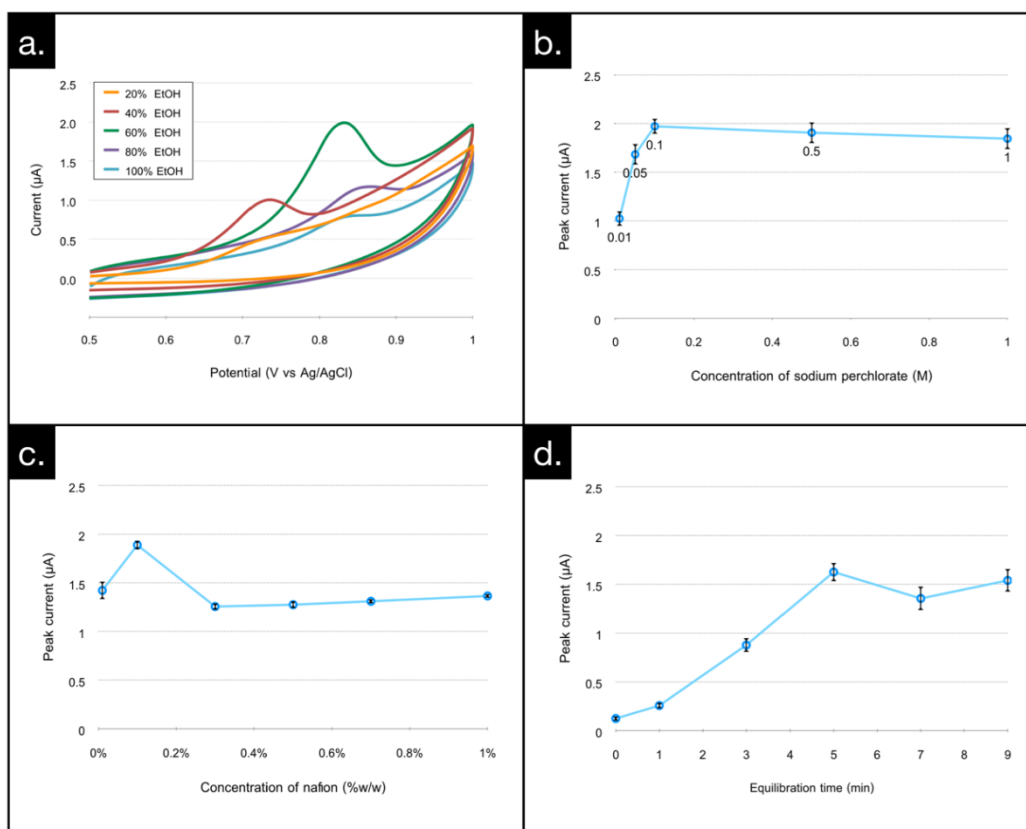
**Figure 4.1.6** Effects of (a) EtOH/water ratio (% v/v), (b) concentration of supporting electrolyte, (c) concentration of Nafion (% w/v), and (d) time on the electrochemical detection of 10 μg mL$^{-1}$ vitamin D$_3$. Error bar: n = 3.

### 4.1.3.4.2 Effect of NaClO$_4$ concentration

The voltammetric responses of vitamin D in different concentrations of the supporting electrolyte (0.01 - 1 M of NaClO$_4$) were also recorded by adsorptive stripping square-wave voltammetry (AdSWV) (Figure 4.1.6b). The maximum peak current was observed at a concentration of 0.1 M, and then the current remained steady above that level. Usually, the concentration of a supporting electrolyte should at least be 1000 times greater than the concentration of the analyte to eliminate migration.

### 4.1.3.4.3 Effect of Nafion concentrations (%w/v)

To explore the best sensitivity of the fabricated electrode for detection of vitamin D, varying concentrations of Nafion for the composite electrode were investigated by AdSWV. Figure 4.1.6c shows the current response for different Nafion percentages. Within the studied range (0.01% to 0.5% w/v Nafion), the maximum $i_{pa}$ occurred at 0.1% w/v. However, lower current responses are observed when higher percentages of Nafion were used. The lower sensitivity is likely due to the hindered active surface area of graphene, which was extensively covered by Nafion. Additionally, an $i_{pa}$ of 0.01% Nafion was less than that of 0.1% probably because of the larger background current, which is almost identical to the graphene electrode. Therefore, the optimal level of Nafion was selected at 0.1% w/v for preparing the electrode ink.

### 4.1.3.4.4 Effect of equilibration time

Time is another important parameter that affects the electrochemical determination of fat-soluble vitamin D. It was found that as the equilibration time before the analysis increases, the peak current increases up to 5 min, and then slightly decreases (Figure 4.1.6d). As discussed earlier in section 3.3.3, the diffusion of the ethanol-solvated molecules to the electrode surface was much less efficient than that of the hydrated molecules [142]. Thus, enough time will facilitate the diffusion of the vitamin D molecules toward the electrode surface. However, long analysis time is undesirable. To avoid a long analytical period, 5 min was chosen as an optimal time for equilibration before the electrochemical analysis of vitamin D.

### 4.1.3.5 Electrode fouling effect from the analysis of vitamin D

To investigate the fouling effect in the detection of vitamin D, 10 µg mL$^{-1}$ vitamin $D_3$ in 60% v/v EtOH was consecutively analyzed using the same electrode with both graphene the and graphene/Nafion composite electrode. For comparison, the peak height of the first run in each case was normalized to 100%. As shown in Figure 4.1.7A, the normalized current of the consecutive run was significantly elevated with the graphene electrode (orange line), leading to a high error in the measurement. Therefore, the repetitive usage of the electrode is limited. Interestingly, a smaller fouling effect occurred with the graphene/Nafion electrode (blue line), which could be successively analyzed up to 10 times with a normalized current less than 105%. Note that a decrease in a surface area of the graphene/Nafion nanocomposite plays a key role in anti-adsorption on the electrode surface by preventing macromolecules from entering inside and blocking the adsorption of debris [143]. This comparison indicates that the graphene-Nafion nanocomposite offers an improvement in repeatability and robustness and is a good alternate for the continuous monitoring of vitamin D with no electrode fouling restrictions.
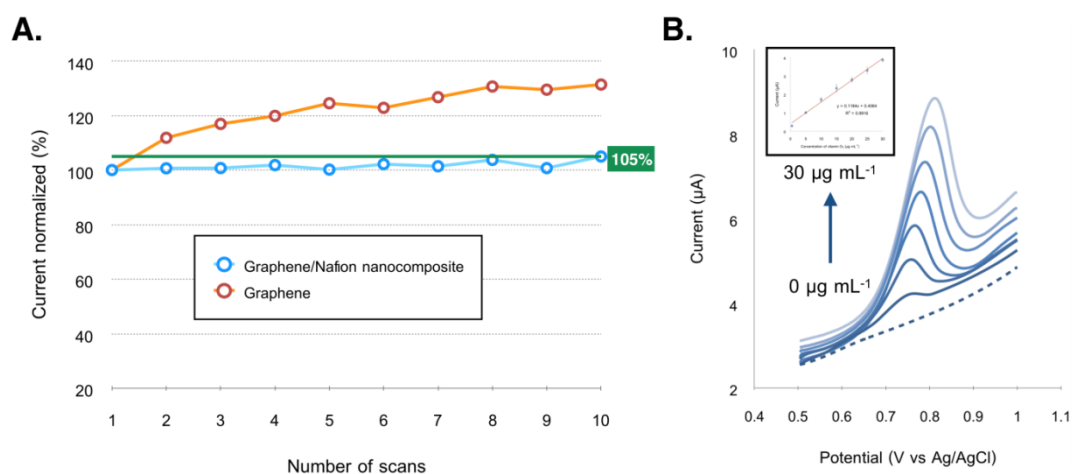
**Figure 4.1.7** (A) The plots between adSWV voltammetric normalized current of 10 µg mL$^{-1}$ vitamin D and number of successive usage of the graphene and graphene/Nafion nanocomposite electrodes. Note that the first peak current in each case has been normalized to 100%. (B) Square-wave voltammogram showing the electrochemical determination of vitamin D and the representative calibration graph (inset) between the oxidative peak current (µA) and concentration of vitamin D (0.5 - 30 µg mL$^{-1}$).

### 4.1.3.6 Analytical performance of the developed sensor for the vitamin D determination

The analytical performance of the graphene/Nafion nanocomposite electrode for the determination of vitamin D was evaluated with AdSWV under optimized conditions. Figure 4.1.7B shows the voltammograms together with a calibration curve (inset) as a function of vitamin D concentration. The sensor demonstrates an excellent linear relation in the range of 0.5-30 µg mL$^{-1}$ with a correlation coefficient of 0.9916. The limit of detection (LOD) and quantitation (LOQ) from the calculation are found to be 68.8 and 229.6 ng mL$^{-1}$, respectively. Furthermore, to evaluate the reproducibility with different graphene/Nafion composite electrodes (n=10) in terms of the relative standard deviation (%RSD), three concentrations of vitamin D were

utilized. The %RSD at each concentration was found to be less than 7%, suggesting a good reliability and reproducibility of the developed sensor for vitamin D detection.

The comparison of the analytical performance between the developed electrochemical sensors with previous works for vitamin D determination is presented in Table 4.1.2. A preferable linear range is achieved using the developed sensor while the LOD is on a level with other electrodes. To the best of our knowledge, a glassy carbon electrode (GCE) can be used to determine the amount of vitamin D, unfortunately, the use of this electrode can be tedious regarding the pretreatment/polishing step before and after use. This additional procedure is often not practical, especially when the disposable/semi-disposable electrode is expected. Generally, the use of GCE is suffered from the electrode fouling leading to an inconvenience for continuous detection. Besides, a further electrode modification is often required to enhance the sensitivity towards target analyte due to very slow electron transfer kinetics of its carbon-based material. However, reproducibility and complicated preparation are the general problems found from the modified electrode. To prove our concept for anti-fouling strategy, in this work, an electrochemical response for 10 consecutive analysis of vitamin D between using unpolished GCE and graphene/Nafion nanocomposite SPE was also compared. Interestingly, the surface fouling effect on GCE was substantially observed (up to 158%) and much larger than the graphene (up to 131%) and graphene/Nafion nanocomposite SPE (Figure 4.1.8). Hence, the cost-effective of the electrode, semi-disposable characteristic (disposable after 10 times usage) and the feasibility for mass production are the major roles for the selection of the screen-printed graphene/Nafion nanocomposite electrode to be the best sensor for vitamin D detection.

**Table 4.1.2** Comparison of this method for the determination of vitamin D with other electrodes.

| Electrodes | Linear range | | Detection limit | | Ref |
|---|---|---|---|---|---|
| | Vitamin $D_2$ ($\mu$g mL$^{-1}$) | Vitamin $D_3$ ($\mu$g mL$^{-1}$) | Vitamin $D_2$ ($\mu$g mL$^{-1}$) | Vitamin $D_3$ ($\mu$g mL$^{-1}$) | |
| Rotating GCE | - | 0.769-76.9 | - | 0.769 | [122] |
| GCE | 0.397-3.97 | 1.92-19.2 | 0.052 | 0.045 | [142] |
| GCE | - | 3.85-15.4 | - | 1.15 | [144] |
| SiO$_2$/GO/Ni(OH)$_2$/GCE | - | 0.096-0.962 | - | 0.001 | [145] |
| AuPd/GCE | 0.397-3.97 | 1.92-19.2 | 0.020 | 0.069 | [146] |
| Graphene-Nafion nanocomposite SPE | 0.5-30 | | 0.069 | | This work |
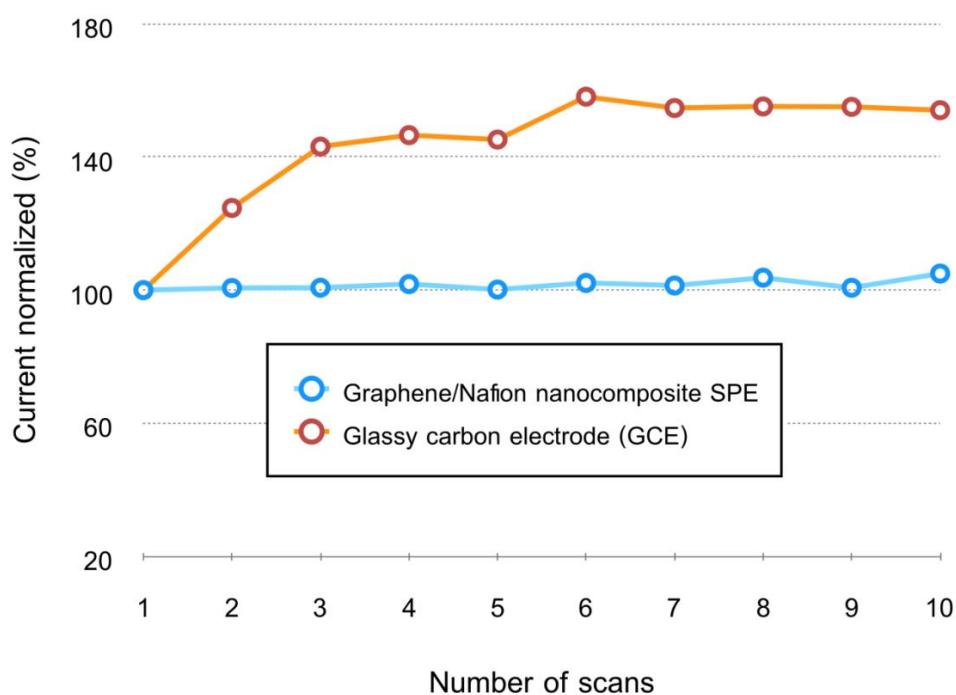
**Figure 4.1.8** The plots between AdSWV voltammetric normalized current of 10 µg mL$^{-1}$ vitamin D and number of successive usage of the GCE and graphene/Nafion nanocomposite electrode. Note that the first peak current in each case has been normalized to 100%.

**4.1.3.7 Selectivity and interference study**

The electrochemical behaviors of 10 µg mL$^{-1}$ vitamin D$_2$ and D$_3$ on graphene/Nafion SPE were initially compared by using AdSWV. Apparently, the voltammetric responses obtained from vitamin D$_2$ were almost identical to vitamin D$_3$ (Figure 4.1.9A). Furthermore, the AdSWV measurement conducted for a mixed solution of vitamin D$_2$ and vitamin D$_3$ (total concentration of 20 µg mL$^{-1}$) was unable to distinguish between the two compounds and resulted in one anodic peak. The similarity in the voltammetric behavior of D$_2$ and D$_3$ demonstrates that the electrode has the same sensitivity to each compound. The similar behavior could be explained

by the structural resemblance of vitamin $D_2$ and $D_3$, where the only difference is in the side chain of vitamin $D_2$, which contains a double bond between carbons 22 and 23 and a methyl group on carbon 24. Additionally, it was suggested in earlier studies that vitamin $D_2$ and $D_3$ were likely undergoing oxidation at the common site of the triene moiety in their structure [121, 123]. Thus, the total level of vitamin D was reported in this study.

Selectivity is another major concern in sensing. The electrochemical responses of the sensor toward fat-soluble vitamins (each concentration = 10 µg mL$^{-1}$), including vitamin A, E, and K was first tested. As shown in Figure 4.1.9B, four well-defined and separated peaks for vitamin K (0.05 V vs Ag/AgCl), vitamin E (0.6 V vs Ag/AgCl), vitamin D (0.85 V vs Ag/AgCl), and vitamin A (1.1 V vs Ag/AgCl) were simultaneously detected using the graphene/Nafion composite electrode. For the first time, all of the lipid-soluble vitamins could be identified by electrochemical detection without prior chromatographic separation. The exceptional electrochemical response allows the use of this electrode for the further analysis of a group of fat-soluble vitamins concurrently.

Additionally, the effect of the potential interferences with regard to the detection of vitamin D was further studied. Note that vitamin D alone is usually inadequate to prevent bone loss. Therefore, along with vitamin D, calcium is regularly added in most supplements to treat skeleton diseases efficiently. Apart from calcium, a myriad of substances was also taken into consideration for the interference study in the presence of 10 µg mL$^{-1}$ of vitamin D. The interference concentration was kept constant at 10 mg mL$^{-1}$ for vitamin $B_1$, vitamin $B_2$, $CaSO_4$, $MgSO_4$, $K_2SO_4$ and $Zn(NO_3)_2$ and 10 µg mL$^{-1}$ for vitamin A, E, and K. No interference significantly impeded the electrochemical detection of vitamin D (inset of Figure

4.1.9B). This result suggests that the proposed sensor can be applied to determine the vitamin D level in pharmaceutical drugs and supplements.
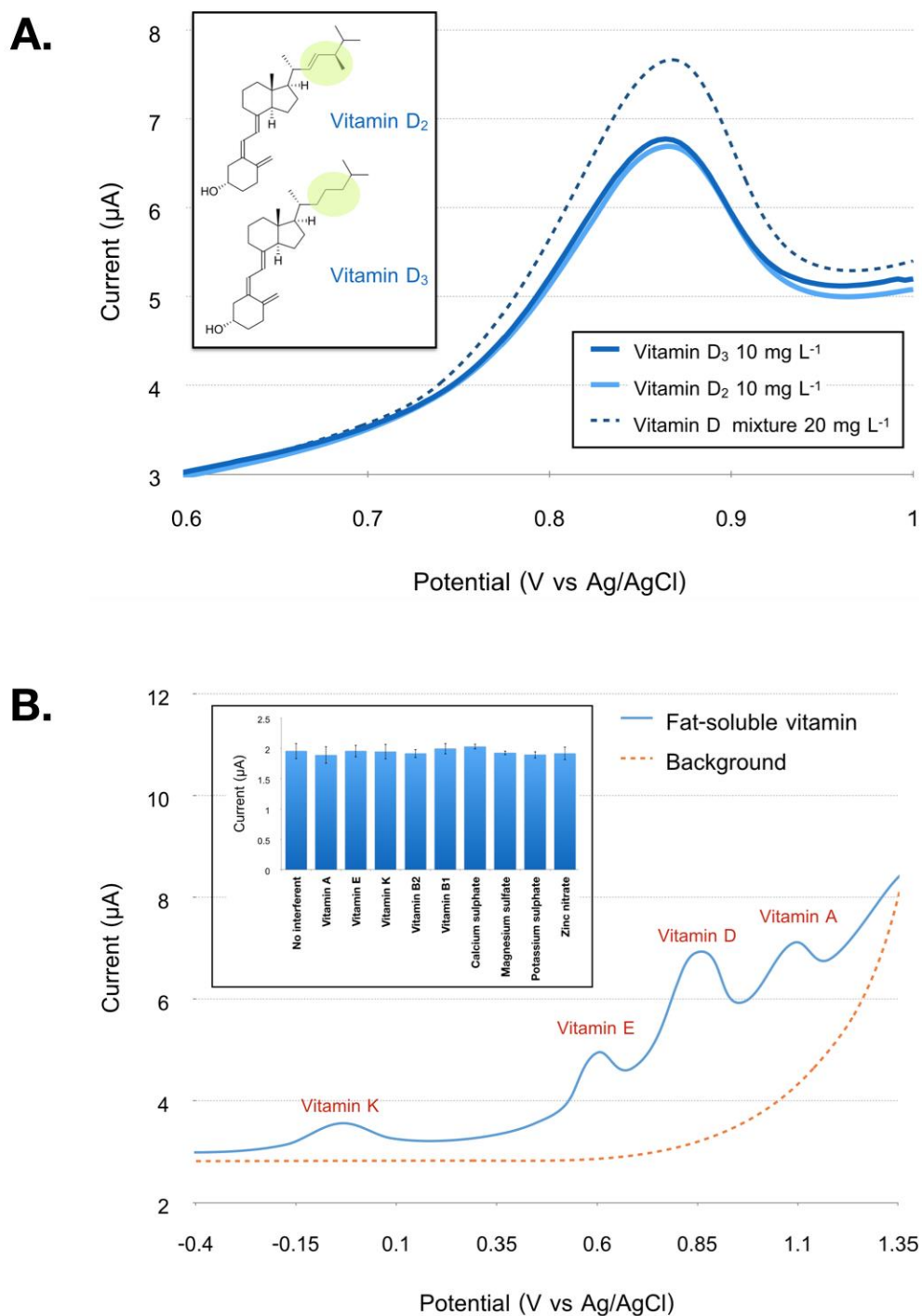
**Figure 4.1.9** (A) Cyclic voltammograms of vitamin $D_3$, vitamin $D_2$, and the mixture of vitamin $D_2$ and $D_3$. The potential sweep rate was 20 mV s$^{-1}$. (B) Square-wave voltammogram of the lipid-soluble mixture (A, D, E, and K), each at a concentration of 10 µg mL$^{-1}$. Inset: effect of the potential interferent (interferent

concentrations were kept constant at 10 mg mL$^{-1}$ for vitamin B$_1$, vitamin B$_2$, CaSO$_4$, MgSO$_4$, K$_2$SO$_4$ and Zn(NO$_3$)$_2$ and 10 µg mL$^{-1}$ for vitamin A, E, and K) on the electrochemical determination of 10 µg mL$^{-1}$ vitamin D$_3$.

### 4.1.3.8 Analysis of vitamin D in dietary supplements and pharmaceutical drug samples

To further evaluate the performance of the graphene/Nafion nanocomposite for the determination of vitamin D in real samples, several dietary supplements and pharmaceutical drugs that contained vitamin D in their composition were tested. Recovery tests were conducted by spiking the samples with vitamin D at concentration levels of 5, 10, and 20 µg mL$^{-1}$ and analyzing the samples according to the procedure described above. As listed in table 4.1.3, the obtained recoveries were in an acceptable range (100.4 - 107.1%), suggesting the proficiency of the method for the determination of vitamin D in such samples. In addition, the applicability of the developed method for the determination of vitamin D in actual samples was then verified with a standard LC-MS/MS method. A comparison of the analytical results between the two techniques is presented in Table 4.1.4. No statistically significant difference was observed (paired t-test at a 95% confidence interval provided *t* calculated (0.899) below *t* critical (3.182)), which demonstrates the applicability and reliability of this approach. Thus, the graphene/Nafion nanocomposite SPE can be successfully employed for the detection of vitamin D in real samples.

**Table 4.1.3** Recovery for the determination of vitamin D in real samples (n=3).

| Sample | Spiked concentration ($\mu$g mL$^{-1}$) | Found concentration ($\mu$g mL$^{-1}$) | %Recovery | %RSD |
|---|---|---|---|---|
| Sample 1 (Vitamin D$_3$) | 5 | 5.16 ± 0.29 | 103.2 | 5.72 |
| | 10 | 10.25 ± 0.41 | 102.5 | 4.01 |
| | 20 | 21.33 ± 1.26 | 106.6 | 5.90 |
| Sample 2 (Vitamin D$_3$) | 5 | 5.22 ± 0.31 | 104.4 | 5.90 |
| | 10 | 10.71 ± 0.41 | 107.1 | 3.85 |
| | 20 | 20.54 ± 0.71 | 102.7 | 3.45 |
| Sample 3 (Vitamin D$_3$) | 5 | 5.19 ± 0.18 | 103.8 | 3.49 |
| | 10 | 10.69 ± 0.19 | 106.9 | 1.76 |
| | 20 | 20.40 ± 0.78 | 101.1 | 3.81 |
| Sample 4 (Vitamin D$_2$) | 5 | 5.01 ± 0.28 | 100.4 | 5.68 |
| | 10 | 10.11 ± 0.39 | 101.1 | 3.90 |
| | 20 | 20.23 ± 0.55 | 101.2 | 2.70 |

**Table 4.1.4** The comparison of the proposed method and standard method for the determination of vitamin D in real samples (n=3).

| Sample | Labeled value (µg) per tablet | Vitamin D (µg) per tablet | | | |
| --- | --- | --- | --- | --- | --- |
| | | Proposed method | | LC-MS/MS | |
| | | found (µg) per tablet | %RSD | found (µg) per tablet | %RSD |
| Supplement 1 (Vitamin $D_3$) | 5 | 5.29 ± 0.27 | 5.18 | 4.84 ± 0.09 | 1.78 |
| Supplement 2 (Vitamin $D_3$) | 25 | 25.00 ± 1.10 | 4.41 | 25.13 ± 1.32 | 5.24 |
| Supplement 3 (Vitamin $D_3$) | 10 | 10.54 ± 0.19 | 1.79 | 10.96 ± 0.02 | 0.23 |
| Supplement 4 (Vitamin $D_2$) | 500 | 504.7 ± 4.52 | 0.90 | 501.2 ± 4.75 | 0.95 |

### 4.1.4 Conclusions

An electrochemical sensing of total vitamin D has been established. The electrochemical response of vitamin D on graphene/Nafion nanocomposite was superior over graphene and carbon electrode, attributing to the electron transfer ability of the grapheme material. Furthermore, the background current obtained from the combined materials exhibited the lowest background. The results from $C_{dl}$ assessment suggested that the lowest $C_{dl}$ value of graphene/Nafion nanocomposite was associated with the decrement in an active surface area, conceivably because of the partial coverage of graphene surface by the Nafion. This suggestion could be authenticated by the CV estimation of effective electrochemical active area and SEM images. With the synergistic effect of graphene nanomaterials and well-known properties of Nafion, a greatly amplified S/B was carried out. In addition, this graphene-based Nafion nanocomposite can effectively reduce electrode fouling effect from vitamin D analysis which limits practical application. Highly sensitive electroanalysis of vitamin $D_3$ and vitamin $D_2$ was also demonstrated, and the results were consistent with the standard LC-MS/MS method. The methodology showed a linear response for vitamin D in the range of 0.5-30 µg mL$^{-1}$ with the limit of detection (LOD) of 68.8 ng mL$^{-1}$. Therefore, this electrochemical sensing platform has a potential as a cheaper, faster analytical method for the direct determination of vitamin D, and group of lipid-soluble vitamins. In addition, this developed sensor could be a candidate for solving the problem from electrode fouling for other important compounds.

**Part II**

## 4.2 A 3D Capillary-Driven Paper-Based Sequential Microfluidic Device for Sensing Applications

Abdulhadee Yakoh[a], Sudkate Chaiyo[a], Weena Siangproh[b], Orawon Chailapakul[a]*

[a] Electrochemistry and Optical Spectroscopy Center of Excellence (EOSCE), Department of Chemistry, Faculty of Science, Chulalongkorn University, 254 Phayathai Road, Patumwan, Bangkok 10330, Thailand

[b] Department of Chemistry, Faculty of Science, Srinakharinwirot University, Sukhumvit 23, Wattana, Bangkok 10110, Thailand

* Corresponding author

## Abstract

This article describes the device design and fabrication of two different configurations (flow-through and stopped-flow) of a sequential fluid delivery platform on a microfluidic paper-based device. The developed device is capable of storing and transporting reagents sequentially to the detection channel without the need for external power. The device comprises two components: an origami folding paper (oPAD) and a movable reagent-stored pad (rPAD). This 3D capillary-driven device eliminates the undesirable procedure of multiple-step reagent manipulation in a complex assay. To demonstrate the scope of this approach, the device is used for electrochemical detection of biological species. Using a flow-through configuration, a self-calibration plot using a single buffer introduction is established for ascorbic acid detection. The effectiveness of the device was further broaden to a complex assay using a stopped-flow configuration. Unlike other electrochemical paper-based sensors in which the user is required to cut off the device before electrochemical measurement, herein, a stopped-flow device is carefully designed to exclude the disturbance from the convective mass transport. As a proof of concept, multiple procedures for electrode modification and voltammetric determination of serotonin are illustrated. In addition, the research includes an impedimetric label-free immunosensor for alpha-fetoprotein using the modified stopped-flow device. The beneficial advantages of simplicity, low sample volume (1 µL), and ability to perform a complex assay qualify this innovative device for use with diverse applications.

**Keywords:** Microfluidic paper-based device, Sequential fluid delivery, Folding paper, Sensing applications

### 4.2.1 Introduction

For decades, paper has been broadly used in analytical experiments, whether as a pH indicator (litmus), filter or substrate material. The distinguishing characteristics of paper (e.g., its high surface area of the fiber network and power-free fluid flow via capillary force) have enabled its use in myriad sensing applications ranging from a simple chemical sensor to clinical diagnosis with various detection techniques. In 2007, the term "microfluidics paper-based analytical device" or μPAD was first publicized by Martinez et al. and led to an influential change in the scientific community that has continued to date [147]. Although the capabilities of the μPAD have been greatly expanded, the limitations of a paper device remain a challenge. Typically, the potential of the μPAD is limited to a straightforward analysis. Immunoassay, for instance, demands multistep reagent introduction, washing (at least 3 times for each immobilization/blocking/conjugation) and a detection step that impedes μPAD to be used by the end-user. To avoid these challenges, substantial colorimetric sensors based on the enzyme-linked immunosorbent assay (ELISA) have been reported. Preechakasedkit recently described the use of an automated wax-printed paper-based lateral flow device for one-step ELISA [148]. Whiteside's group also reported a sliding strip microfluidics that enables ELISA on paper [149]. An electrochemical sensor for specific analytes (heavy metals and biological compounds) is also another example that requires multiple steps preparation. Several electrochemical biosensors often require an electrode-modifying agent (e.g., noble metal nanoparticles) to enhance the sensitivity of the sensor for such complex samples. However, an electrochemical modification of these noble metals cannot be accomplished directly on a regular paper device as a consequence of the remaining metal residue inside the porous structure of the cellulose paper. To avoid a washing step, previous studies have tended to fabricate folding papers containing an additional counter/reference (CE/RE) electrode that can be detached after

modification [150]. Nevertheless, steps for the reagent (noble metal solution), analyte introduction, and washing of a working electrode (WE) may be inevitable.

Herein, a new novel design: a 3D sequential microfluidic paper-based analytical device or sePAD that allows reagents to be stored in a movable reagent storage PAD (rPAD) and transported sequentially to the detection zone of origami PAD (oPAD) was engineered. Only a single introduction of a carrier buffer sufficiently runs a completed assay; therefore, little manipulation of solutions is needed by the user. In the present work, a sensitive electrochemical method was incorporated in a paper device. To demonstrate the capability of the device, a variety of biological sensing applications were applied and tested with the developed platform. For example, a straightforward flow-through design (Figure 4.2.1A) for amperometric ascorbic detection was illustrated in this work as a proof of concept, which enables an establishment of a self-calibration plot within a single device. In addition, the functionality of the sePADs for a multiple-step voltammetric serotonin (5-HT) sensor using a gold-modified electrode was demonstrated using one-step manipulation. This research also included a one-step label-free electrochemical impedance immunosensor for alpha-fetoprotein (AFP) detection. To perform an electrochemical measurement (e.g., voltammetry, electrochemical impedance spectroscopy), the disturbance of mass transfer induced by convection had to be eliminated. Hence, a stopped-flow wax barrier assembled in a simple oPAD was also designed to stop convection from fluid flow within the channel during the measurement (Figure 4.2.1B). Using the stopped-flow configuration coupled with a pullable rPAD, a time-controlled fluid flow could be precisely constrained. This novel platform served as an alternative analytical tool for the determination of a complex assay, for which an inexpensive and effortless system is particularly desired.
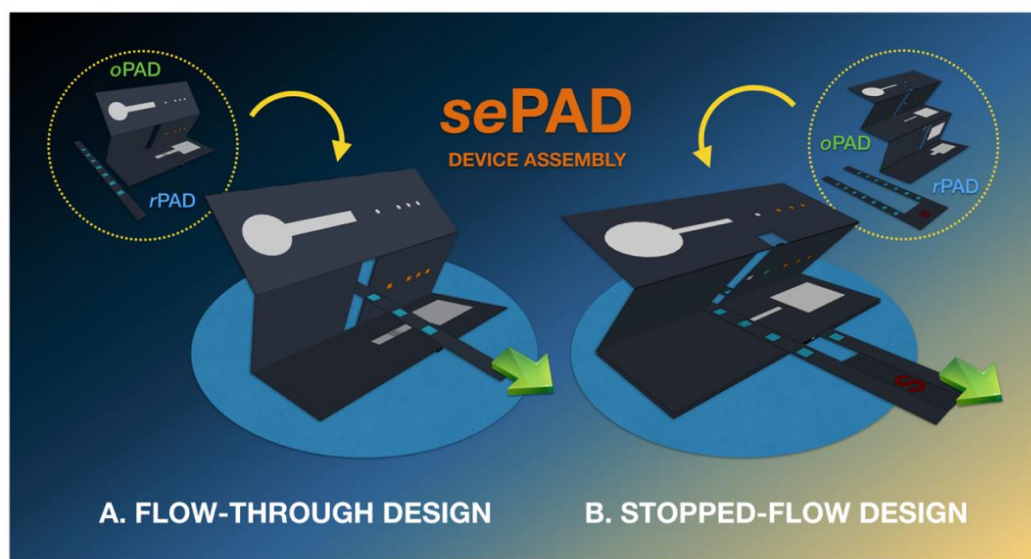
**Figure 4.2.1** Schematic illustration of the sePAD components and device assembly using A.) flow-through design and B.) stopped-flow design

### 4.2.2 Experimental

#### 4.2.2.1 Materials, equipment, and chemicals

All commercial reagents were of analytical grade and handled according to the material safety data sheets suggested by the suppliers. Phosphate buffered saline (PBS), potassium ferricyanide, casein, bovine serum albumin (BSA), 1-ethyl-3-(3-dimethylaminopropyl) carbodiimide (EDC), N-hydroxysulfosuccinimide (sulfo-NHS), creatine (CA), Tween 20 and Tris(hydroxymethyl) aminomethane were purchased from Sigma Aldrich (St. Louis, MO, USA). Ascorbic acid (AA), glucose anhydrous (Glc), sulfuric acid, sodium chloride, potassium chloride and potassium nitrate were purchased from Carlo Erba (Barcelona, Spain). Potassium tetrachloroaurate (III), uric acid (UA) were acquired from Wako (Japan). Alpha-fetoprotein (AFP) monoclonal antibodies (10–1391) were purchased from Fitzgerald (North Acton, MA, USA). A water-based dispersion of single layer GO sheets (5 mg mL$^{-1}$) was purchased from Angstron Materials (OH). A carbon/graphene paste, and Ag/AgCl ink was purchased from Gwent group/Sun Chemical (Pontypool, U.K.). All aqueous solutions were

freshly prepared in ultrapure water produced using a Milli-Q system (18.2 M$\Omega$ cm) purchased from Millipore. Whatman 1 chromatography paper was acquired from Fisher Scientific (PA). Wax printing was patterned with a Xerox ColorQube 8570 (CT) wax printer. SEM was performed using SEM-EDS (IT-500HR) (JEOL Ltd., Japan). Cross-sectional SEM and EDX analysis were performed by JSM-7610F field emission scanning electron microscope (FESEM) (JEOL Ltd., Japan).

### 4.2.2.2 Fabrication of the 3D sePAD

In all cases, the 3D sePAD comprised two main parts: a reagent PAD (rPAD) and a folding origami PAD (oPAD). All device designs (Figure 4.2.2 A-B) were created using Adobe Illustrator CC (Adobe Systems, USA). A wax-printing technique was used to create a wax barrier. The designed pattern was printed on Whatman grade 1 chromatography paper using a wax printer (Xerox ColorQube 8570, Japan) and then placed in an oven at 170°C for 1.5 min to melt the wax. Next, hollow channels were cut using a razor blade. Three electrodes were then screen-printed at the back of the detection zone of oPAD (unless state otherwise) via screen-printing technique (Figure 4.2.2 C-D) and dried at 65°C for 30 min. A double-sided tape was used to attach the back of the pipetted reservoir and working zone (3 electrodes). Blotting paper was attached at the bottom of the waste reservoir to accumulate excess solution. Alligator clips were used to connect the three electrodes to a potentiostat. Finally, the rPAD was placed in the folding paper of oPAD, and the assembled device was sandwiched between two acrylic plates and tighten with binder clips.
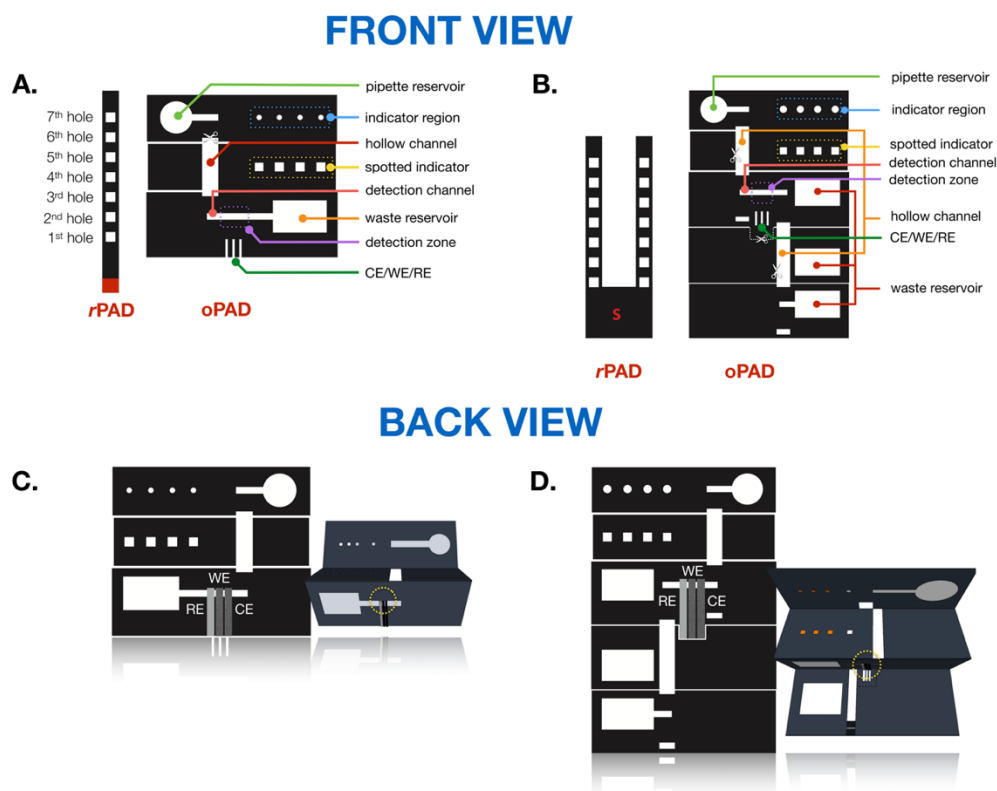
**Figure 4.2.2** Schematic illustration of the sePAD device configurations: front view and back view of the flow-through design (A and C) for AA detection and the stopped-flow design (B and D)) for 5-HT detection.

### 4.2.2.3 Sample and reagent spotting

In all cases, 1 µL of the sample/reagent solution was spotted in the storage hole of rPAD as shown in Figure 4.2.3. After reagent spotting, the rPAD was allowed to dry at room temperature (25℃). A dye solution of orange G (1 µL) was spotted in the indicator zones on the second layer of oPAD. The appearance of an orange dye flowing upward to the first layer indicated when the fluid passed across the detection zone. To enable an impedimetric AFP immunosensor, the AFP antibody was immobilized on the oPAD following a literature with a slight modification [151]. Briefly, 1 µL of GO solution (0.1 mg mL$^{-1}$) was deposited in a porous paper of a separated WE and allowed to dry. After washing with milliQ water, a carboxylic group

(−COOH) of GO was activated with EDC/NHS (30 mM, 5 µL) followed by coupling with the AFP antibody (1 mg mL$^{-1}$, 0.2 µL) for 1 hr. After a washing step with 0.01 M PBS (pH 7.4) containing 0.05% Tween 20, the working zone was blocked using the blocking buffer (100 mM Tris buffer (pH 9.2) with 1% (w/v) casein) for 1 hr and allowed to dry. At this point, the device was ready to use for the analysis.
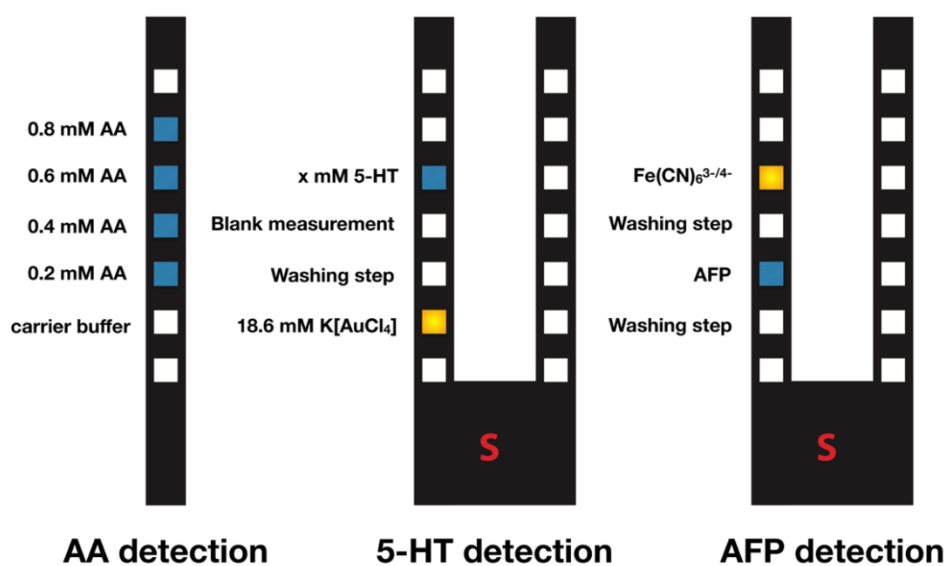


**Figure 4.2.3** Schematic illustration of the spotted reagents on rPAD for AA, 5-HT and AFP detection.

### 4.2.2.4 Electrochemical detection

Voltammetric and chronoamperometric experiments were performed with a model 1232A potentiostat (CH Instruments, Austin, TX). Electrochemical impedance spectroscopy (EIS) was performed with a PalmSens 4 potentiostat/impedance analyzer (PalmSens BV, Netherlands).

For AA detection using the flow-through design, 200 µL of 0.01 M PBS was used as a carrier buffer. After loading the carrier buffer, a chronoamperometry (potential of 0.3 V vs Ag/AgCl, sample interval of 0.1 s, and run time of 3000 s) was monitored after the orange indicator has appeared.

For 5-HT detection, 120 µL of 0.01 M PBS was used as a carrier buffer. Electrodeposition was used to prepare the modified electrode. A solution of 18.6 mM $K[AuCl_4]$ was eluted from the rPAD and flowed through the electrode while applying an accumulation potential of -0.5 V vs Ag/AgCl for 300 s. After modification, the electrode was then rinsed with a carrier buffer for 300 s through an empty hole of rPAD. Next, a solution of 5-HT was introduced to the detection channel for 60 s, and the wicking was then stopped by moving the rPAD to the wax barrier. A rest period was maintained for 120 s to allow the solution to reach steady state. Subsequently, differential-pulse voltammetry (DPV) was performed using a potential scan ranging between -0.1 to 0.5 V vs Ag/AgCl, an amplitude of 0.05 V vs Ag/AgCl, a potential increment of 4 mV, and a pulse width of 0.05 s.

For AFP immunosensor, 200 µL of 0.1 M $KNO_3$ was used as a carrier. AFP was allowed to wick across the electrode for 20 min to ensure the protein binding. Unbound AFP was further rinsed off through the vacant hole of rPAD for 10 min. For EIS measurement, a solution of 20 mM $Fe(CN)_6^{3-/4-}$ was introduced to the detection channel for 60 s. Afterward, the solution wicking was stopped and left in a rest step for 120 s before EIS analysis. EIS was recorded in the frequency range of 0.01 Hz – 300 kHz with the AC potential of 0.1 V.

### 4.2.3 Results and discussion

#### 4.2.3.1 Design and operation of the 3D sePAD

In this section, conceptual design and working operation of the sePAD are described. Basically, the device comprises two main components: a movable reagent storage pad (rPAD) to store and transfer reagents and a folding origami paper (oPAD) for electrochemical measurement. Once assembled, a loading carrier buffer continually elutes a prior-deposited reagent from rPAD to the detection channel of oPAD. Two different sePAD configurations, flow-through and stopped-flow, were designed for different sensing purposes. In particular, the flow-through architecture was developed for continuous flow electrochemical measurements such as chronoamperometry, whereas the stopped-flow architecture was developed for nonconvective electrochemical measurements such as voltammetry.

Beginning with the flow-through design, the first hole of the rPAD is aligned at a starting position and marked as a guide for the next hole (Figure 4.2.4A). In this position, the tip of the inlet channel (layer 1 of oPAD) faces the underlying layer of the second hole of rPAD. Therefore, a carrier buffer coming from inlet elutes a stored solution in the second hole of rPAD to the subsequent layer of oPAD (detection channel in layer 3 of oPAD). After the carrier buffer is loaded, the stored solution moves across a detection zone and passes through the first indicator spot to the waste reservoir. The appearance of an orange color in the first spot of indicator region (layer 1 of oPAD) caused by the upward flow from detection channel indicates that the solution has already passed over a detection zone and is ready for electrochemical measurement (Figure 4.2.4B). In addition, the capacity of the waste reservoir can be monitored from the orange color dot appeared in the second to fourth spot of indicator region (layer 1 of oPAD). Using this automated indicator, an external timer and potential error from assay timing are eliminated [152]. A blotting paper was attached at the bottom of the waste reservoir to collect excess liquid and

provide a capillary-driven flow of liquid.[149] When the time-controlled reaction is completed, the stored solution from the third hole in rPAD is subsequently introduced to the detection channel by pulling the rPAD to the next position. A similar step is applied to all the stored solution.
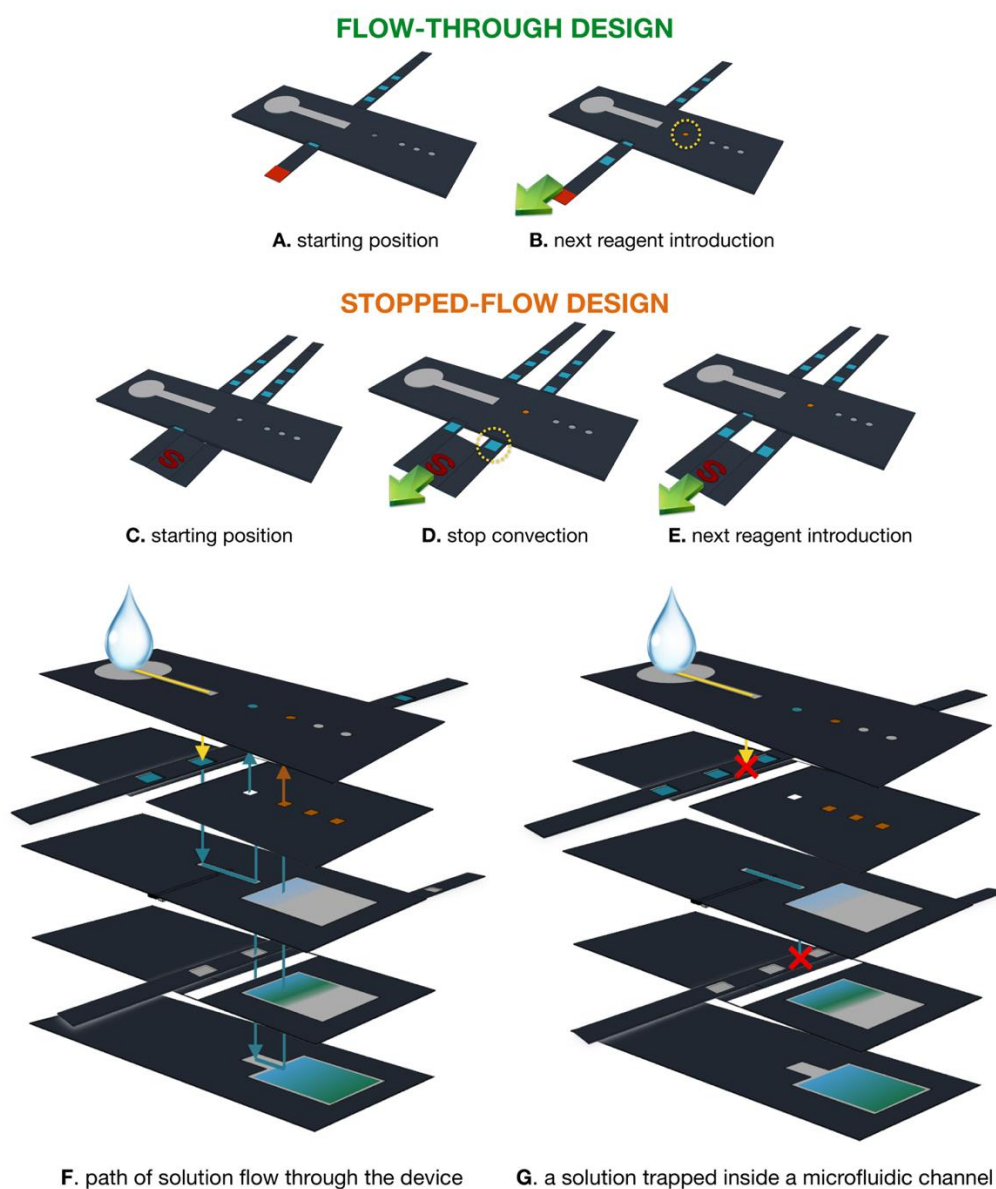


**Figure 4.2.4** Operation of the 3D sePAD using flow-through (A-B) and stopped-flow configuration (C-E). Components of the sePAD illustrating the path of the solution flow inside the channel: (F) before and (G) after stop flow.

A similar working principle was operated to a stopped-flow design (Figure 4.2.4 C, D and E). The path of solution flow throughout the device is schematically illustrated in Figure 4.2.4F. However, to stop convection from fluid flow, the movable rPAD is pulled to a position where a wax barrier (between each hole of rPAD) was vertically aligned to the inlet reservoir (Figure 4.2.4G). An exact position can be obtained from the border of the previous hole (see Figure 4.2.4D). With this alignment, a carrier buffer from the pipette reservoir cannot pass through the blocking layer of the wax barrier of rPAD. A related point to consider is the pattern design of the oPAD and rPAD. To confine a liquid inside the channel, wax barrier gates are required for both ends of the detection channel. Therefore, a pair of controllable gates was implemented on this platform to facilitate solution retention (Figure 4.2.4G). A photograph of the corresponding device after solution flow are shown in Figure 4.2.5A. After loading 120 μL of carrier solution (milliQ water), a solution moved from the pipette reservoir to the waste reservoir via capillary-driven force. Once the carrier passed through a detection channel, the upward flow of the solution toward indicator zone quickly wetted the prespotted dye and diffused to the indicator region in the layer 1. On the other hand, when the rPAD was pulled to a wax barrier position, a liquid can be trapped inside the detection channel and cannot flow to the waste reservoir. In addition, diffusion of the spotted-dye within the detection channel, once it was blocked, was observed in this study (Figure 4.2.5B). Therefore, to avoid possible interference in the electrochemical measurement from the spotted dye, the first indicator spot was left empty in the stopped-flow pattern. Despite this step, liquid flow is still detectable in the first indicator spot as soon as the liquid dampens a paper. Moreover, as a demonstration of the principle of the sePAD, different color dyes (spotted in the rPAD) representing

different storage reagents were consecutively introduced into the detection channel lacking prespotted indicator. The final device image depicted in Figure 4.2.6 illustrate that the stored dyes were visibly eluted from the rPAD to the detection channel and washed out to the waste reservoir. This result verifies the functionality of the device.
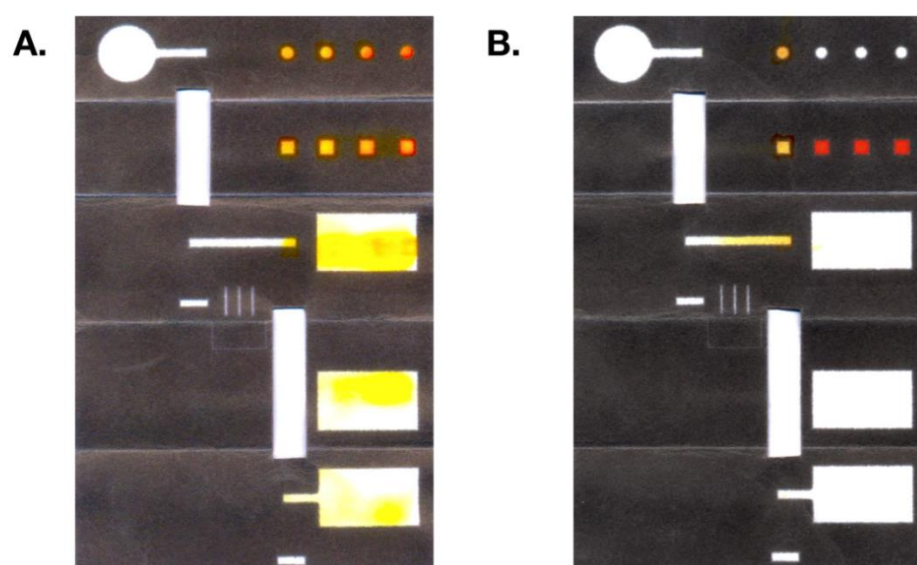


**Figure 4.2.5** A) Image showing the carrier flow into the waste reservoir and diffusion to the spotted indicator. B) Corresponding image device after the solution flow stopped.
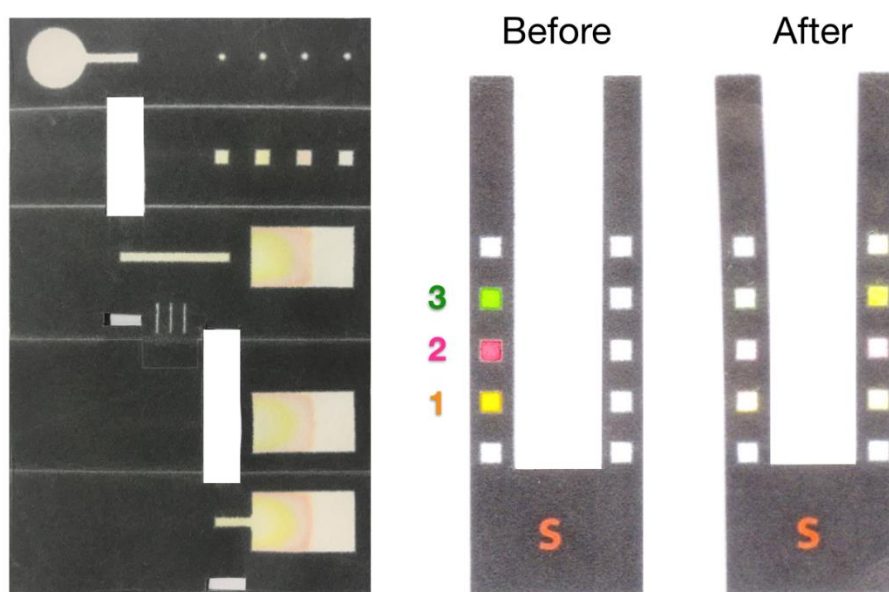
**Figure 4.2.6** Solution flow in the oPAD using different spotted color dyes.

For further use in immunoassay application, the alignment of the WE in the stopped-flow sePAD is altered. In most cases, the antibody (Ab) immobilization on a paper device was done on the nitrocellulose (NC) as antibody spontaneously immobilized onto NC via hydrophobic and electrostatic interaction [153]. However, Ab could not be directly immobilized on a regular Whatman paper. Therefore, graphene oxide (GO) drop-casted on paper was employed in this work as an immobilizing substrate. GO, a well-publicized precursor of graphene, has gained attention in the past few years, as it exhibits great potential for use in biosensing applications [154-157]. In the present work, the carboxylic (-COOH) termination of oxygen-containing functional groups of GO was activated and served as an active site to immobilize Ab through EDC/NHS chemistry. To define a working zone and control the dispersion of GO in a finite area, a separated working zone in parallel with a detection channel was designed in the second layer of the oPAD (see Figure 4.2.7 A

and B). The back of this isolated zone was screen-printed with carbon/graphene ink as WE. In this aspect, a small slit in the detection channel was trimmed to ensure that all the liquid flowing would pass through the immobilized Ab in the separated WE after the device was folded. Further characterization is discussed in Section 4.2.3.4.
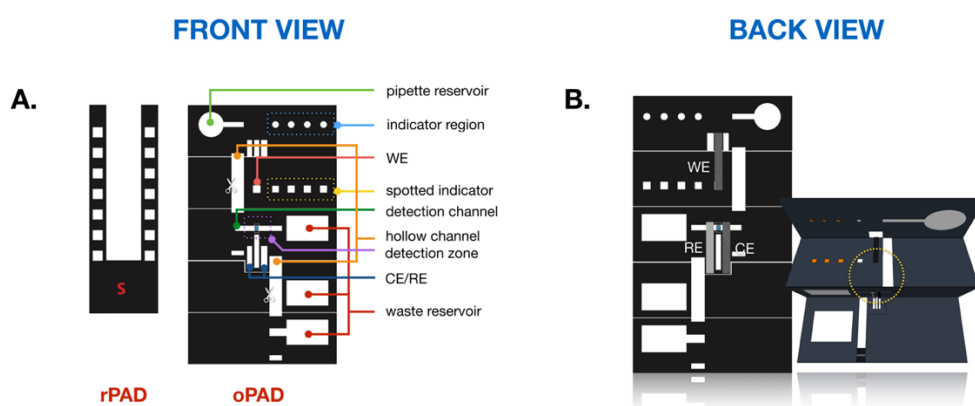


**Figure 4.2.7** Schematic illustration of the modified stopped-flow device for immunoassay application: A) front view and B) back view of the device.

### 4.2.3.2 Electrochemical detection of ascorbic Acid (AA) using flow-through sePAD

As proof of the concept, chronoamperometry (CA) for AA detection was performed using flow-through sePAD to demonstrate the electroanalytical applicability of the device. AA was chosen as a model analyte in this work due to its biological importance for humans and because sensitive determination methods for this biomarker are in demand. First, the influence of device geometry on the electrochemical response was studied by varying the channel width (1 and 2 mm), as illustrated in Figure 4.2.8A. The channel width was defined after the wax melting step. In this study, a larger channel width would provide a larger electrode area, thus leading to a higher electrochemical signal (Figure 4.2.8B). However, a narrower

channel width yields a faster flow velocity. Hence, a shorter recovery time (defined as the time required to recover up to 90% of the initial baseline) for the channel width of 1 mm is observed (250 s for 1 mm width and 505 s for 2 mm width). Additionally, the charge density ($\mu C\ mm^{-2}$) is greatly enhanced using a smaller width (2.50 $\mu C\ mm^{-2}$ for 1 mm width and 1.29 $\mu C\ mm^{-2}$ for 2 mm width). For this reason, a channel width of 1 mm was selected in this study to ensure a faster analysis time. Different concentrations of AA ranging from 0.2 to 0.8 mM were also tested using sePAD with a flow-through configuration. With a single introduction of a running buffer (PBS), a chronoamperogram for multiple AA concentrations (with unknown sample for real sample analysis) was obtained as shown in Figure 4.2.8C. In addition, the anodic peak current increased linearly with increasing AA concentration. The corresponding calibration curve for AA determination from 3 different devices is displayed in Figure 4.2.8D. To demonstrate the reproducibility of the device, triplicate introduction of 0.4 mM AA within the same device was performed. The relative standard deviation (RSD) was found to be less than 7.7%, indicating satisfactory precision and promising applicability of the device for the quantification of AA.
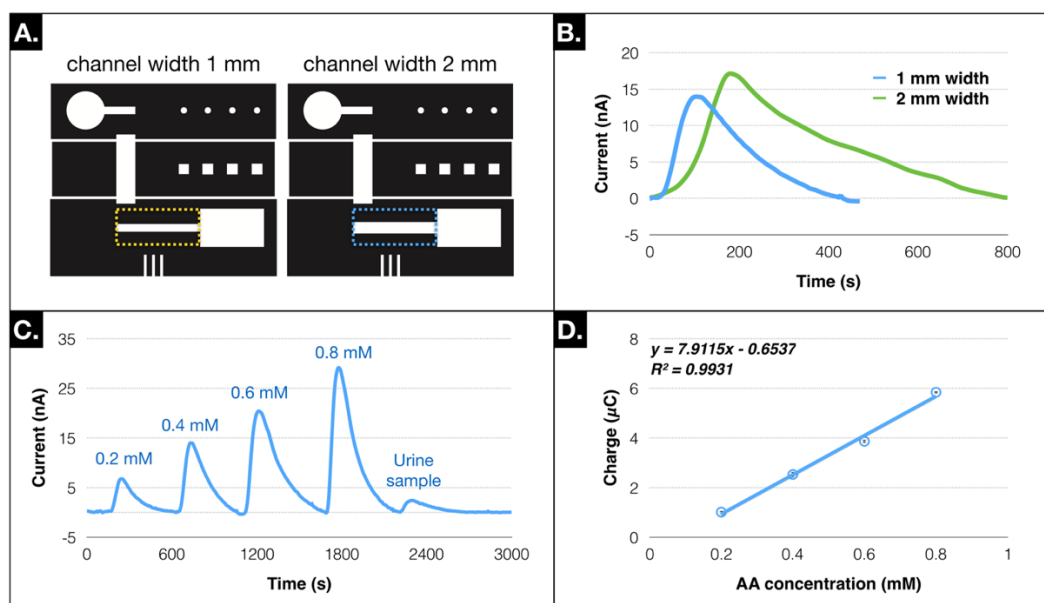
**Figure 4.2.8** A) Schematic illustration of the flow-through sePAD with different channel widths. B) Amperograms of AA as a function of channel width. C) One-step detection of AA in the concentration range of 0.2 to 0.8 mM and tested sample. D) Corresponding linear calibration plot of peak current as a function of AA concentration.

To further assess the selectivity of the method, possible interferences at normal concentrations found in the samples (urine: uric acid, creatinine, NaCl, KCl; and vitamin C beverage: glucose) were examined individually. The results showed that the normalized charge of uric acid was found to be less than 12% relative to AA while no signal was observed from other compounds (figure 4.2.9 A and B). To demonstrate the device applicability, the flow-through sePAD was used to detect AA in an artificial urine sample (Carolina Biological Supply Company, USA) and a vitamin C commercial beverage bought from the local market (Bangkok, Thailand). The test was conducted by spiking known concentration of an AA (0.1135 mM) into an artificial urine sample. For vitamin C beverage sample, the result was compared with the label value on the bottle of the beverage. The percentage of recoveries for all

samples were found in the range of 98.8% to 106 % and %RSD (n=3) was below 6.1%. These findings illustrate that the developed flow-through sePAD has a great promising to use in the real-world sample. Although the total analysis time for AA determination using this developed platform is extended relative to other AA sensors, excellent benefits such as low sample volume usage (only 1 μL for each rPAD hole), self-calibration establishment, and one-step detection without a required washing procedure make the platform feasible to use for electroanalysis applications.
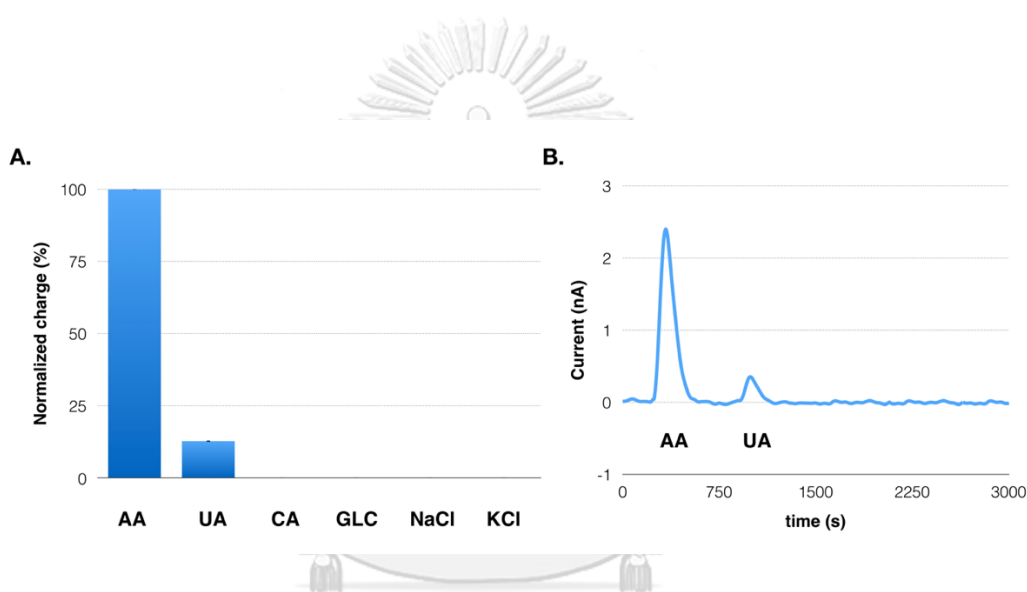


**Figure 4.2.9** The plot of the normalized charge (A) and the amperogram (B) for AA (0.11 mM), UA (0.20 mM), CA (5.92 mM), Glc (50 mM), NaCl (32 mM) and KCl (10 mM) tested with flow-through sePAD.

### 4.2.3.3 Electrochemical characterization of the stopped-flow sePAD and detection of serotonin (5-HT) by a gold-modified electrode

Principally, the mass transfer to an electrode plays a large role in electrochemical dynamics, as mediated by the Nernst-Planck equation [158]. Mass transfer, that is, the movement of the material from one location in solution to another, arises either from differences in electrical or chemical potential at the two locations or from the movement of a volume element of the solution. Theoretically,

there are three mechanisms of mass transfer: i) diffusion, ii) migration and iii) convection [159]. In practice, the electrochemical experiment is specifically designed to eliminate the contributions of migration and convection and limits the mass transfer to the contribution of diffusion. This controlling experiment can be achieved by the addition of an inert electrolyte (a supporting electrolyte) at a concentration much larger than that of the electroactive species (100-1000-fold) to reduce the effect from migration. In addition, the convection component (e.g., laminar flow or turbulent flow) can be prevented by avoiding stirring and vibrations in the electrochemical cell. Herein, the stopped-flow designed was specifically fabricated to prevent convection in the porous media of the paper. To confirm the functionality and applicability of the device to control a flow of solution in electrochemical measurement, a cyclic voltammetry experiment of an electroactive species ($Fe(CN)_6^{3-/4-}$) was conducted on a stopped-flow device. Because the flow in the paper channel followed Lucas–Washburn theory, the rate of flow ultimately approached zero [160]. Thus, to avoid a different wicking rate over time within a single device, two independent stopped-flow devices were used for the cyclic voltammetry measurement in the presence and absence of convection (flow-through and stopped-flow). From the cyclic voltammograms shown in Figure 4.2.10, the electrochemical behavior of $Fe(CN)_6^{3-/4-}$ performed on a device with and without convection can be discriminated. Under the same applied conditions, the CV curve in the presence of convection (Figure 4.2.10A) exhibited approximately steady-state behavior. With an enhancement in the mass transfer rate generated by the fluid motion, the peak shape of $Fe(CN)_6^{3-/4-}$ changed from the usual behavior in quiescent solution to a convective diffusion, yielding a higher current and almost reaching the plateau state. However, the current magnitude from 5 continuous cycles was gradually reduced, which could be ascribed to the nonlinear decreasing of wicking rate over time/distance in a paper [152]. On the other hand, as illustrated in Figure

4.2.10B, the magnitude of current in absence of convection was much smaller than in the convective system due to a limited mass transfer of diffusion. Interestingly, it can be clearly observed from 5 continuous cycles of CV that more reproducibility was attained when the fluid motion was stopped. Accordingly, it could be deduced that the stopped-flow sePAD offers an excellent capability for an electrochemical measurement in a quiescent solution.

จุฬาลงกรณ์มหาวิทยาลัย
CHULALONGKORN UNIVERSITY
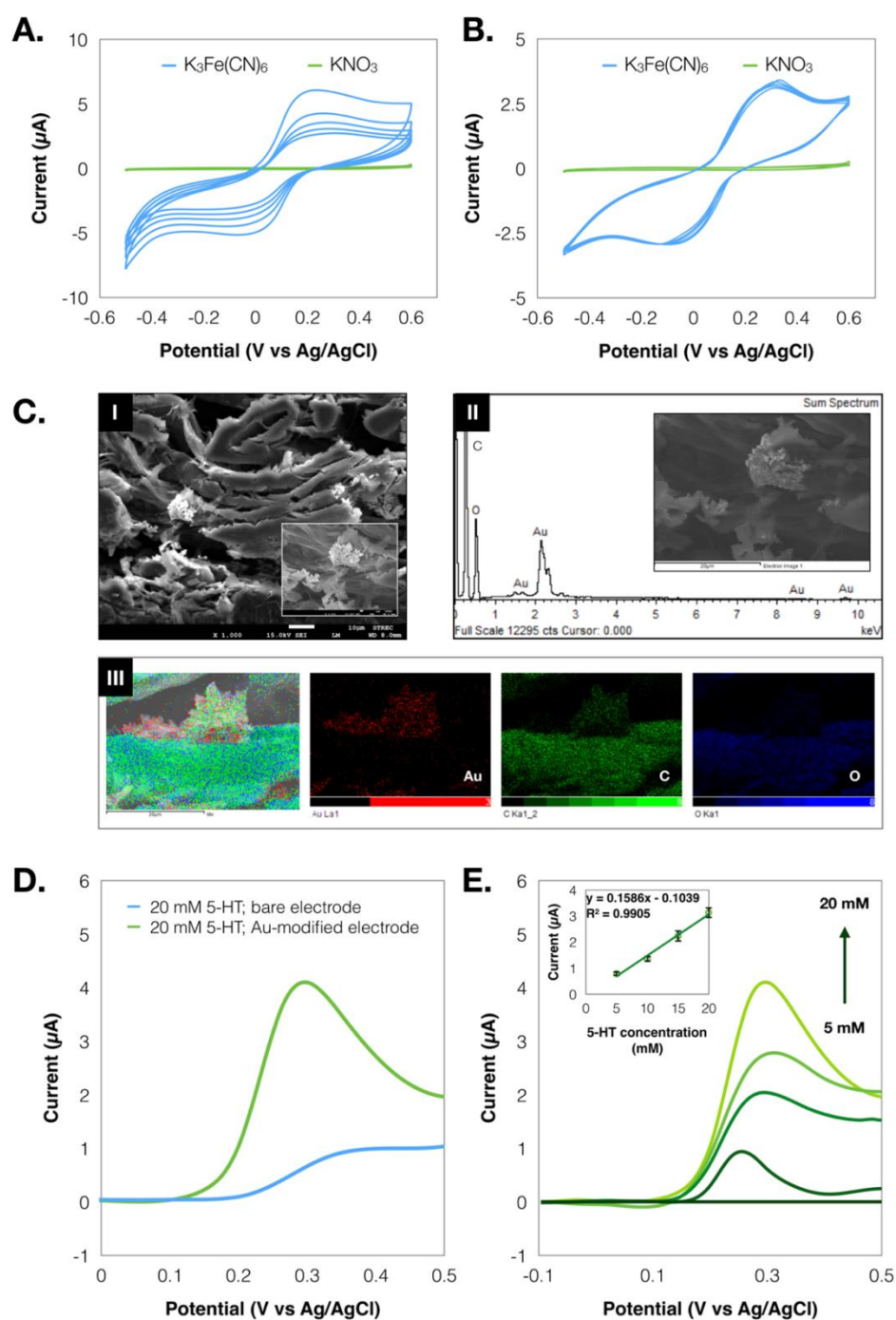
**Figure 4.2.10** CVs of the Fe(CN)$_6^{3-/4-}$ in the presence (A) and absence (B) of convection. C) Cross-sectional SEM image (I), corresponding EDX spectra (II) and elemental mapping (III) of the electrodeposited gold particles on a microfluidic paper-based device. D) DPVs for 20 mM 5-HT, at a bare, and Au-modified electrode.

E) DPVs of 5-HT from 5 to 20 mM and corresponding calibration curve (inset), at the modified electrode using stopped-flow sePAD.

To demonstrate the scope of a stopped-flow sePAD in practical application, the vital neurotransmitter serotonin (5-hydroxy-DL-tryptophan, 5-HT) was chosen as a model compound for a differential-pulse voltammetric (DPV) analysis. It has been reported that an inadequate level of 5-HT can cause certain types of depression [161, 162]. Thus, several electrochemical methodologies have been established for sensitive 5-HT detection. One area of interest within this broad method is an electrodeposition of the electrode-modifying agent such as gold nanoparticles (AuNPs) [163]. In this application, multiple procedures for electrode preparation (Au electrodeposition), washing and determination are enabled within the single device by a single running buffer introduction. Successful fabrication of the electrodeposited Au on a porous network of the paper WE could be confirmed by the cross-sectional SEM images. As depicted in a panel I of Figure 4.210C, after 5 min of Au electrodeposition, Au particles were found distributed on the surface of cellulose fibers near WE. SEM/energy dispersive X-ray (EDX) analysis was also performed to analyze elemental constituents. The presence of Au from EDX spectra and corresponding EDX mapping displayed in panel II and III of Figure 4.2.10C could verify the electrodeposition process using the developed sequential introduction platform.

Figure 4.2.10D shows a DPV for 20 mM 5-HT at a bare electrode (▬) and Au-modified electrode (▬). A distinct oxidation peak of 5-HT appeared at approximately 0.3 V vs Ag/AgCl. However, a substantial decrease in the peak current with a slight shift in peak potential toward a positive direction was obtained using an unmodified electrode. Similar trends were clearly observed using a freestanding commercial screen-printed electrode (Figure 4.2.11). These results confirmed the successful

electrodeposition of AuNPS using the sePAD platform. Next, the DPV measurement was employed for the determination of 5-HT. As illustrated in Figure 4.2.10E, the peak current is proportionally increased to the increasing concentration of 5-HT in the studied range of 5 to 20 mM with a correlation coefficient ($R^2$) of 0.99. In sum, these results indicate that the sePAD has practical potential as an outstanding platform for multiple-step voltammetric determination.
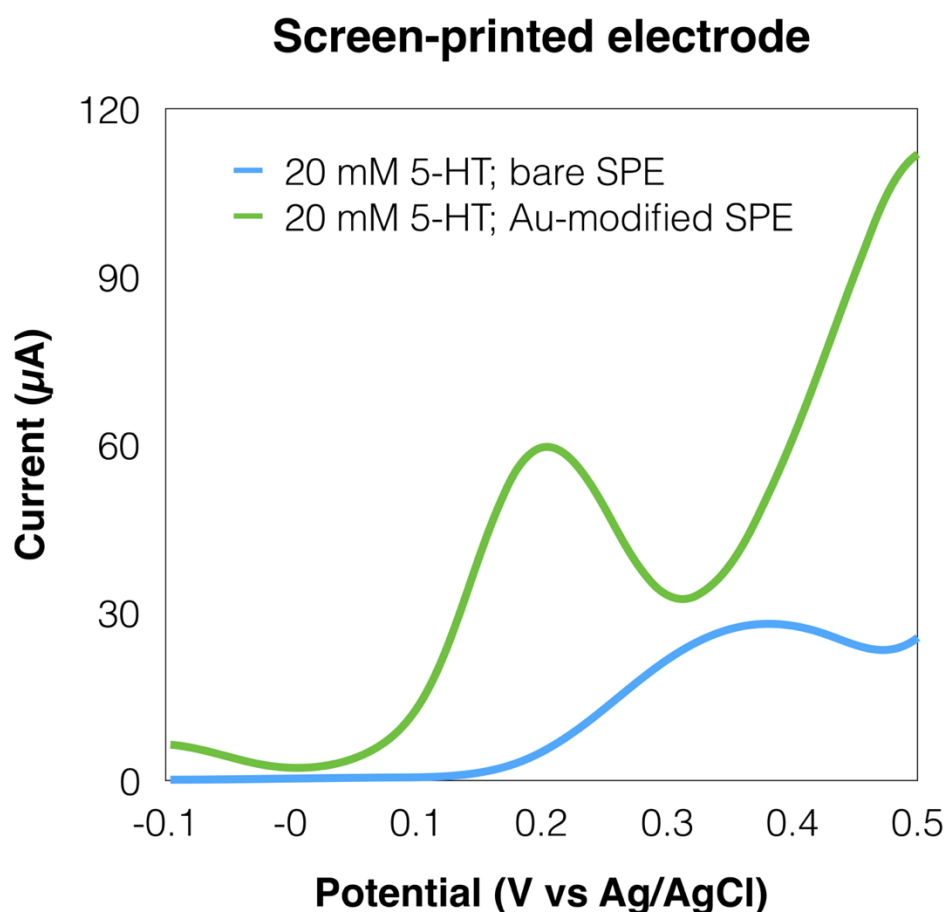


**Figure 4.2.11** DPVs for 20 mM 5-HT using freestanding screen-printed electrode: bare and Au-modified electrode.

### 4.2.3.4 Impedimetric label-free AFP immunosensor

In this application, alpha-fetoprotein (AFP), a well-known tumor marker for various cancerous diseases, was chosen as the analyte of interest to demonstrate the potential of the sePAD for a complex analysis. The abnormally elevated levels of AFP (<25 ng mL$^{-1}$ for healthy human and >25 ng mL$^{-1}$ for abnormal patients) may indicate increased risk for a yolk sac tumor or for liver, hepatocellular, testicular or nasopharyngeal cancer [148, 164, 165].

As previously mentioned, the stopped-flow configuration was designed specifically for the electroimmunoassay application. First, the effect of the device geometry toward flow velocity was studied. In this study, the flow velocity was calculated by monitoring the time for the fluid (120 μL milliQ water) to traverse across a straight channel until it reached the first spotted-indicator (orange color). It was found that the sePAD without separated WE exhibited a flow velocity of 0.035 cm s$^{-1}$. Nonetheless, with separated WE, the flow velocity was found to be 0.029 and 0.02 cm s$^{-1}$ for the unmodified paper and GO-modified paper, respectively. This prolonged velocity was ascribed to the device geometry of the overlapped channel and the accumulation of the GO nanosheet inside the porous structure which may obstruct the solution flowing.

SEM and EIS techniques were used to characterize the fabrication of the sensor. First, the morphology of the drop-casted GO on a paper was characterized by SEM technique. As depicted in Figure 4.2.12A, an unmodified paper displayed a fiber network of cellulose (panel I), whereas the GO nanosheet of GO-modified paper was overspread in the structure of a paper (panel II). Each fabrication procedure was also characterized by an EIS technique in the presence of the Fe(CN)$_6^{3-/4-}$ as a redox probe. In the biosensing field, EIS has been broadly used to detect the binding event of biomolecules occurring at the electrode-electrolyte interface onto the surface of

the sensor due to its capability to discriminate a small change on the surface [166, 167]. The EIS Nyquist plot is presented in Figure 4.2.12B. As depicted in panel I, the small $R_{ct}$ of a bare electrode indicates that the redox probe does not face any obstruction. When the electrode was drop-casted with GO, the $R_{ct}$ value is increased (Figure 4.2.12B panel II). This result suggests that GO acted as an insulating layer that hindered interfacial electron transfer due to the disrupted $sp^2$ bonding networks [168]. Once the Ab is immobilized onto the GO nanosheet through EDC/NHS chemistry (Figure 4.2.12B panel III), the continued increase of the $R_{ct}$ is observed, indicating a successful immobilization of the AFP antibody that acts as an electrochemical barrier between the electrode surface and redox probe. The blocking effect of casein is clearly indicated by an increase of the $R_{ct}$ (Figure 4.2.12B panel IV). This effect can be attributed to the protein immobilized on the electrode surface forbids the mass transfer of the redox mediator [169]. For AFP conjugation, this device design enables the continuous wicking of AFP across the electrode and facilitates the conjugation between antigen-antibody. After incubation with an AFP, the conjugation of an antigen-antibody exhibits a substantial obstacle to the redox probe (Figure 4.2.12B panel V). In this present work, the impedance spectra of the $Fe(CN)_6^{3-/4-}$ were modeled using the equivalent circuit of the Randles model modified with Warburg impedance (Figure 4.2.12B, VI).
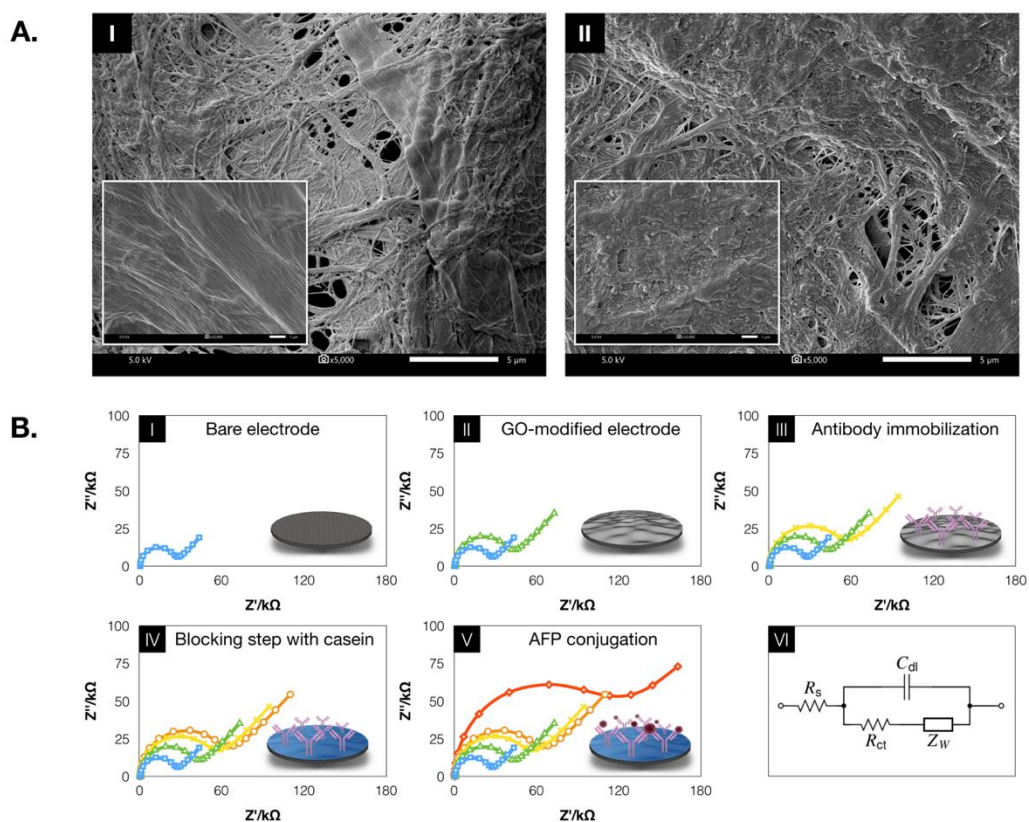
**Figure 4.2.12** A) SEM images of the unmodified (I) and GO-deposited (II) on a paper device. B) EIS characterization of the bare electrode (I) and after drop-casted with GO (II), antibody immobilization (III), blocking step with casein (IV) and 100 ng mL$^{-1}$ AFP conjugation (V). Equivalent circuit of the prepared electrode (VI).

As proof of the concept, the analytical performance of the developed paper device was concisely evaluated. The Nyquist plot of the faradaic impedance spectra with varied concentration of AFP is displayed in Figure 4.2.13A. The semicircles are gradually extended, as increasing the concentration of AFP. The dependence of the $R_{ct}$ on the concentration of AFP was also presented in Figure 4.2.13B. For a quantitative analysis, a linear calibration between $R_{ct}$ value and logarithmic concentration of AFP was established in the range of 10 to 100 ng mL$^{-1}$ with a regression coefficient of 0.9903. The small error bars of the standard deviations using

three intradevices demonstrated an excellent reproducibility of the method. These results indicate that the developed sePAD shows great promise for use in POC applications.
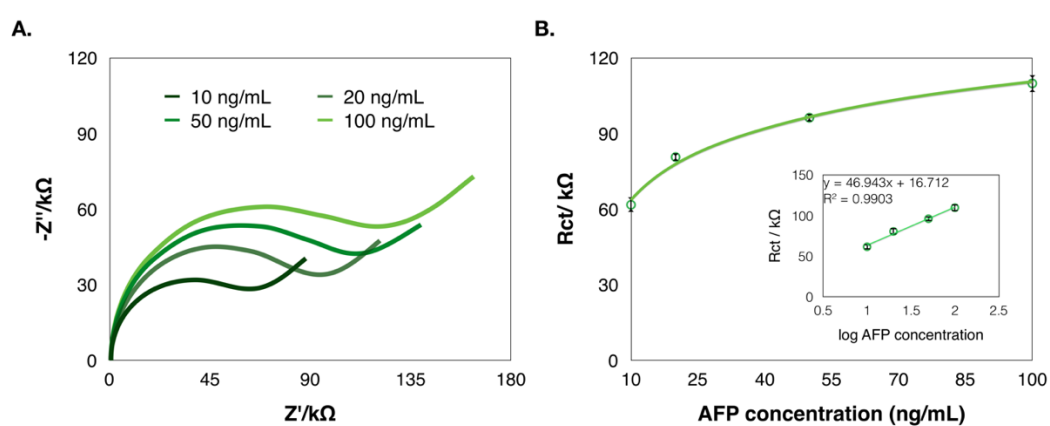


**Figure 4.2.13** A) Nyquist plots for the sePAD immunosensor at different AFP concentrations (10 to 100 ng mL$^{-1}$). B) Plot between $R_{ct}$ value and AFP concentrations and inset showing a linear calibration curve plotted between the $R_{ct}$ values vs logarithmic concentration of AFP in the range of 10 to 100 ng mL$^{-1}$.

### 4.2.4 Conclusions

In summary, a new class of microfluidic devices for electrochemical determination is reported. In this regard, the sequence of analytes/reagents is delivered to the detection channel through a reagent storage pad without the need for reagents manipulation by the users. Two different architectures of a sequential microfluidic platform; flow-through and stopped-flow; are designed specifically for different functions. As a demonstration, a completed calibration plot of amperometric ascorbic acid determination is simply established with a flow-through format using one-step buffer introduction. In addition, for the first time, a stopped-flow format is employed in the µPAD for sequential electrochemical deposition of the gold-modified electrode and differential-pulse voltammetric determination of serotonin. Benefitting from this architecture, the convective flow of the solution inside the porous structure of cellulose can be controlled, enabling an electrochemical measurement in a quiet solution. This innovative platform can also be applied to an impedimetric immunosensor of an alpha-fetoprotein detection. The sequential microfluidic device demonstrated here can be easily fabricated and extended to a range of a complex assay with the favorable advantages of an inexpensive and effortless platform, allowing use by end users.

# CHAPTER V
# CONCLUSIONS AND FUTURE PERSPECTIVE

## 5.1 Conclusions

The aim of this dissertation has been to develop miniaturized platforms for analytical sensing applications and improve the performance of the devices by integrating excellent properties of the nanomaterials. The results apparently indicated that the developed sensor exhibited outstanding performance as analytical sensing tools, regarding environmental, pharmaceutical, and clinical applications. Particularly, the miniaturized devices demonstrated in this dissertation were broadened for several purposes, depending on the device functionality and capability. Individual conclusion for each detection platform was deduced as follows;

**CHAPTER III: Development of nanomaterials-based miniaturized platforms for optical sensing application.** The novel optical sensors including a paper-based colorimetric sensor and screen-printed electroluminescent sensor were demonstrated for environmental and clinical sensing application. The enhanced sensitivity for these miniaturized devices is strongly influenced by the use of nanomaterials; silver nanoprisms (colorimetric sensor), graphene oxide (electroluminescent sensor). To allow simplicity and portability for on-site processing, a smartphone was integrated into these platforms as a quantitative readout. Compared with the traditional systems, the miniaturized devices outlined here are superior in terms of simple operation and interpretation, fast response and its versatility for a broad application.

**CHAPTER IV: Development of nanomaterials-based miniaturized platforms for electrochemical sensing applications.** The new electrochemical sensors were developed for a sensitive detection of a potential pharmaceutical

substance and clinical indicator. The key development reported here is the use of nanomaterials such as carbon-based nanomaterials (graphene, graphene oxide, graphene nanocomposite) and gold nanoparticles. In the first section, an anti-fouling electrode for a strong adsorb compound (vitamin D) was developed for continuous usage. The capability to prevent adsorption and enhance the sensor performance is due to the functionality of the graphene/Nafion nanocomposite. In addition, a microfluidic paper-based sensor was also developed for a fluid delivery system which could be a benefit for multi-steps assay. Ascorbic acid, serotonin, and alpha-fetoprotein, for instance, were selected as model analytes and further tested with several electrochemical formats.

## 5.2 Future perspective

Currently, the analytical trend is moving toward a smartphone-based detection. In this regard, the compact miniaturized device coupled with a smartphone would create new opportunities for the resource-limited area. In this perspective, the developed platforms show a great promising to be extended for numerous analyte detection, especially for point-of-care (POC) testing which is of prime importance. In addition, with the wireless technology, NFC (near-field communication)-enabled electronic devices, for example, can be used to overcome the gap of traditional electrochemical measurement in which a potentiostat is still needed to control electroanalytical experiments.

# REFERENCES

[1]     Lopez-Ruiz, N., et al. Smartphone-Based Simultaneous pH and Nitrite Colorimetric Determination for Paper Microfluidic Devices. <u>Analytical Chemistry</u> 86(19) (2014): 9554-9562.

[2]     Gesellschaft, D.P., Poggendorff, J.C., Wiedemann, E., library, W.o., Wiedemann, G.H., and Berlin, P.G.z. <u>Annalen der Physik</u>. J. A. Barth, 1888.

[3]     Kitai, A. <u>Luminescent Materials and Applications</u>. Wiley, 2008.

[4]     Haranath, D., Shanker, V., and Vij, D.R. Electroluminescence. in <u>Handbook of Electroluminescent Materials</u>: Taylor & Francis, 2004.

[5]     Mahesh Kumar Jain. <u>Eternal War between Alternating and Direct Current continuing for Rail Transport</u> [Online]. 2014. Available from: <u>https://www.railelectrica.com/traction-distribution/war-between-alternating-and-direct-current/</u> [26 August]

[6]     Fischer, A.G. Electroluminescent Lines in ZnS Powder Particles II . Models and Comparison with Experience. <u>Journal of The Electrochemical Society</u> 110(7) (1963): 15.

[7]     Bard, A.J. and Faulkner, L.R. <u>Electrochemical Methods: Fundamentals and Applications, 2nd Edition</u>. John Wiley & Sons, 2000.

[8]     Shapley, P. <u>Galvanic and Electrolytic Cells</u> [Online]. 2012. Available from: <u>http://butane.chem.uiuc.edu/pshapley/genchem2/c6/1.html</u> [29 August]

[9]     Oberacher, H., Pitterl, F., Erb, R., and Plattner, S. Mass spectrometric methods for monitoring redox processes in electrochemical cells. <u>Mass Spectrometry Reviews</u> 34(1) (2015): 64-92.

[10]    Skoog, D.A., West, D.M., Crouch, S.R., and Holler, F.J. <u>Fundamentals of Analytical Chemistry</u>. Thomson-Brooks/Cole, 2004.

[11]    <u>Pulse Voltammetric Techniques</u> [Online]. Available from: <u>https://www.basinc.com/manuals/EC_epsilon/Techniques/Pulse/pulse</u> [28 August]

[12]    Zelić, M. Reverse Scan as a Source of Information in Square Wave Voltammetry.

Croatica Chemica Acta 79(1) (2006): 6.

[13]     Yogesh Singh, A.A. Electroanalytical techniques [Online]. Available from: https://www.serotonin.ucla.edu/pages/electroanalytical [29 August]

[14]     Randviir, E. and Banks, C. Electrochemical impedance spectroscopy: An overview of bioanalytical applications. Vol. 5, 2013.

[15]     Renault, C., Koehne, J., Ricco, A.J., and Crooks, R.M. Three-Dimensional Wax Patterning of Paper Fluidic Devices. Langmuir 30(23) (2014): 7030-7036.

[16]     Organization, W.H. Guidelines for Drinking-water Quality: Recommendations. World Health Organization, 2004.

[17]     Morales, J.A., de Graterol, L.S., and Mesa, J. Determination of chloride, sulfate and nitrate in groundwater samples by ion chromatography. Journal of Chromatography A 884(1) (2000): 185-190.

[18]     Edgell, K.W., Longbottom, J.E., and Pfaff, J.D. Determination of inorganic anions in water by ion chromatography: a collaborative study. Journal of AOAC International 77(5) (1994): 1253-1263.

[19]     Bujes-Garrido, J. and Arcos-Martínez, M.J. Disposable sensor for electrochemical determination of chloride ions. Talanta 155 (2016): 153-157.

[20]     Amra Bratovcic, A.S.O. Determination of Fluoride and Chloride Contents in Drinking Water by Ion Selective Electrode. in Environmental Monitoring, Ekundayo, E.O., Editor. 2011, IntechOpen.

[21]     Rocha, D.L. and Rocha, F.R.P. An environmentally friendly flow-based procedure with photo-induced oxidation for the spectrophotometric determination of chloride in urine and waters. Microchemical Journal 108 (2013): 193-197.

[22]     Silva, C.R., Vieira, H.J., Canaes, L.S., Nóbrega, J.A., and Fatibello-Filho, O. Flow injection spectrophotometric method for chloride determination in natural waters using Hg(SCN)2 immobilized in epoxy resin. Talanta 65(4) (2005): 965-970.

[23]     Maya, F., Estela, J.M., and Cerdà, V. Spectrophotometric determination of chloride in waters using a multisyringe flow injection system. Talanta 74(5) (2008): 1534-1538.

[24]     Bonifácio, V.G., Figueiredo-Filho, L.C., Marcolino, L.H., and Fatibello-Filho, O. An improved flow system for chloride determination in natural waters exploiting

solid-phase reactor and long pathlength spectrophotometry. <u>Talanta</u> 72(2) (2007): 663-667.

[25] Parvinen, P. and Lajunen, L.H.J. Determination of chloride in drinking and ground water by AlCl molecular absorption spectrometry using graphite furnace atomic absorption spectrometer. <u>Talanta</u> 50(1) (1999): 67-71.

[26] Cirello-Egamino, J. and Brindle, I.D. Determination of chloride ions by reaction with mercury thiocyanate in the absence of iron(III) using a UV-photometric, flow injection method. <u>Analyst</u> 120(1) (1995): 183-186.

[27] Clarke, F.E. Determination of Chloride in Water Improved Colorimetric and Titrimetric Methods. <u>Analytical Chemistry</u> 22(4) (1950): 553-555.

[28] Horwitz, W. and Latimer, G.W. <u>Official methods of analysis of AOAC International</u>. 18th ed. ed. Gaithersburg, Md.: AOAC International, 2005.

[29] Meredith, N.A., Quinn, C., Cate, D.M., Reilly, T.H., Volckens, J., and Henry, C.S. Paper-based analytical devices for environmental analysis. <u>Analyst</u> 141(6) (2016): 1874-1887.

[30] Cate, D.M., Adkins, J.A., Mettakoonpitak, J., and Henry, C.S. Recent Developments in Paper-Based Microfluidic Devices. <u>Analytical Chemistry</u> 87(1) (2015): 19-41.

[31] Liana, D.D., Raguse, B., Gooding, J.J., and Chow, E. Recent Advances in Paper-Based Sensors. <u>Sensors</u> 12(9) (2012): 11505.

[32] Apilux, A., Siangproh, W., Praphairaksit, N., and Chailapakul, O. Simple and rapid colorimetric detection of Hg(II) by a paper-based device using silver nanoplates. <u>Talanta</u> 97 (2012): 388-394.

[33] Wiley, B., Sun, Y., Mayers, B., and Xia, Y. Shape-Controlled Synthesis of Metal Nanostructures: The Case of Silver. <u>Chemistry – A European Journal</u> 11(2) (2005): 454-463.

[34] Gao , C., et al. Highly Stable Silver Nanoplates for Surface Plasmon Resonance Biosensing. <u>Angewandte Chemie International Edition</u> 51(23) (2012): 5629-5633.

[35] Chaiyo, S., Siangproh, W., Apilux, A., and Chailapakul, O. Highly selective and sensitive paper-based colorimetric sensor using thiosulfate catalytic etching of

silver nanoplates for trace determination of copper ions. Analytica Chimica Acta 866 (2015): 75-83.

[36]    Li, J., Li, W., Qiang, W., Wang, X., Li, H., and Xu, D. A non-aggregation colorimetric assay for thrombin based on catalytic properties of silver nanoparticles. Analytica Chimica Acta 807 (2014): 120-125.

[37]    Duan, J., Yin, H., Wei, R., and Wang, W. Facile colorimetric detection of Hg2+ based on anti-aggregation of silver nanoparticles. Biosensors and Bioelectronics 57 (2014): 139-142.

[38]    Li, H., Li, F., Han, C., Cui, Z., Xie, G., and Zhang, A. Highly sensitive and selective tryptophan colorimetric sensor based on 4,4-bipyridine-functionalized silver nanoparticles. Sensors and Actuators B: Chemical 145(1) (2010): 194-199.

[39]    Shanmugaraj, K. and Ilanchelian, M. Colorimetric determination of sulfide using chitosan-capped silver nanoparticles. Microchimica Acta 183(5) (2016): 1721-1728.

[40]    Zhang, L. and Li, L. Colorimetric detection of hydrogen peroxide using silver nanoparticles with three different morphologies. Analytical Methods 8(37) (2016): 6691-6695.

[41]    Zhao, L., et al. Colorimetric detection of catalase and catalase-positive bacteria (E. coli) using silver nanoprisms. Analytical Methods 8(36) (2016): 6625-6630.

[42]    Millstone, J.E., Hurst, S.J., Métraux, G.S., Cutler, J.I., and Mirkin, C.A. Colloidal Gold and Silver Triangular Nanoprisms. Small 5(6) (2009): 646-664.

[43]    Pastoriza-Santos, I. and Liz-Marzán, L.M. Colloidal silver nanoplates. State of the art and future challenges. Journal of Materials Chemistry 18(15) (2008): 1724-1737.

[44]    Parnklang, T., Lertvachirapaiboon, C., Pienpinijtham, P., Wongravee, K., Thammacharoen, C., and Ekgasit, S. H2O2-triggered shape transformation of silver nanospheres to nanoprisms with controllable longitudinal LSPR wavelengths. RSC Advances 3(31) (2013): 12886-12894.

[45]    Zhang, Q., Li, N., Goebl, J., Lu, Z., and Yin, Y. A Systematic Study of the Synthesis of Silver Nanoplates: Is Citrate a "Magic" Reagent? Journal of the American Chemical Society 133(46) (2011): 18931-18939.

[46]     Chen, A., Cheng, H., Qin, B., Xu, Y., Li, R., and Tai, Z. Rapid Determination of Chloride Using Silver Triangular Nanoplates. Analytical Letters 48(14) (2015): 2223-2233.

[47]     Yang, X.-H., Ling, J., Peng, J., Cao, Q.-E., Ding, Z.-T., and Bian, L.-C. A colorimetric method for highly sensitive and accurate detection of iodide by finding the critical color in a color change process using silver triangular nanoplates. Analytica Chimica Acta 798 (2013): 74-81.

[48]     Bromide in drinking-water : background document for development of WHO guidelines for drinking-water quality. 2009, World Health Organization: Geneva : World Health Organization.

[49]     Vos, W.D., Salminen, R., and Tarvainen, T. Geochemical atlas of Europe: interpretation of geochemical maps, additional tables, figures, maps, and related publications. Geol. Surv. Finl. (2006): 205-208.

[50]     Indermitte, E., Saava, A., and Karro, E. Exposure to High Fluoride Drinking Water and Risk of Dental Fluorosis in Estonia. International Journal of Environmental Research and Public Health 6(2) (2009): 710.

[51]     Liu, J., et al. Two-Dimensional CH3NH3PbI3 Perovskite: Synthesis and Optoelectronic Application. ACS Nano 10(3) (2016): 3536-3542.

[52]     Bao, Q. and Loh, K.P. Graphene Photonics, Plasmonics, and Broadband Optoelectronic Devices. ACS Nano 6(5) (2012): 3677-3694.

[53]     Oh, S.J., et al. Selective p- and n-Doping of Colloidal PbSe Nanowires To Construct Electronic and Optoelectronic Devices. ACS Nano 9(7) (2015): 7536-7544.

[54]     Qin, J., et al. Controlled Growth of a Large-Size 2D Selenium Nanosheet and Its Electronic and Optoelectronic Applications. ACS Nano (2017).

[55]     Kwon, K.C., et al. Synthesis of Atomically Thin Transition Metal Disulfides for Charge Transport Layers in Optoelectronic Devices. ACS Nano 9(4) (2015): 4146-4155.

[56]     Park, Y., Ryu, B., Oh, B.-R., Song, Y., Liang, X., and Kurabayashi, K. Biotunable Nanoplasmonic Filter on Few-Layer MoS2 for Rapid and Highly Sensitive Cytokine Optoelectronic Immunosensing. ACS Nano 11(6) (2017): 5697-5705.

[57]    Hu, G., et al. Black phosphorus ink formulation for inkjet printing of optoelectronics and photonics. <u>Nature Communications</u> 8(1) (2017): 278.

[58]    Dong, H., et al. A Flexible and Thin Graphene/Silver Nanowires/Polymer Hybrid Transparent Electrode for Optoelectronic Devices. <u>ACS Applied Materials & Interfaces</u> 8(45) (2016): 31212-31221.

[59]    Kim, T.-H., et al. Fully Stretchable Optoelectronic Sensors Based on Colloidal Quantum Dots for Sensing Photoplethysmographic Signals. <u>ACS Nano</u> 11(6) (2017): 5992-6003.

[60]    Jinno, H., et al. Stretchable and waterproof elastomer-coated organic photovoltaics for washable electronic textile applications. <u>Nature Energy</u> (2017).

[61]    Lee, H., Kim, M., Kim, I., and Lee, H. Flexible and Stretchable Optoelectronic Devices using Silver Nanowires and Graphene. <u>Advanced Materials</u> 28(22) (2016): 4541-4548.

[62]    Yi, F., et al. Stretchable and Waterproof Self-Charging Power System for Harvesting Energy from Diverse Deformation and Powering Wearable Electronics. <u>ACS Nano</u> 10(7) (2016): 6519-6525.

[63]    Cheng, Y., et al. Highly Stretchable and Conductive Copper Nanowire Based Fibers with Hierarchical Structure for Wearable Heaters. <u>ACS Applied Materials & Interfaces</u> 8(48) (2016): 32925-32933.

[64]    Koo, J.H., et al. Wearable Electrocardiogram Monitor Using Carbon Nanotube Electronics and Color-Tunable Organic Light-Emitting Diodes. <u>ACS Nano</u> (2017).

[65]    Choi, S., Lee, H., Ghaffari, R., Hyeon, T., and Kim, D.-H. Recent Advances in Flexible and Stretchable Bio-Electronic Devices Integrated with Nanomaterials. <u>Advanced Materials</u> 28(22) (2016): 4203-4218.

[66]    Cheng, Y., Wang, R., Sun, J., and Gao, L. A Stretchable and Highly Sensitive Graphene-Based Fiber for Sensing Tensile Strain, Bending, and Torsion. <u>Advanced Materials</u> 27(45) (2015): 7365-7371.

[67]    Kim, J., et al. Ultrathin Quantum Dot Display Integrated with Wearable Electronics. <u>Advanced Materials</u>: 1700217-n/a.

[68]    Park, J.H., Lee, S.H., Kim, J.S., Kwon, A.K., Park, H.L., and Han, S.D. White-electroluminescent device with ZnS:Mn, Cu, Cl phosphor. <u>Journal of</u>

Luminescence 126(2) (2007): 566-570.

[69]   Liang, G., Hu, H., Liao, L., He, Y., and Ye, C. Highly Flexible and Bright Electroluminescent Devices Based on Ag Nanowire Electrodes and Top-Emission Structure. Advanced Electronic Materials 3(3) (2017): 1600535-n/a.

[70]   Schrage, C. and Kaskel, S. Flexible and Transparent SWCNT Electrodes for Alternating Current Electroluminescence Devices. ACS Applied Materials & Interfaces 1(8) (2009): 1640-1644.

[71]   Torres Alonso, E., Karkera, G., Jones, G.F., Craciun, M.F., and Russo, S. Homogeneously Bright, Flexible, and Foldable Lighting Devices with Functionalized Graphene Electrodes. ACS Applied Materials & Interfaces 8(26) (2016): 16541-16545.

[72]   Rack, P.D. and Holloway, P.H. The structure, device physics, and material properties of thin film electroluminescent displays. Materials Science and Engineering: R: Reports 21(4) (1998): 171-219.

[73]   Cho, S.H., et al. Extremely Bright Full Color Alternating Current Electroluminescence of Solution-Blended Fluorescent Polymers with Self-Assembled Block Copolymer Micelles. ACS Nano 7(12) (2013): 10809-10817.

[74]   Berndt, K.W. and Lakowicz, J.R. Electroluminescent lamp-based phase fluorometer and oxygen sensor. Analytical Biochemistry 201(2) (1992): 319-325.

[75]   En-on, J., Tuantranont, A., Kerdcharoen, T., and Wongchoosuk, C. Flexible alternating current electroluminescent ammonia gas sensor. RSC Advances 7(27) (2017): 16885-16889.

[76]   Wang, Z.-g., et al. Flexible Graphene-Based Electroluminescent Devices. ACS Nano 5(9) (2011): 7149-7154.

[77]   You, B., Kim, Y., Ju, B.-K., and Kim, J.-W. Highly Stretchable and Waterproof Electroluminescence Device Based on Superstable Stretchable Transparent Electrode. ACS Applied Materials & Interfaces 9(6) (2017): 5486-5494.

[78]   Wood, V., et al. Inkjet-Printed Quantum Dot–Polymer Composites for Full-Color AC-Driven Displays. Advanced Materials 21(21) (2009): 2151-2155.

[79]   Sloma, M., Janczak, D., Wroblewski, G., Mlozniak, A., and Jakubowska, M. Electroluminescent structures printed on paper and textile elastic substrates.

Circuit World 40(1) (2014): 13-16.

[80]    Withnall, R., Harris, P., Silver, J., and Jones, S. 28.1: Invited Paper: Novel, Bright, Inorganic Electroluminescent Flexible Displays Comprising Ink Jet Printed Silver Back Electrodes. SID Symposium Digest of Technical Papers 41(1) (2010): 397-400.

[81]    Kim, E.H., et al. Organic light emitting board for dynamic interactive display. Nature Communications 8 (2017): 14964.

[82]    Morales-Narváez, E. and Merkoçi, A. Graphene Oxide as an Optical Biosensing Platform. Advanced Materials 24(25) (2012): 3298-3308.

[83]    Morales-Narváez, E., Sgobbi, L.F., Machado, S.A.S., and Merkoçi, A. Graphene-encapsulated materials: Synthesis, applications and trends. Progress in Materials Science 86(Supplement C) (2017): 1-24.

[84]    Chałupniak, A. and Merkoçi, A. Toward integrated detection and graphene-based removal of contaminants in a lab-on-a-chip platform. Nano Research 10(7) (2017): 2296-2310.

[85]    Li, N., Chen, X., Chen, X., Ding, X., and Zhao, X. Ultrahigh humidity sensitivity of graphene oxide combined with Ag nanoparticles. RSC Advances 7(73) (2017): 45988-45996.

[86]    Miyoshi, Y., et al. Flexible humidity sensor in a sandwich configuration with a hydrophilic porous membrane. Sensors and Actuators B: Chemical 142(1) (2009): 28-32.

[87]    Zampetti, E., et al. Design and optimization of an ultra thin flexible capacitive humidity sensor. Sensors and Actuators B: Chemical 143(1) (2009): 302-307.

[88]    Zhang, D., Tong, J., Xia, B., and Xue, Q. Ultrahigh performance humidity sensor based on layer-by-layer self-assembly of graphene oxide/polyelectrolyte nanocomposite film. Sensors and Actuators B: Chemical 203(Supplement C) (2014): 263-270.

[89]    Han, J.-W., Kim, B., Li, J., and Meyyappan, M. Carbon Nanotube Based Humidity Sensor on Cellulose Paper. The Journal of Physical Chemistry C 116(41) (2012): 22094-22097.

[90]    Kuang, Q., Lao, C., Wang, Z.L., Xie, Z., and Zheng, L. High-Sensitivity Humidity

Sensor Based on a Single SnO2 Nanowire. <u>Journal of the American Chemical Society</u> 129(19) (2007): 6070-6071.

[91]   Yu, H.-W., et al. Self-Powered Humidity Sensor Based on Graphene Oxide Composite Film Intercalated by Poly(Sodium 4-Styrenesulfonate). <u>ACS Applied Materials & Interfaces</u> 6(11) (2014): 8320-8326.

[92]   Zhou, G., et al. Highly Sensitive Wearable Textile-Based Humidity Sensor Made of High-Strength, Single-Walled Carbon Nanotube/Poly(vinyl alcohol) Filaments. <u>ACS Applied Materials & Interfaces</u> 9(5) (2017): 4788-4797.

[93]   Nair, R.R., Wu, H.A., Jayaram, P.N., Grigorieva, I.V., and Geim, A.K. Unimpeded Permeation of Water Through Helium-Leak–Tight Graphene-Based Membranes. <u>Science</u> 335(6067) (2012): 442-444.

[94]   Bi, H., et al. Ultrahigh humidity sensitivity of graphene oxide. <u>Scientific Reports</u> 3 (2013): 2714.

[95]   Karim, M.R., et al. Graphene Oxide Nanosheet with High Proton Conductivity. <u>Journal of the American Chemical Society</u> 135(22) (2013): 8097-8100.

[96]   O'Dea, J.R., Economou, N.J., and Buratto, S.K. Surface Morphology of Nafion at Hydrated and Dehydrated Conditions. <u>Macromolecules</u> 46(6) (2013): 2267-2274.

[97]   Liu, L., Chen, W., and Li, Y. An overview of the proton conductivity of nafion membranes through a statistical analysis. <u>Journal of Membrane Science</u> 504(Supplement C) (2016): 1-9.

[98]   Kreuer, K.-D., Dippel, T., Meyer, W., and Maier, J. Nafion® Membranes: Molecular Diffusion, Proton Conductivity and Proton Conduction Mechanism. <u>MRS Proceedings</u> 293 (2011).

[99]   Sumner, J.J., Creager, S.E., Ma, J.J., and DesMarteau, D.D. Proton Conductivity in Nafion® 117 and in a Novel Bis[(perfluoroalkyl)sulfonyl]imide Ionomer Membrane. <u>Journal of The Electrochemical Society</u> 145(1) (1998): 107-110.

[100]  Xuan, W., et al. Fast Response and High Sensitivity ZnO/glass Surface Acoustic Wave Humidity Sensors Using Graphene Oxide Sensing Layer. <u>Scientific Reports</u> 4 (2014): 7206.

[101]  Borini, S., et al. Ultrafast Graphene Oxide Humidity Sensors. <u>ACS Nano</u> 7(12) (2013): 11166-11173.

[102] Yasuma, F. and Hayano, J.-i. Respiratory Sinus Arrhythmia: Why Does the Heartbeat Synchronize With Respiratory Rhythm? Chest 125(2) (2004): 683-690.

[103] Bates, J., Schmalisch, G., Filbrun, D., and Stocks, J. Tidal breath analysis for infant pulmonary function testing. ERS/ATS Task Force on Standards for Infant Respiratory Function Testing. European Respiratory Society/American Thoracic Society. European Respiratory Journal 16(6) (2000): 1180-1192.

[104] Du, B., et al. MoS2-based all-fiber humidity sensor for monitoring human breath with fast response and recovery. Sensors and Actuators B: Chemical 251(Supplement C) (2017): 180-184.

[105] Ghosh, S., Ghosh, R., Kumar Guha, P., and Bhattacharyya, T.K. Enhanced Proton Conductivity of Graphene Oxide/Nafion Composite Material in Humidity Sensing Application. IEEE Transactions on Nanotechnology 15(5) (2016): 782-790.

[106] Lee, J.H., O'Keefe, J.H., Bell, D., Hensrud, D.D., and Holick, M.F. Vitamin D Deficiency. Journal of the American College of Cardiology 52(24) (2008): 1949-1956.

[107] National Institutes of Health. Vitamin D Fact Sheet for Consumers [Online]. 2016. Available from: https://ods.od.nih.gov/factsheets/VitaminD-Consumer/ [24 July, 2017]

[108] Lappe, J.M. The Role of Vitamin D in Human Health: A Paradigm Shift. Journal of Evidence-Based Complementary & Alternative Medicine 16(1) (2011): 58-72.

[109] Norman, A. Vitamin D. Elsevier Science, 2012.

[110] Holick , M.F. Vitamin D Deficiency. New England Journal of Medicine 357(3) (2007): 266-281.

[111] Perales, S., Alegría, A., Barberá, R., and Farré, R. Review: Determination of Vitamin D in Dairy Products by High Performance Liquid Chromatography. Revista de Agaroquimica y Tecnologia de Alimentos 11(6) (2005): 451-462.

[112] Blanco, D., Fernandez, M.P., and Gutierrez, M.D. Simultaneous determination of fat-soluble vitamins and provitamins in dairy products by liquid chromatography with a narrow-bore column. Analyst 125(3) (2000): 427-431.

[113] Gomis, D.B., Fernández, M.P., and Gutiérrez Alvarez, M.D. Simultaneous determination of fat-soluble vitamins and provitamins in milk by microcolumn

liquid chromatography. <u>Journal of Chromatography A</u> 891(1) (2000): 109-114.

[114] Heudi, O., Trisconi, M.-J., and Blake, C.-J. Simultaneous quantification of Vitamins A, D3 and E in fortified infant formulae by liquid chromatography–mass spectrometry. <u>Journal of Chromatography A</u> 1022(1) (2004): 115-123.

[115] Viñas, P., Bravo-Bravo, M., López-García, I., and Hernández-Córdoba, M. Dispersive liquid–liquid microextraction for the determination of vitamins D and K in foods by liquid chromatography with diode-array and atmospheric pressure chemical ionization-mass spectrometry detection. <u>Talanta</u> 115 (2013): 806-813.

[116] Strobel, N., Buddhadasa, S., Adorno, P., Stockham, K., and Greenfield, H. Vitamin D and 25-hydroxyvitamin D determination in meats by LC–IT-MS. <u>Food Chemistry</u> 138(2) (2013): 1042-1047.

[117] Bilodeau, L., et al. Determination of vitamin D3 and 25-hydroxyvitamin D3 in foodstuffs by HPLC UV-DAD and LC–MS/MS. <u>Journal of Food Composition and Analysis</u> 24(3) (2011): 441-448.

[118] Trenerry, V.C., Plozza, T., Caridi, D., and Murphy, S. The determination of vitamin D3 in bovine milk by liquid chromatography mass spectrometry. <u>Food Chemistry</u> 125(4) (2011): 1314-1319.

[119] Byrdwell, W.C., et al. Liquid chromatography with ultraviolet and dual parallel mass spectrometric detection for analysis of vitamin D in retail fortified orange juice. <u>Journal of Food Composition and Analysis</u> 24(3) (2011): 299-306.

[120] Mackay, C., Tillman, J., and Burns, D.T. Determination of vitamin D2 in multivitamin tablets by high-performance liquid chromatography. <u>Analyst</u> 104(1240) (1979): 626-636.

[121] Hart, J.P., Norman, M.D., and Lacey, C.J. Voltammetric behaviour of vitamins D2 and D3 at a glassy carbon electrode and their determination in pharmaceutical products by using liquid chromatography with amperometric detection. <u>Analyst</u> 117(9) (1992): 1441-1445.

[122] Méndez, J.H., Pérez, A.S., Zamarreño, M.D., and Garcia, M.L.H. Voltammetric determination of vitamin D3 with a rotating glassy carbon electrode. <u>Journal of Pharmaceutical and Biomedical Analysis</u> 6(6) (1988): 737-741.

[123] Chan, Y.Y., Yue, Y., and Webster, R.D. Voltammetric Studies on Vitamins D2 and

D3 in Organic Solvents. <u>Electrochimica Acta</u> 138 (2014): 400-409.

[124]   Webster, R.D. Voltammetry of the liposoluble vitamins (A, D, E and K) in organic solvents. <u>The Chemical Record</u> 12(1) (2012): 188-200.

[125]   Yang, X., Kirsch, J., Olsen, E.V., Fergus, J.W., and Simonian, A.L. Anti-fouling PEDOT:PSS modification on glassy carbon electrodes for continuous monitoring of tricresyl phosphate. <u>Sensors and Actuators B: Chemical</u> 177 (2013): 659-667.

[126]   Heras, M.A., et al. A poly(3,4-ethylenedioxythiophene)-poly(styrene sulphonate) composite electrode coating in the electrooxidation of phenol. <u>Electrochimica Acta</u> 50(7) (2005): 1685-1691.

[127]   Wang, W., Cui, M., Song, Z., and Luo, X. An antifouling electrochemical immunosensor for carcinoembryonic antigen based on hyaluronic acid doped conducting polymer PEDOT. <u>RSC Advances</u> 6(91) (2016): 88411-88416.

[128]   Lupu, S., Lete, C., Marin, M., Totir, N., and Balaure, P.C. Electrochemical sensors based on platinum electrodes modified with hybrid inorganic–organic coatings for determination of 4-nitrophenol and dopamine. <u>Electrochimica Acta</u> 54(7) (2009): 1932-1938.

[129]   Friedel, B., et al. Effects of Layer Thickness and Annealing of PEDOT:PSS Layers in Organic Photodetectors. <u>Macromolecules</u> 42(17) (2009): 6741-6747.

[130]   Wang, X. and Wang, Z.M. <u>High-Efficiency Solar Cells: Physics, Materials, and Devices</u>. Springer International Publishing, 2013.

[131]   Lai, T.-H., Tsang, S.-W., Manders, J.R., Chen, S., and So, F. Properties of interlayer for organic photovoltaics. <u>Materials Today</u> 16(11) (2013): 424-432.

[132]   Vreeland, R.F., et al. Biocompatible PEDOT:Nafion Composite Electrode Coatings for Selective Detection of Neurotransmitters in Vivo. <u>Analytical Chemistry</u> 87(5) (2015): 2600-2607.

[133]   Lee, Y.J., Kim, J.D., and Park, J.Y. Nafion coated enzyme free glucose micro-biosensors for anti-fouling of protein. in <u>2009 4th IEEE International Conference on Nano/Micro Engineered and Molecular Systems</u>, pp. 335-338, 2009.

[134]   Zhang, Z., et al. Anti-fouling in situ deposited antimony/nafion film electrode for electrochemical stripping analysis. <u>Int. J. Electrochem. Sci</u> 8 (2013): 4183-4193.

[135]   Xie, L.-Q., et al. A highly sensitive dopamine sensor based on a
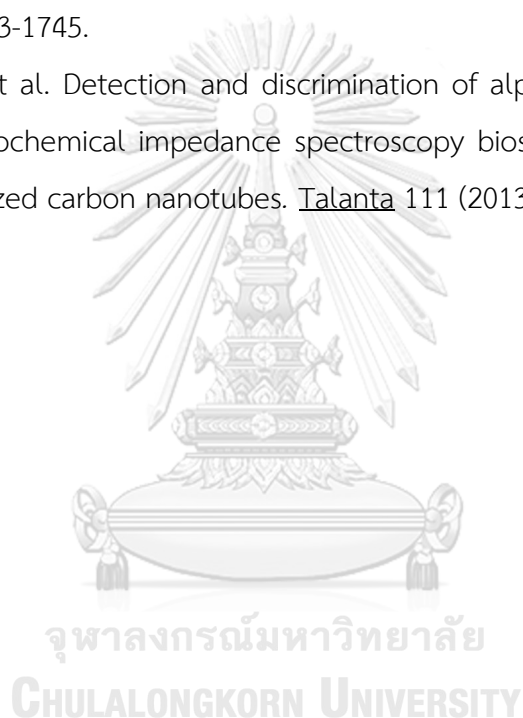
polyaniline/reduced graphene oxide/Nafion nanocomposite. <u>Chinese Chemical Letters</u> 28(1) (2017): 41-48.

[136] Wu, S., Huang, F., Lan, X., Wang, X., Wang, J., and Meng, C. Electrochemically reduced graphene oxide and Nafion nanocomposite for ultralow potential detection of organophosphate pesticide. <u>Sensors and Actuators B: Chemical</u> 177 (2013): 724-729.

[137] Er, E., Çelikkan, H., and Erk, N. Highly sensitive and selective electrochemical sensor based on high-quality graphene/nafion nanocomposite for voltammetric determination of nebivolol. <u>Sensors and Actuators B: Chemical</u> 224 (2016): 170-177.

[138] Wisniewski, N. and Reichert, M. Methods for reducing biosensor membrane biofouling. <u>Colloids and Surfaces B: Biointerfaces</u> 18(3) (2000): 197-219.

[139] Kondo, T., et al. Enhanced Sensitivity for Electrochemical Detection Using Screen-Printed Diamond Electrodes via the Random Microelectrode Array Effect. <u>Analytical Chemistry</u> 88(3) (2016): 1753-1759.

[140] Gayen, P. and Chaplin, B.P. Selective Electrochemical Detection of Ciprofloxacin with a Porous Nafion/Multiwalled Carbon Nanotube Composite Film Electrode. <u>ACS Applied Materials & Interfaces</u> 8(3) (2016): 1615-1626.

[141] Wang, F., Yu, X., Li, H., Li, M., and Feng, Q. Graphene-Nafion Composite Film Modified Electrode for Voltammetric Sensor for Determination of Dihydromyricetin. <u>Journal of the Chinese Chemical Society</u> 60(8) (2013): 1019-1026.

[142] Cincotto, F.H., Canevari, T.C., and Machado, S.A.S. Highly Sensitive Electrochemical Sensor for Determination of Vitamin D in Mixtures of Water-Ethanol. <u>Electroanalysis</u> 26(12) (2014): 2783-2788.

[143] Wu, M., Zhang, H., Zeng, B., and Zhao, F. A strategy to enhance the antifouling property of coating for direct immersion solid phase microextraction. <u>Journal of Chromatography A</u> 1384 (2015): 22-27.

[144] Arlinda Nallbani, J.H., Milan Sýs, Tahir Arbneshi, Karel Vytřas. Voltammetric determination of cholecalciferol at glassy carbon electrode performed in water

ethanol mixture. <u>Potravinarstvo Slovak Journal of Food Sciences</u> 12 (2018): 6.

[145]   Canevari, T.C., Cincotto, F.H., Landers, R., and Machado, S.A.S. Synthesis and characterization of α-nickel (II) hydroxide particles on organic-inorganic matrix and its application in a sensitive electrochemical sensor for vitamin D determination. <u>Electrochimica Acta</u> 147 (2014): 688-695.

[146]   Kun Men, Y.C., Jinbiao Liu, Dianjun Wei. Electrochemical Detection of Vitamin D2 and D3 Based on a AuPd Modified Glassy Carbon Electrode. <u>International Journal of Electrochemical Science</u> 12 (2017): 9.

[147]   Martinez, A.W., Phillips, S.T., Butte, M.J., and Whitesides, G.M. Patterned Paper as a Platform for Inexpensive, Low-Volume, Portable Bioassays. <u>Angewandte Chemie International Edition</u> 46(8) (2007): 1318-1320.

[148]   Preechakasedkit, P., Siangproh, W., Khongchareonporn, N., Ngamrojanavanich, N., and Chailapakul, O. Development of an automated wax-printed paper-based lateral flow device for alpha-fetoprotein enzyme-linked immunosorbent assay. <u>Biosensors and Bioelectronics</u> 102 (2018): 27-32.

[149]   Verma, M.S., et al. Sliding-strip microfluidic device enables ELISA on paper. <u>Biosensors and Bioelectronics</u> 99 (2018): 77-84.

[150]   Pungjunun, K., Chaiyo, S., Jantrahong, I., Nantaphol, S., Siangproh, W., and Chailapakul, O. Anodic stripping voltammetric determination of total arsenic using a gold nanoparticle-modified boron-doped diamond electrode on a paper-based device. <u>Microchimica Acta</u> 185(7) (2018): 324.

[151]   Jung, J.H., Cheon, D.S., Liu, F., Lee, K.B., and Seo, T.S. A Graphene Oxide Based Immuno-biosensor for Pathogen Detection. <u>Angewandte Chemie International Edition</u> 49(33) (2010): 5708-5711.

[152]   Cate, D.M., Noblitt, S.D., Volckens, J., and Henry, C.S. Multiplexed Paper Analytical Device for Quantification of Metals using Distance-Based Detection. <u>Lab on a chip</u> 15(13) (2015): 2808-2818.

[153]   Holstein, C.A., et al. Immobilizing affinity proteins to nitrocellulose: a toolbox for paper-based assay developers. <u>Analytical and Bioanalytical Chemistry</u> 408(5) (2016): 1335-1346.

[154] Chiu, N.-F., Huang, T.-Y., Lai, H.-C., and Liu, K.-C. Graphene oxide-based SPR biosensor chip for immunoassay applications. <u>Nanoscale Research Letters</u> 9(1) (2014): 445.

[155] Xie, K.-X., et al. Graphene oxide-assisted surface plasmon coupled emission for amplified fluorescence immunoassay. <u>Sensors and Actuators B: Chemical</u> 253 (2017): 804-808.

[156] Deng, X., et al. A Highly Sensitive Immunosorbent Assay Based on Biotinylated Graphene Oxide and the Quartz Crystal Microbalance. <u>ACS Applied Materials & Interfaces</u> 8(3) (2016): 1893-1902.

[157] Zhang, H., Sun, Y., Gao, S., Zhang, J., Zhang, H., and Song, D. A Novel Graphene Oxide-Based Surface Plasmon Resonance Biosensor for Immunoassay. <u>Small</u> 9(15) (2013): 2537-2540.

[158] Zhang, J. <u>PEM Fuel Cell Electrocatalysts and Catalyst Layers: Fundamentals and Applications</u>. Springer London, 2008.

[159] Bard, A.J. and Faulkner, L.R. <u>Electrochemical Methods: Fundamentals and Applications</u>. Wiley, 2000.

[160] Washburn, E.W. The Dynamics of Capillary Flow. <u>Physical Review</u> 17(3) (1921): 273-283.

[161] Ressler, K.J. and Nemeroff, C.B. Role of serotonergic and noradrenergic systems in the pathophysiology of depression and anxiety disorders. <u>Depress Anxiety</u> 12 Suppl 1 (2000): 2-19.

[162] Cowen, P.J. and Browning, M. What has serotonin to do with depression? <u>World Psychiatry</u> 14(2) (2015): 158-160.

[163] Wei, X., Wang, F., Yin, Y., Liu, Q., Zou, L., and Ye, B. Selective detection of neurotransmitter serotonin by a gold nanoparticle-modified glassy carbon electrode. <u>Analyst</u> 135(9) (2010): 2286-2290.

[164] Wang, H., et al. Label-free immunosensor based on Pd nanoplates for amperometric immunoassay of alpha-fetoprotein. <u>Biosensors and Bioelectronics</u> 53 (2014): 305-309.

[165] Wang, T., Yang, Z., Lei, C., Lei, J., and Zhou, Y. An integrated giant magnetoimpedance biosensor for detection of biomarker. <u>Biosensors and</u>

Bioelectronics 58 (2014): 338-344.

[166] Mayorga-Martinez, C.C., et al. An iridium oxide nanoparticle and polythionine thin film based platform for sensitive Leishmania DNA detection. Journal of Materials Chemistry B 3(26) (2015): 5166-5171.

[167] Lisdat, F. and Schäfer, D. The use of electrochemical impedance spectroscopy for biosensing. Analytical and Bioanalytical Chemistry 391(5) (2008): 1555.

[168] Hu, Y., et al. Label-free electrochemical impedance sensing of DNA hybridization based on functionalized graphene sheets. Chemical Communications 47(6) (2011): 1743-1745.

[169] Yang, H., et al. Detection and discrimination of alpha-fetoprotein with a label-free electrochemical impedance spectroscopy biosensor array based on lectin functionalized carbon nanotubes. Talanta 111 (2013): 62-68.

จุฬาลงกรณ์มหาวิทยาลัย

CHULALONGKORN UNIVERSITY

# VITA

| | |
|---|---|
| NAME | Abdulhadee Yakoh |
| DATE OF BIRTH | 29 January 1991 |
| PLACE OF BIRTH | Narathiwat |
| INSTITUTIONS ATTENDED | Doctor of Philosophy |
| HOME ADDRESS | 12 Soi2, Yakang1 Road, Bangnak, Muang, Narathiwat, Thailand |
| PUBLICATION | 1. A. Yakoh, C. Pinyorospathum, W. Siangproh, O. Chailapakul, Review: Biomedical Probes Based on Inorganic Nanoparticles for Electrochemical and Optical Spectroscopy Applications, Sensors, 2015, 15, 21427-21477. |

PUBLICATION (continued):

2. A. Yakoh, W. Siangproh, Colorimetric detection of ethanolamine using silver nanoparticles as colorimetric agent, Srinakharinwirot Science Journal, 2015, 31, 26-15.

3. A. Yakoh, P. Rattanarat, W. Siangproh, O. Chailapakul, Simple and selective paper-based colorimetric sensor for determination of chloride ion in environmental samples using label-free silver nanoprisms, Talanta, 2018, 178, 134-140.

4. A. Yakoh, R. A. Diduk, O. Chailapakul, A. Merkoçi, Screen-printed electroluminescent lamp modified with graphene oxide as a sensing device, ACS Applied Materials & Interfaces, 2018, 10, 20775-20782.

5. A. Yakoh, O. Chailapakul, W. Siangproh, Fabrication and characterization of graphene-Nafion nanocomposite and its application in highly sensitive electrochemical sensor for vitamin D determination, Sensors and Actuators B

(Submitted), 2018.

6. A. Yakoh, S. Chaiyo, W. Siangproh, O. Chailapakul, A 3D capillary-driven paper-based sequential microfluidic device for sensing applications, Lab on a Chip (Submitted), 2018.

**AWARD RECEIVED**   The best poster presentation, the 41st congress on science and technology of Thailand (STT41), 2015